

**Surface modification and mechanical reliability enhancement of
free-standing single crystal silicon microstructures using
localized KrF excimer laser annealing**

2015

Mohamed Elwi Mitwally

**Surface modification and mechanical reliability enhancement of
free-standing single crystal silicon microstructures using localized
KrF excimer laser annealing**

By

Mohamed Elwi Mitwally

A dissertation submitted in partial fulfillment
of the requirements for the degree of
Doctor of Engineering (Micro Engineering)

Kyoto University

2015

Dedication

**This thesis is dedicated to my parents
whom I wished to be there on my graduation day.
May they rest in peace.**

Acknowledgements

I thank Allah for his support and generosity without which I would not have been able to accomplish my work. I also need to remember my parent's support and help on different levels. I just wished they would have been with me to see the fruit of their investment. I am deeply indebted to my advisors; Professor Osamu Tabata and Professor Toshiyuki Tsuchiya for their guidance, their patience and their help during difficult periods of my life. I would like to thank Professor Sherif Sedky for his valuable discussions and inputs throughout the course of my research. I also am grateful to Dr. Sakakura for all his help with the laser annealing machine as well as the discussions we had. I would also like to thank my dissertation defense committee members; Professor Shiro Biwa and Professor Atsushi Matsubara for their advice and input in constructing my thesis.

I also need to recognize the help I got from other professors in my laboratory, Nano Micro systems Laboratory, Professor Koji Sugano and Professor Yoshikazu Hirai whose comments and questions during the lab seminars provided valuable insights into my work. I would also like to thank my colleagues in the laboratory; Tsujimoto, Singh, Uesugi, Zhipeng, Taniyama, Kogita, Katayama, Hokazono, Makino and Nakano for the fruitful discussions we had as well as their help with some of the laboratory equipment. I need to thank the laboratory staff for the help throughout my stay in Japan; Okino, Kawano, Fuji, Honda, Watanabe and Matoba. I also need to recognize the effort by microscopy room staff; Ishikawa and Kinoshita san for their help with using the FESEM as well as nano hub staff for helping me with using the equipment especially Inoue, Sato, Seto and Takahashi.

Finally I would like to thank my friends who made my stay pleasant in Japan; Yuko, Hisham, Gamil, Sherif, Sayed, Ahmed, Yasser and Abdallah.

Abstract

Microelectromechanical systems (MEMS) are used in many applications where many elements of MEMS devices are subjected to mechanical loads. These elements include beams and diaphragms that can be found in accelerometers, gyroscopes, micropumps and microvalves among other applications. Such elements are mainly subjected to tensile and fatigue loading. These elements operate in free-standing state and are basically made of single crystal silicon (SCS). In order to improve the mechanical performance of MEMS devices, it is necessary to choose a treatment technique that would be suitable for free-standing SCS microstructures. It is also important to study the factors that affect their behavior under tension or fatigue loading conditions. Two main factors that affect mechanical behavior of SCS microstructures are sidewall roughness resulting from fabrication and crystal orientation. Scallop on sidewalls act as stress concentration locations that can cause failure. It is also observed that SCS microstructures exhibit different mechanical properties and fracture behavior depending on crystal orientation. It the purpose of the current study to improve mechanical performance of free-standing SCS microstructures by improving sidewall roughness of samples oriented along different crystal orientations.

Laser treatment was chosen as the method of improving sidewall roughness. Laser treatment has an advantage over other roughness improvement techniques which is localized treatment. It was possible to focus the laser spot only to the sidewalls of the samples which allowed laser treatment at high energies up to 4 J/cm^2 without fracture. High energies are needed in order to melt scallops on the sidewalls. For efficient exposure of the sidewall to the laser beam, samples were tilted during irradiation. The effect of laser energy and number of pulses on sample morphology, topology and crystallinity was studied to find an optimum condition for laser treatment of mechanical test samples (conditioning stage).

It was found that laser energy was the major parameter affecting sample morphology and roughness. Samples irradiated at laser energies below 1.6 J/cm^2 showed an improvement in sidewall roughness and did not show a significant change in morphology. All irradiated samples also showed a crystalline nature after laser treatment.

From the knowledge gained during the conditioning stage, tension test samples were irradiated using two different laser treatment conditions. Sample oriented along $\langle 100 \rangle$ and $\langle 110 \rangle$ orientations were laser treated with the cross section shape, fracture behaviour and tensile strength investigated after the treatment. Using a low energy (1.2 J/cm^2) and high tilt angle (65°) led to a more preserved cross section with a slight strength improvement. The strength improvement was limited due to other surfaces that were not affected by laser treatment. An improvement of 30% in tensile strength was achieved compared to as-fabricated samples with a higher energy (4 J/cm^2) lower tilt angle (45°) treatment that was consistent for different sample orientations. The cross section of the samples treated at such condition was significantly changed however. The effect of sample orientation on fracture behaviour was studied and unstable crack propagation was observed for $\langle 100 \rangle$ oriented samples that was more significant after laser treatment.

Fatigue test samples were irradiated using 1 J/cm^2 at 45° . As-fabricated and laser treated samples were subjected to a constant deflection amplitude of 1.7° in a controlled environment. Fatigue life of laser treated samples showed a higher variation than as-fabricated samples that had an average life of 5.6×10^8 cycles. Two laser treated samples showed an improvement in fatigue life (1.8×10^9 cycles), one sample showed a comparable fatigue life to as-fabricated samples (1.1×10^7) and two samples fractured instantaneously. Poor performance of the two laser treated samples might be related to stress concentration features at the notch tip.

In conclusion, laser treatment was successful in improving mechanical performance of SCS microstructures under tensile or fatigue loading. This was reflected in a 30% improvement in fracture strength of tensile test samples as well as an improvement in fatigue life of two laser treated samples.

Table of contents

List of figures.....	vii
List of tables	xi
1. Introduction	1
1.1 Background and motivation.....	1
1.2 Research objectives.....	6
1.3 Thesis outline	7
2. Mechanical properties of silicon.....	9
2.1 Tensile strength of SCS	9
2.1.1 Effect of temperature.....	9
2.1.2 Size effect.....	11
2.1.3 Effect of crystal orientation:.....	12
2.1.4 Effect of surface roughness	13
2.2 Fatigue testing of SCS microstructures and factors affecting performance.	14
2.2.1 Environment effect.....	15
2.2.2 Effect of crystal orientation.....	16
2.2.3 Effect of surface roughness	16
2.3 Concluding remarks	17
3. Review on sidewall roughness reduction techniques	19
3.1 Wet etching	19
3.2 Thermal Oxidation	21
3.3 Hydrogen annealing.....	23
3.4 Laser annealing	26
4. Devices and experimental methods	31
4.1 Sample description and preparation.....	31
4.2 Experimental procedure	33
4.3 Evaluation of irradiated samples.....	34
4.4 Finite element analysis.....	35
4.5 Laser annealing	35
4.6 Tensile testing	38
4.7 Fatigue testing.....	39
5. Localized laser treatment on free-standing SCS structures	41
5.1 Laser irradiation at high laser energies without sample fracture	41
5.2 Temperature distribution.....	41

5.3 Effect of energy and number of pulses on sidewall morphology	43
5.4 Effect of energy and pulses on top surface morphology.....	45
5.5 Surface roughness of top surfaces.....	47
5.6 Crystallinity of top surfaces	49
5.7 Effect of laser energy, number of pulses on melt flow	50
5.8 Summary of laser treatment conditioning.....	51
6. Tensile strength and fracture behavior of laser treated SCS	53
6.1 Choice of laser treatment condition for tensile test samples.....	53
6.2: Temperature distribution analysis.....	53
6.3 Tensile strength of as-fabricated and laser treated samples.....	54
6.4 Effect of crystallographic orientation	60
6.5 Fracture behavior of as-fabricated and laser treated samples	63
6.6 Concluding remarks	64
7. Fatigue properties of laser treated SCS	65
7.1 Laser treatment of wide notch samples.....	65
7.2: Fatigue testing of wide notch samples.....	66
7.3 Fracture behavior of wide notch samples	68
7.4 Choice of laser treatment condition for narrow notch samples	69
7.5: Fatigue testing of narrow notch samples	71
7.6 Fracture behavior of narrow notch samples.....	73
7.7 Concluding remarks	76
8. Conclusions and future work.....	77
8.1 Thesis contributions	77
8.2 Future work.....	78
Bibliography	79
Appendix A.....	85
List of publications	91

List of figures

Fig 1.1: MEMS devices; a) Accelerometer [2], b) Gyroscope[3], c) Micropump[4] and d) Microvalve array[5].....	2
Fig 1.2: Various types of SCS samples subjected to fatigue testing in a) with corresponding S-N curve [8]	4
Fig 1.3: Reaction layer fatigue failure mechanism [9].....	5
Fig 1.4: Subcritical crack growth mechanism [9].....	5
Fig 2.1: Effect of temperature on a) Young's modulus [41], b) Fracture strength [41] and c) fracture toughness [40]	10
Fig 2.2: Young's modulus of various sizes of SCS structures in the a) nanometer scale, b) micrometer scale and c) millimeter scale [42]	11
Fig 2.3: Size effect on bending strength [42]	12
Fig 2.4: Typical fatigue test device using integrated sensing and actuation [16].....	14
Fig 2.5: Effect of environment on fatigue performance of SCS microstructures focusing mainly on a) humidity effect and b) temperature effect [8].....	15
Fig 2.6: Fatigue performance of a) different orientation of SCS microbeams shown in b) [12]	16
Fig 2.7: S-N for samples from different wafers. The solid line indicates the best fit based on samples from wafer 1 [50].....	17
Fig 3.1: Effect of KOH wet etching time on sidewall roughness for different orientations of SCS microbeams [24].....	20
Fig 3.2: Effect of KOH wet etching time on fracture strength for different orientations of SCS microbeams [24].....	21
Fig 3.3: Surface smoothing by wet oxidation [25]	22
Fig 3.4: Surface profile before and after wet oxidation [25]	22
Fig 3.5: Surface profile before and after dry oxidation [26]	23
Fig 3.6: Mechanism of surface smoothing due to hydrogen annealing [28]	24
Fig 3.7: Trench and cylindrical patterns subjected to hydrogen annealing [28]	24
Fig 3.8: AFM profile image of a 0.5 μm fabricated step after hydrogen annealing [28]	25
Fig 3.9: a) As-fabricated SCS sidewall surface, b) Hydrogen annealed surface for 30 minutes and c) Hydrogen annealed surface for 120 minutes [31].....	25
Fig 3.10: Fracture strength improvement due to hydrogen annealing at different hydrogen anneal times [31]	26

Fig 3.11: Cross sections of SCS waveguide. a) As-fabricated and laser treated at 1.4 J/cm ² , one shot at incident angles b) 45°, c) 60° d) 75° and 5 shots at the same energy at d) 45°, e) 60° and f) 75° [36]	27
Fig 3.12: Surface roughness of flat SCS surfaces a) As-fabricated and laser treated surfaces subjected to 1 shot of laser at 1.4 J/cm ² at the incident angles of b) 45°, c) 60°, d) 75°, e) 90° and 5 shots at the incident angle of f) 45° g) 60°, h) 75° and i) 90° [36]	28
Fig 3.13: Effect of number of pulses at different laser energies on RMS roughness [36]	28
Fig 4.1: Test samples; a) tensile test sample and b) fatigue test sample	31
Fig 4.2: Layout of the fatigue test chip	32
Fig 4.3: Sidewall view of the a) tensile and b) fatigue test samples	33
Fig 4.4: FESEM images of a) Top surfaces, b) bottom surfaces and c) Bottom surfaces with etch pits	33
Fig 4.5: Laser system layout	36
Fig 4.6: Sample holder	37
Fig 4.7: Schematic test setup for tilted irradiation of a) tensile and b) fatigue test samples	38
Fig 4.8: Schematic of tensile test setup (Not drawn to scale)	39
Fig 4.9: Layout of fatigue testing circuit	40
Fig 5.1: Temperature distribution due to a single laser pulse at 1.6 J/cm ² at 65°	42
Fig 5.2: FESEM image of a fatigue test sample subjected to a single pulse at 1.6 J/cm ² tilted at 65°	43
Fig 5.3: Sidewalls of fatigue test samples subjected to different laser treatment conditions	44
Fig 5.4: Top surface of tensile test sample subjected to 2 J/cm ² of laser energy for a) one pulse and b) ten pulses	46
Fig 5.5: Laser treated top surfaces of tensile samples for 10 pulses at a) 2.4 J/cm ² , b) 2.8 J/cm ² , c) 3.2 J/cm ² and d) 4 J/cm ²	47
Fig 5.6 Surface profiles for a) as-fabricated and laser annealed samples at b) 1.2 J/cm ² , c) 1.6 J/cm ² , d) 2.4 J/cm ² , and e) 2.8 J/cm ² and f) 3.2 J/cm ² with 10 pulses	48
Fig 5.7: Average roughness values for different laser energies with a 10 pulse treatment	48
Fig 5.8: Raman spectra for as-fabricated and laser irradiated tensile samples at different laser energies at 10 pulses	49
Fig 5.9: Change in normalized FWHM and Raman shift for different laser energies at 10 pulses	50

Fig 5.10: Summary of laser treatment results	52
Fig 6.1: Temperature distribution for laser treated samples at a) 4 J/cm ² tilted by 45° and b) 1.2 J/cm ² tilted by 65°	54
Fig 6.2: Fracture strength and location for as-fabricated and laser treated <110> samples	55
Fig 6.3: Fracture surfaces and sidewalls for as-fabricated and laser treated <110> samples. Fracture origin location is encircled	56
Fig 6.4: Bottom surfaces of laser treated <110> samples at 1.2 J/cm ² , 5 pulses tilted at 65° with several etch pits encircled	57
Fig. 6.5: Bottom surface of a laser treated samples at 4 J/cm ² that fractured at the bottom surface. A circle indicates the fracture origin and arrows indicate etch pits....	58
Fig. 6.6: Bottom view of a laser treated sample at 4 J/cm ² that fractured at sidewalls. A circle indicates the fracture origin.	59
Fig 6.7: Top surface view of a laser treated sample that fractured at top surface. A circle indicates the fracture origin.	59
Fig 6.8: Fracture strength and location for as-fabricated and laser treated <100> samples	61
Fig 6.9: Fracture surfaces and sidewalls for as-fabricated and laser treated <100> samples with fracture locations encircled.....	62
Fig 6.10: Top view of a laser treated <100> sample after fracture showing cleavage steps	63
Fig 6.11: 3D schematic of as-fabricated and laser treated <100> samples after fracture with fracture location encircled	64
Fig 7.1: Notch part of fatigue sample after laser treatment at 1.6 J/cm ² for 1 pulse at 65°, ridges are encircled	65
Fig 7.2: Fracture surfaces for selected fatigue samples.....	67
Fig 7.3: Sample in figure 7.1 after fracture at 1.6° a) Notch surface and b) fracture surface.....	68
Fig 7.4: Narrow notch test structure.	69
Fig 7.5: Top view at notch area of a sample irradiated at 1.4 J/cm ² , 2 pulses tilted at 65° with the protrusion encircled.....	70
Fig 7.6: Narrow notch top view of a) as-fabricated sample and b) laser treated samples	70
Fig 7.7: Notch area after laser treatment	70
Fig 7.8: Fracture surfaces for as-fabricated narrow notch <110> samples	72
Fig 7.9: Fracture surfaces for laser treated narrow notch <110> samples.....	74

Fig 7.10: Notch area of laser treated sample 3	75
Fig 7.11: Notch area of laser treated sample 5	75
Fig 7.12: Top view at notch area of laser treated sample 5	76

List of tables

Table 1.1: Young's modulus and fracture strength of SCS structures from literature [6]	3
Table 2.1: Fracture strengths of various orientations of SCS beams [43].....	13
Table 2.2: Fracture strengths of SCS subjected to different fabrication conditions (A, B and C) [49].....	13
Table 3.1: Comparison between different sidewall roughness improvement techniques	30
Table 4.1: Material properties for solid and liquid silicon	35
Table 7.1: Fatigue life of as-fabricated wide notch samples	66
Table 7.2: Fatigue life of as-fabricated narrow notch samples.....	71
Table 7.3: Fatigue life of laser treated samples with a narrow notch.....	72

1. Introduction

1.1 Background and motivation

Microelectromechanical systems (MEMS) are systems of miniaturized devices that perform electrical and mechanical functions to serve sensing and actuation applications. MEMS devices have characteristic lengths ranging from 1 μm to 1 mm. The miniaturization has allowed batch production of functional devices economically. Fabrication techniques of MEMS devices include surface micromachining, bulk micromachining, lithography and thin film deposition techniques. Basically these microfabrication techniques were based on those of the microelectronics technology. MEMS have complicated 3D structures as well as a variety of building materials. Sensing devices for MEMS include inertial sensors such as accelerometers and gyroscopes as well as pressure sensors. Inertial sensors as well as pressure sensors are used widely to serve many purposes. In the automotive field, accelerometers are used in automobile air bag systems while pressure sensors are used in tire pressure monitoring system. Aerospace applications include navigation control. Actuator applications include fluidic devices like micropumps and microvalves as well as optical devices like micromirrors. Microvalves and micropumps are widely used in biomedical and pharmaceutical fields as in drug delivery and chemical analysis applications. Figures of some of these devices are shown in figure 1.1.

The basic operation of the aforementioned devices is based on a moving proof mass as in the case of inertial sensors or a bending diaphragm as in the case of pressure sensors or microvalves and micropumps. Many elements in these devices are subjected to mechanical loads. Beams that support proof masses in accelerometers or gyroscopes deform as the mass moves in response to applied inertial force. Diaphragms of pressure sensors bend under applied pressure of the medium. Microvalves and micropumps depend also on diaphragm bending to control the cross sectional area of the flow channel in the case of microvalves or to apply enough pressure on the flowing fluid to be released as in the case of micropumps.

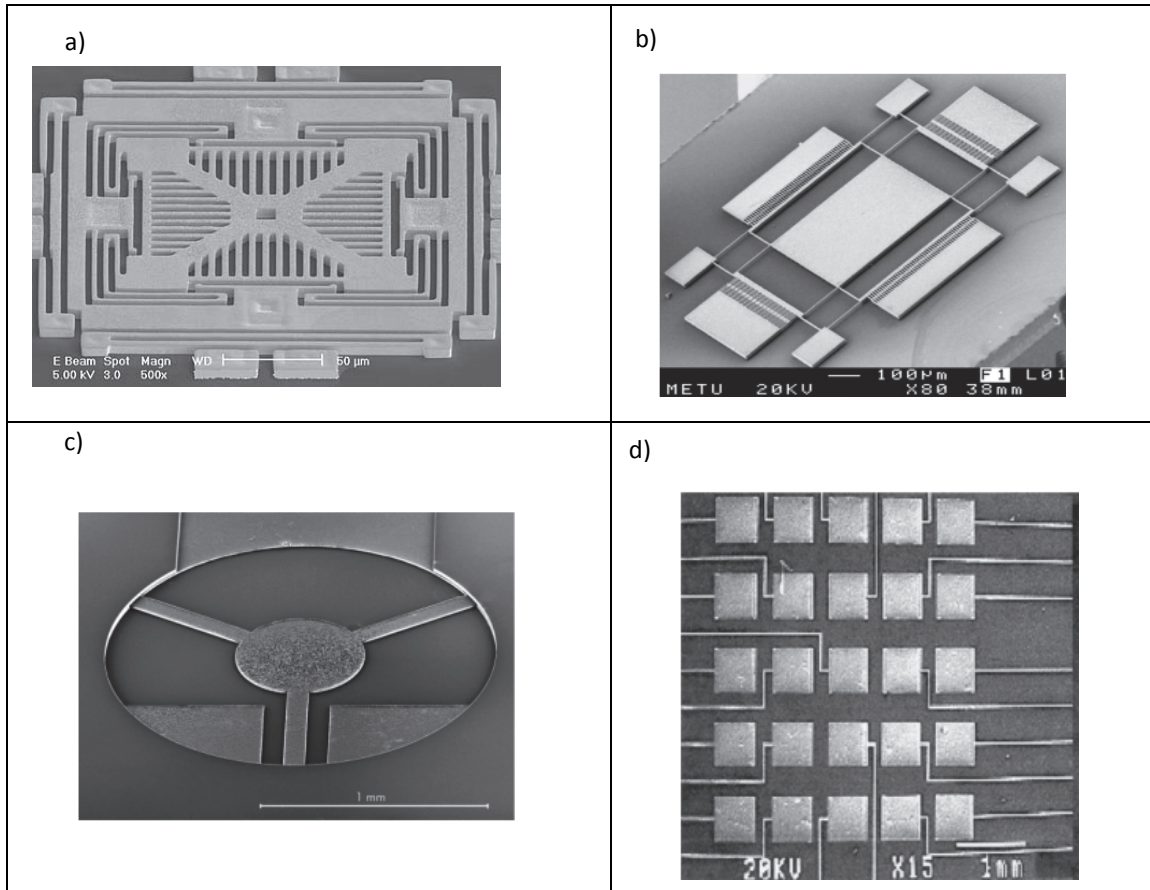


Fig 1.1: MEMS devices; a) Accelerometer [2], b) Gyroscope[3], c) Micropump[4] and d) Microvalve array[5]

These elements (beams, diaphragms) are in a free-standing state in order to perform the required functions. They are mainly fabricated from single crystal silicon (SCS) which is the main building material used in MEMS. Silicon can be easily processed into high purity electronic grade. It is also a semiconductor that can be doped to have regions of higher conductivity. From a mechanical application point of view, Silicon is a very attractive material since it has high tensile strength and Young's modulus [6].

In order to improve the performance of MEMS devices, it is crucial to improve the mechanical performance of the free-standing SCS elements that are involved in the sensing and actuation operation. MEMS elements are required to have high fracture strength (static loading) and fatigue life (dynamic loading). The mechanical performance of SCS structures under such loadings have been studied extensively.

Basic mechanical properties of silicon crystals like fracture strength and young's modulus has been summarized by Gad-el-Hak as shown in the table 1.1 [6]. Mechanical properties are much influenced by crystal orientation that determines

values of young's modulus as well as fracture strength. One other factor that was studied extensively and was found to affect fracture strength of SCS free-standing structures is surface roughness since it has been argued that miniaturized structures are more affected by surface defects rather than bulk defects because of their small volume [7].

Table 1.1: Young's modulus and fracture strength of SCS structures from literature [6]

Young's Modulus (GPa)	Fracture Strength (GPa)	Ref.	Method	Comments
177 ± 18	2.0–4.3	Johansson et al. (1988)	Bending	⟨110⟩
188	—	Weihs et al. (1989)	Indentation	
163	>3.4	Weihs et al. (1989)	Bending	⟨110⟩
122 ± 2	—	Ding et al. (1989)	Bending	⟨110⟩
125 ± 1	—	Ding et al. (1989)	Resonance	⟨110⟩
131	—	Zhang et al. (1991)	Resonance	
173 ± 13	—	Osterberg et al. (1994)	Bending	⟨110⟩
147	0.26–0.82	Cunningham et al. (1995)	Tension	⟨110⟩
—	8.5–20	Saif and MacDonald (1996)	Torsion	Shear and normal
60–200	—	Bhushan and Li (1997)	Indentation	Various doping
130	—	Dual et al. (1997)	Resonance	⟨100⟩
75	—	Dual et al. (1997)	Torsion	Shear modulus
125–180	1.3–2.1	Sato et al. (1997)	Tension	Three orientations
—	9.5–26.4	Chen et al. (1998)	Bending	Various etches
—	0.7–3.0	Chen et al. (1999)	Bending	Measured roughness
142 ± 9	1.73	Greek and Ericson (1998)	Tension	⟨100⟩
165 ± 20	2–8	Komai et al. (1998)	Bending	Fatigue tests also
168	—	Li and Bhushan (1999)	Indentation	⟨100⟩
—	0.59 ± 0.02	Mazza and Dual (1999)	Tension	⟨100⟩
—	2–6	Minoshima et al. (1999)	Bending	Fatigue also
169.2 ± 3.5	0.6–1.2	Yi and Kim (1999b)	Tension	Various etches
115–191	—	Yi and Kim (1999c)	Tension	Three orientations
164.9 ± 4	—	Anwander et al. (2000)	Tension	Laser speckle
169.9	0.5–17	Namazu et al. (2000)	Bending	Various sizes

SCS microstructures were observed to undergo fatigue failure under cyclic loading in various studies [8-22]. A review paper combining data from several fatigue tests done in Japanese institutes on different types of SCS and polysilicon microstructures presents a stress-number of cycles curve (S-N curve) as shown in figure 1.2b with the types of specimens used for testing shown in figure 1.2a[8].

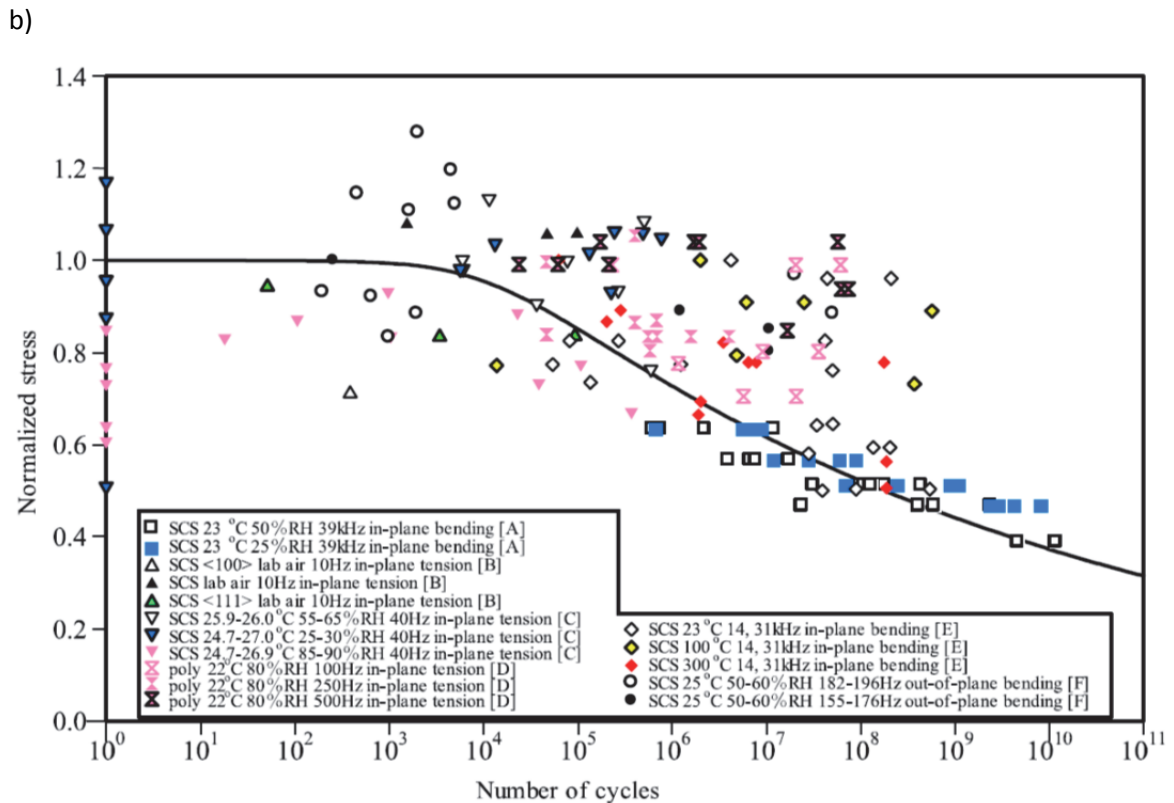
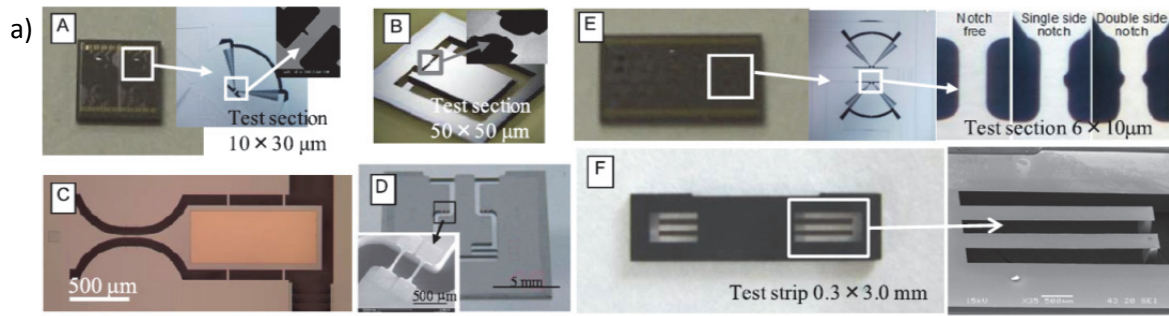


Fig 1.2: Various types of SCS samples subjected to fatigue testing in a) with corresponding S-N curve [8]

Figure 1.2b shows that SCS structures exhibit fatigue behavior. Although the applied cyclic stress still remains below the fracture strength of the material, the components fail by cyclic load. Two failure mechanisms have been suggested to explain this behavior. The first mechanism attributes failure to the growth of cracks in the native oxide layer of the SCS structure that gets thicker with loading cycles as the crack grows due to environmental moisture and/or oxygen as shown in figure 1.3[9]. The mechanism is called reaction layer fatigue. The second mechanism for failure is subcritical crack growth inside the SCS structure. Oxide debris or native oxide form on

crack surfaces during compression cycles causing a cantilever effect that leads to crack growth inside the silicon itself as shown in figure 1.4.[9]

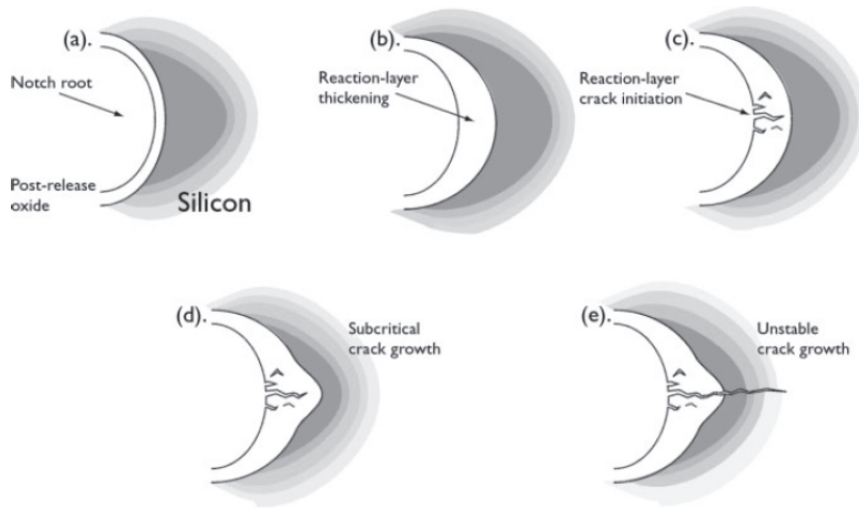


Fig 1.3: Reaction layer fatigue failure mechanism [9]

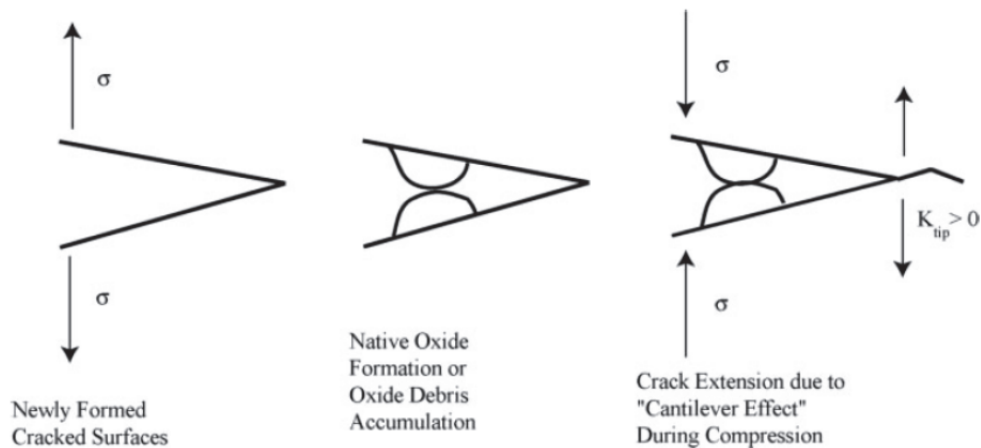


Fig 1.4: Subcritical crack growth mechanism [9]

Two main factors are thought to affect fatigue performance were surface roughness and crystal orientation. Ikehara et al found that samples having a rough surface at notch tip exhibited shorter life [10]. Pierron et al have suggested that cracks initiate at sidewalls where fabrication process leaves scallops that act as locations of stress concentration [11]. The significance of the fabrication history of the structures to be fatigue tested and how this can affect fatigue performance has been pointed out. Crystal orientation was also studied by Ikehara et al and it was found that samples oriented along the $\langle 100 \rangle$ direction exhibited a longer fatigue life compared to $\langle 110 \rangle$

samples for the same applied strain [10, 12]. Fracture behavior was also different for the two orientations.

So from previous studies about tensile or fatigue performance, it could be said that two common factors affecting the mechanical performance of SCS microstructures that were found to be crucial in determining both tensile or fatigue behavior are surface roughness and crystal orientation.

Surface roughness improvement of fabricated structures was performed using different techniques such as wet etching [23,24], thermal oxidation [25-27], hydrogen annealing [28-32] and laser annealing [33-36]. These techniques were successful in improving surface of planar surfaces as well as sidewalls having scallops resulting from fabrication and act as stress concentration locations. Improving sidewall roughness of MEMS components serves many purposes like decreasing scatter loss for waveguides as well as improving fracture strength. Most studies however dealt with supported structures rather than free-standing structures. MEMS components that are subjected to mechanical loading however involve mainly free-standing structures and accordingly any technique chosen to improve surface roughness for better mechanical performance should be suitable for such fragile structures. It is also beneficial to perform the treatment at the final stage of fabrication since this would mean that no further damage would be introduced due to fabrication after the treatment and would not affect the yield. Although most surface roughness improvement techniques are capable of handling free-standing structures, laser treatment has an advantage over other techniques which is localized treatment. Controlling the laser spot size allows only locations of interest to be treated rather than the whole device. This aspect is crucial in case polymeric or metallic components are present on the device that would be affected by high temperatures that are needed during thermal oxidation or hydrogen annealing.

1.2 Research objectives

It is the purpose of the research to improve surface roughness of free-standing microscale SCS structures as a means of improving mechanical performance and investigate the effect of such improvement on tensile and fatigue behavior of test structures oriented along different crystal orientations. Laser treatment is chosen as the technique for roughness improvement due to the ability of localized treatment. With

results from fatigue testing obtained together with tensile test results, more comprehensive conclusions can be made regarding the effectiveness of laser treatment as a technique for roughness improvement as well as the importance of sidewall roughness in determining mechanical performance of SCS microstructures.

- 1) Different techniques for improving sidewall roughness are reviewed and compared to choose the most suitable for the goal of our study and the SCS structures.
- 2) The chosen technique, excimer laser treatment, is evaluated and different parameters are tailored to achieve sidewall roughness improvement while not affecting other aspects like surface morphology.
- 3) Based on the parameter tailoring stage (conditioning stage), tensile testing on SCS structures is performed using the optimized laser treatment conditions. Different orientations of SCS structures are subjected to tensile testing to evaluate the effectiveness of the chosen technique in improving mechanical performance.
- 4) Finally fatigue testing is performed using optimized laser treatment conditions as well as insights from tensile testing. Fatigue life for as-fabricated and laser treated samples are compared to evaluate the effect of laser treatment on fatigue life.

1.3 Thesis outline

In chapter 2, a review on mechanical properties of silicon is provided. In chapter 3, a review on methods of improving sidewall roughness is provided as well as an evaluation for each technique and its applicability and appropriateness for improving sidewall roughness for free-standing SCS structures. Chapter 4 provides details on the test structures, experimental procedure and characterization techniques. Chapter 5 discusses parameter optimization and the effect of laser treatment on the test device surface morphology, roughness and crystallinity. Chapter 6 discusses the test results of tensile test for as-fabricated and laser treated samples while considering the effect of sample orientation. Chapter 7 deals with fatigue performance of as-fabricated and laser treated samples. Conclusions are presented in chapter 8 together with recommendations on future work.

2. Mechanical properties of silicon

Silicon is the second most abundant element after oxygen in earth's crust. It is a solid at room temperature with a melting point of 1414°C. Silicon has a diamond cubic crystal structure. It is considered a semiconductor. It has an electrical resistivity of 2300 $\Omega\cdot\text{m}$ at room temperature with a negative temperature coefficient of resistance. It has a Young's modulus of 130-188 GPa depending on crystal orientation as has been shown in table 1.1. Mechanical properties of SCS microstructures were investigated in various studies under tensile and fatigue loading conditions.

2.1 Tensile strength of SCS

Tensile tests were mainly performed using uniaxial loading or bending loading. Several factors were investigated that affect tensile strength of SCS microstructures. The factors discussed here are temperature, samples size, crystal orientation and surface roughness.

2.1.1 Effect of temperature

Bulk SCS is a brittle material at room temperature. The brittle to ductile transition temperature (BDTT) is from 550°C to 800°C [37-38]. In the case of micron sized MEMS components a number of studies have been conducted to study mechanical behavior of SCS structures at elevated temperatures. Nakao et al [40,41] conducted uniaxial tensile tests on SCS microstructures and measured mechanical properties change with temperatures ranging from room temperature to 500°C. The test structures were oriented on the (001) plane along the $\langle 110 \rangle$ direction. Notched samples were used for fracture toughness tests. Results for Young's modulus, fracture strength and fracture toughness against temperature are shown in figure 2.1. Young's modulus showed a maximum decrease of 5% at 500°C. Fracture strength decreased significantly with temperature to 32% at 500°C of the room temperature value. Stress strain curves corresponding to temperatures above 300°C deviated from linear plot indicating plastic deformation. This conclusion has also been supported by scanning electron microscopy (SEM) observations that showed clear slip planes.

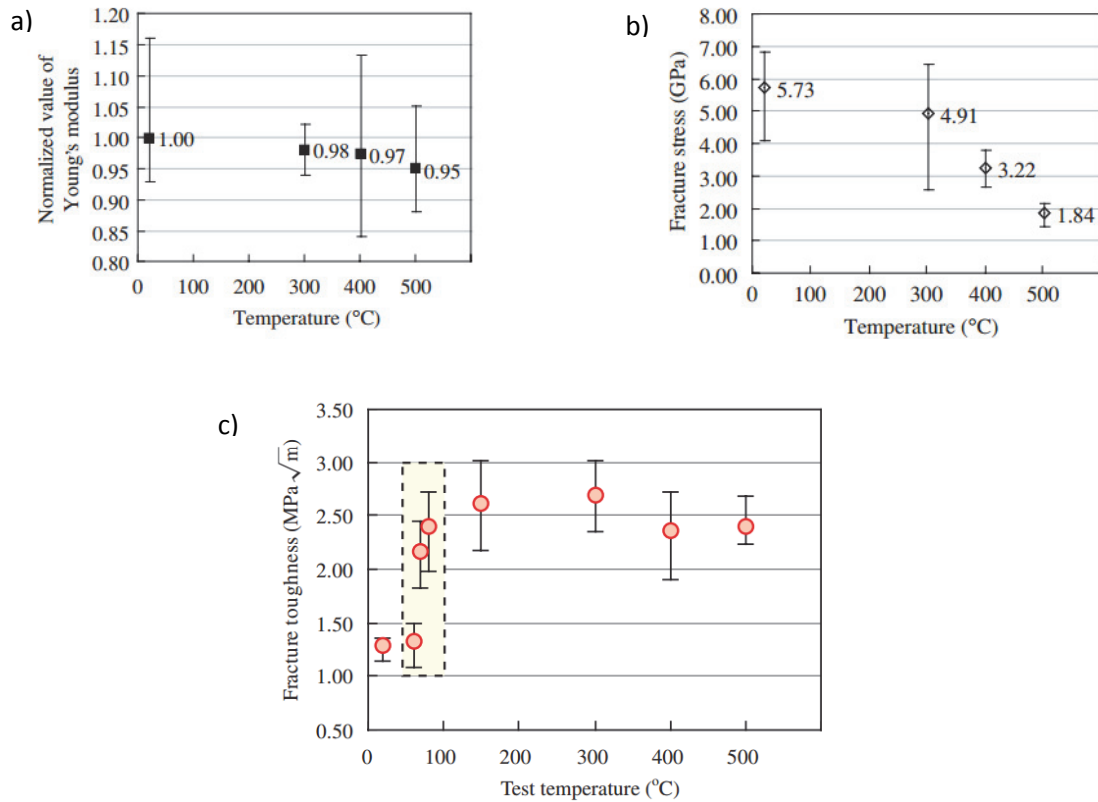


Fig 2.1: Effect of temperature on a) Young's modulus [41], b) Fracture strength [41] and c) fracture toughness [40]

Fracture toughness for microincreased with test temperature and the transition region was observed around 70°C although no nonlinear behavior was observed from stress strain curves. From SEM and transmission electron microscopy (TEM) observations, it was concluded that dislocations were generated at temperature as low as 80°C indicating a significant decrease in BDTT for SCS microstructures. This low BDTT was observed with samples having a thickness of 4 μm.

Another study on SCS microstructures and nanostructures being subjected to bending loads showed that BDTT decreased with samples size causing plasticity at lower temperatures characterized by lower fracture strength and higher fracture toughness than that for bulk SCS at same temperature[8]. Such behavior was attributed to the low bulk dislocation density of small size samples as well as their large surface area to volume ratio. Hence, plasticity is controlled by dislocation nucleation rather than multiplication of preexisting dislocation inside the crystals. Dislocation nucleation at the surface however requires less energy than that inside the bulk of the crystal and

accordingly lower BDTT is observed for small sized samples where nucleation of dislocation at the surface is less expensive [8].

2.1.2 Size effect

A study about the effect of size on bending strength was conducted by Namazu et al. [42]. Three point bending tests using an AFM tip on several SCS cantilevers having sizes ranging from the nanometer to the millimeter scale were performed at room temperature. Nanometer scale samples were 0.2-0.98 μm wide, 0.255 μm thick and 6 μm long. Micrometer scale samples were 4.75 to 74.5 μm wide, 1.91-19 μm thick and 35-360 μm long. Millimeter scale samples were 1045-1800 μm wide, 520 μm thick and 9850 μm long. Samples were oriented along the $\langle 110 \rangle$ direction on the (001) plane. Force displacement curves for different sample sizes from which Young's modulus is calculated are shown in figure 2.2 while figure 2.3 shows a cumulative probability plot of bending strength for different sizes.

The calculated value of Young's modulus doesn't show any change with sample size. For the $\langle 110 \rangle$ samples it showed an average value of 169 GPa regardless with size. Bending strength on the other hand showed a general decrease with samples size as can be seen in figure 2.3.

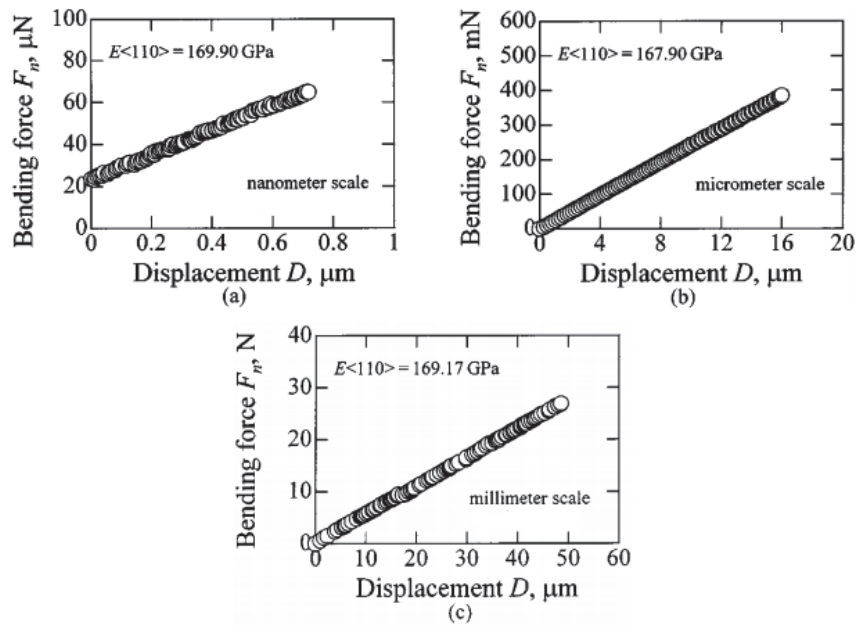


Fig 2.2: Young's modulus of various sizes of SCS structures in the a) nanometer scale, b) micrometer scale and c) millimeter scale [42]

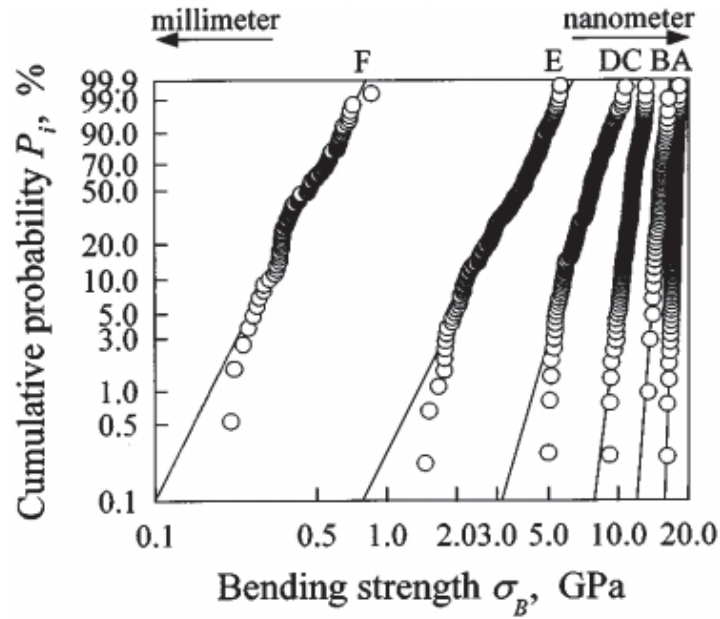


Fig 2.3: Size effect on bending strength [42]

The reason behind such variability in bending strength with sample size was attributed to surface roughness of the surfaces where the crack initiated. For the different sample sizes, roughness values showed a decrease as the sample size decreases.

2.1.3 Effect of crystal orientation:

The effect of crystal orientation on fracture strength, fracture toughness and Young's modulus of fabricated SCS structures was studied extensively [43-47]. Samples oriented along different directions and different planes were subjected to uniaxial tensile and bending tests with the aforementioned mechanical properties computed as well as the fracture behavior investigated. Focusing mainly on SCS microstructures without notches, Uesugi et al [43] investigated samples oriented along $\langle 110 \rangle$, $\langle 100 \rangle$ and $\langle 111 \rangle$ directions along the (110) plane together with samples oriented along the $\langle 110 \rangle$ and $\langle 100 \rangle$ directions along the (100) plane. All samples had a square cross section of $5 \times 5 \mu\text{m}$ and they were subjected to uniaxial tensile testing. All samples were subjected to the same fabrication conditions. Fracture strength results are shown in table 2.1 for samples oriented along different orientations

Table 2.1: Fracture strengths of various orientations of SCS beams [43]

Surface plane	(100)		(110)		
Tensile crystal orientation	<100>	<110>	<100>	<110>	<111>
Number of specimens	10	9	22	26	29
Average tensile strength (GPa)	2.7	3.14	3.69	3.62	3.62

All samples oriented along different directions on the (110) plane showed the same average tensile strength. Samples along the (100) plane on the other hand showed that <110> oriented samples had a higher strength than <100> samples with the difference still within 20%. The number of tested samples on the (100) plane was significantly less than that for the (110) plane as can be seen from table 2.2. All samples showed fracture surfaces along the (111) plane which is the expected cleavage plane having the lowest surface energy according to Griffith criterion [48].

2.1.4 Effect of surface roughness

As stated in section 2.1.2, Namazu et al [42] found that tested SCS samples with different sizes showed a change in strength with the smallest samples having the highest strength only because of sidewall morphology. A study by Uesugi et al [49] investigated the effect of fabrication condition on fracture strength of SCS microstructures. Samples were oriented along <110>, <100> and <111> directions on the (110). Results are shown in table 2.2 where A, B and C correspond to different fabrication conditions with the B condition having the best sidewall morphology followed by condition C and condition A.

Table 2.2: Fracture strengths of SCS subjected to different fabrication conditions (A, B and C) [49]

Conditions	A			B			C		
Tensile crystal orientations	<100>	<110>	<111>	<100>	<110>	<111>	<100>	<110>	<111>
Samples	30	29	30	22	26	29	25	22	28
Average strength [GPa]	1.61	1.89	1.86	3.69	3.62	3.62	2.59	2.69	3.01

Results show that for any crystal orientation, the average strength varies significantly according to sidewall morphology. Samples fabricated with condition B show the highest fracture strength followed by those fabricated using condition C and A. The improvement in strength was nearly doubled between condition A and B. This shows the importance sidewall roughness in determining tensile strength of fabricated SCS microstructures.

2.2 Fatigue testing of SCS microstructures and factors affecting performance.

Most studies dealing with fatigue testing on SCS microstructures tend to use devices with integrated actuation and sensing mechanisms. Electrostatic forces apply in-plane cyclic bending loads for the movement of the test structure. The test structure is usually a beam having a notch to have the crack initiate at the notch location to study the fracture behavior. A typical structure is shown in figure 2.4.

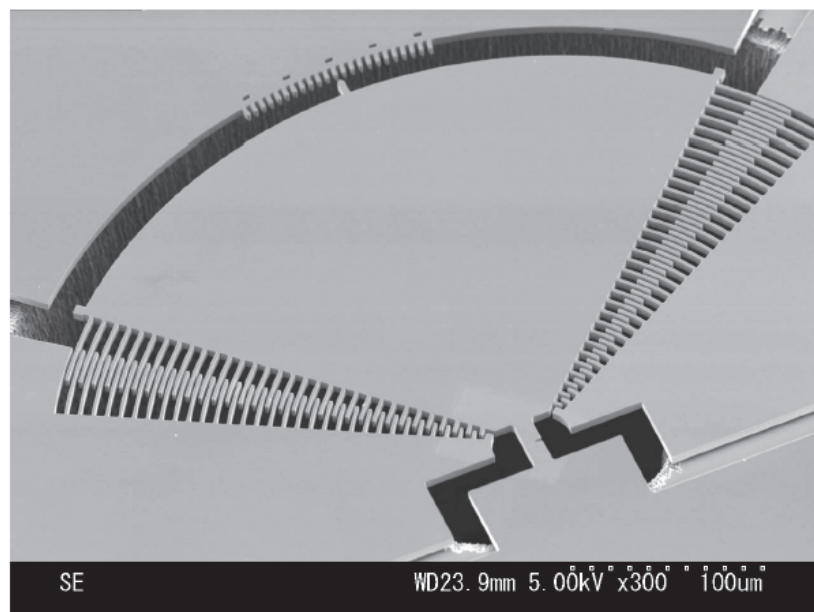


Fig 2.4: Typical fatigue test device using integrated sensing and actuation [16]

Several factors were investigated that affect fatigue performance of SCS microstructures. The factors discussed here are the environment effect, crystal orientation and surface roughness.

2.2.1 Environment effect

Both fatigue mechanisms of failure of SCS are concerned with surface or native oxide. Accordingly, the study of environmental factors affecting surface oxidation like temperature and humidity is important. The effect of temperature and humidity on SCS microstructures from research done by several Japanese institutes using the devices in figure 1.2b is shown in figure 2.5 [8]. An increase in temperature or humidity leads to a degradation in fatigue life as can be observed from figure 2.5. The effect of humidity on SCS and polysilicon microstructures is more significant than temperature.

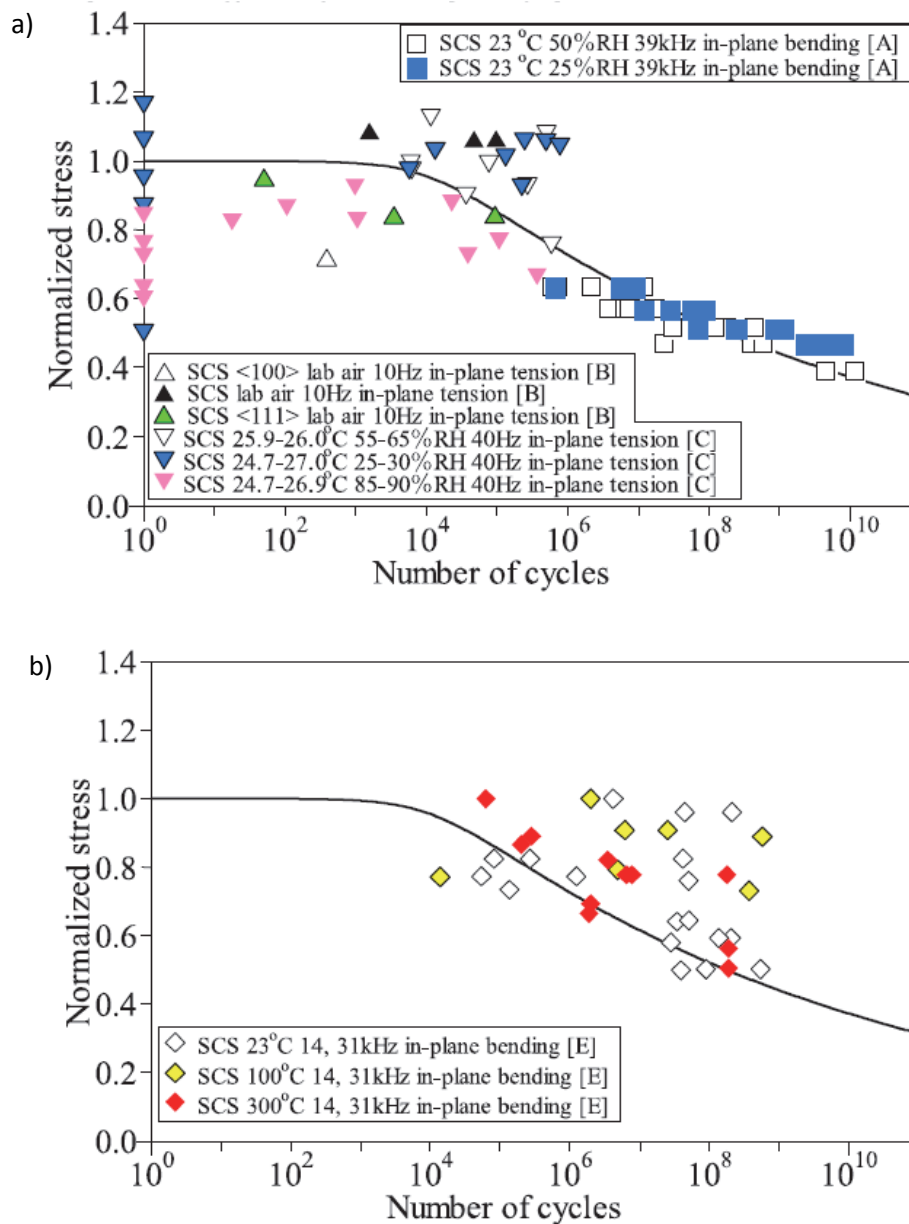


Fig 2.5: Effect of environment on fatigue performance of SCS microstructures focusing mainly on a) humidity effect and b) temperature effect [8]

2.2.2 Effect of crystal orientation

Ikehara et al [10,12] has studied the fatigue behavior of SCS microstructure oriented along $\langle 110 \rangle$ and $\langle 100 \rangle$ direction on a (001) wafer using the device shown in figure 2.4. Fatigue testing was performed at 23°C and 50% relative humidity. Results are shown in figure 2.6.

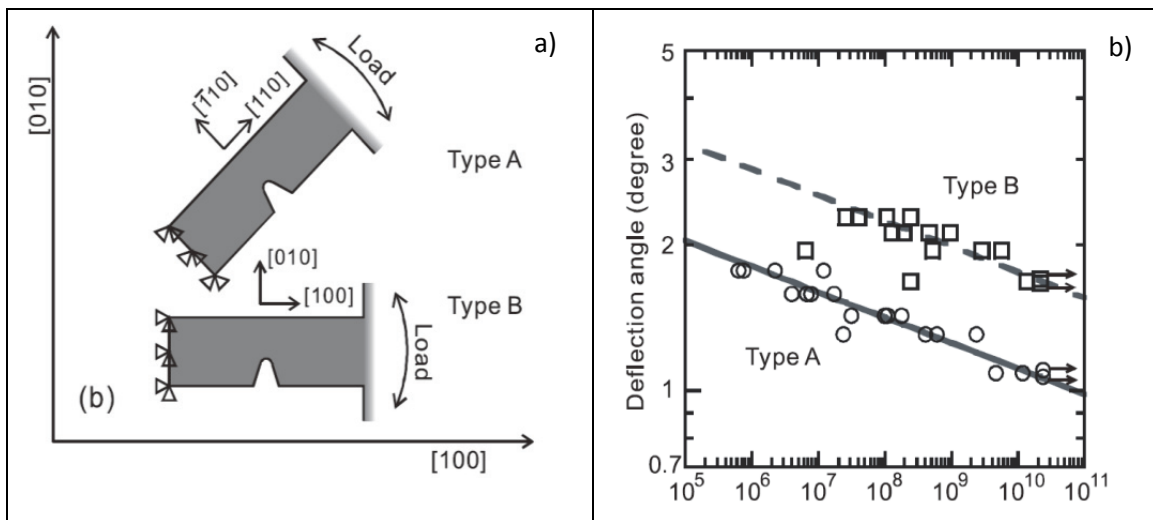


Fig 2.6: Fatigue performance of a) different orientation of SCS microbeams shown in b) [12]

From the results it can be seen that $\langle 100 \rangle$ oriented samples endured a higher strain amplitude than $\langle 110 \rangle$ samples at the same fatigue life. One reason for such anisotropy was the lower Young's modulus along the $\langle 100 \rangle$ direction which means lower bending rigidity as well as lower stresses than the $\langle 110 \rangle$ samples. It was also found that the ratio of normal stresses on the two most likely planes for cleavage ((111) and (110)) between $\langle 110 \rangle$ and $\langle 100 \rangle$ samples was equal to 1.51 for the same deflection angle indicating that $\langle 110 \rangle$ samples exhibit higher stress. The authors also examined fracture surfaces of both types of samples. The $\langle 110 \rangle$ oriented samples showed cleavage along the (110) plane while the $\langle 100 \rangle$ samples had the crack to zigzag across the specimen. Samples along $\langle 110 \rangle$ that exhibited longer fatigue life showed a mirror like (110) fracture surface. Samples with a shorter life showed bent surfaces connecting (110) and (111) planes.

2.2.3 Effect of surface roughness

The effect of surface roughness on fatigue behavior of SCS microstructures has seldom been studied. One study by Ikehara et al [50] investigates the effect of sidewall

morphology of samples similar to the device in figure 2.4. Samples from one wafer (wafer 1) had smooth sidewalls. Samples from another wafer (wafer 2) had rougher sidewalls exhibiting irregular vertical stripes. Concave etching damage near the top of sidewalls was also observed on samples from wafer 2 in the worst case. Samples from both wafers were tested in a controlled environment (23°C and 50% relative humidity) at a constant amplitude of oscillation and the resulting S-N curve is shown in figure 2.7. For wafer 2, closed squares indicate fracture initiating at the etching damage while open squares indicate fracture occurring elsewhere on the sidewall.

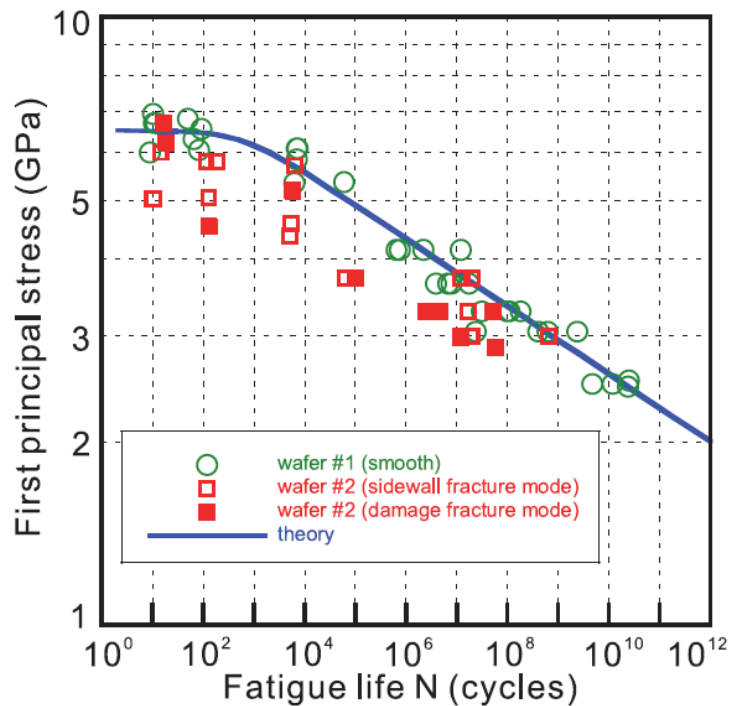


Fig 2.7: S-N for samples from different wafers. The solid line indicates the best fit based on samples from wafer 1 [50]

It can be seen that samples with smooth sidewall from wafer 1 showed a higher fatigue life for the same value of first principal stress as well as less scatter. These results indicate the importance of sidewall roughness in determining the fatigue behavior of SCS structures.

2.3 Concluding remarks

From the studies on factors affecting tensile and fatigue performance, it can be seen that surface roughness has a major impact on tensile and fatigue behavior of SCS microstructures. Smooth sidewalls mean higher fracture strength as well as longer

fatigue life. Another factor that determines both tensile performance and fatigue performance is crystal orientation. These two factors are then crucial in improving mechanical performance of SCS microstructures under tensile or fatigue loading and will be further investigated in the current study.

3. Review on sidewall roughness reduction techniques

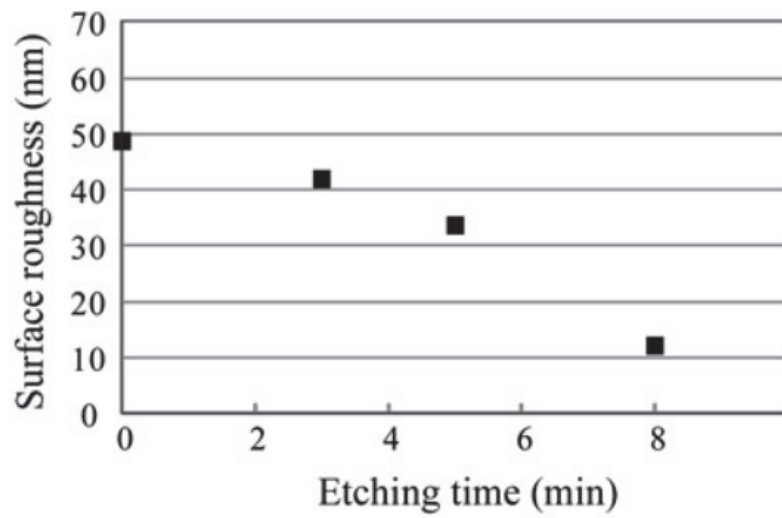
Many researchers have been investigating sidewall morphology and roughness improvement techniques of fabricated SCS microstructures for different purposes. Sidewall roughness improvement is crucial for MEMS components performance and reliability. In optical applications, sidewall roughness causes scattering losses in case of waveguides and micromirrors. In microfluidic applications, surface roughness can cause unsteady secondary flows in microchannels as well as influence capillary forces and surface tension. In mechanical transmission components that undergo contact like microgears, surface roughness can affect friction, running life and power consumption. Also, as discussed in the previous chapter, components that are subjected to tensile and fatigue loads may fail due to stress concentration locations because of rough sidewalls.

Many techniques have been developed to improve sidewall roughness including wet etching, thermal oxidation, hydrogen annealing and laser treatment.

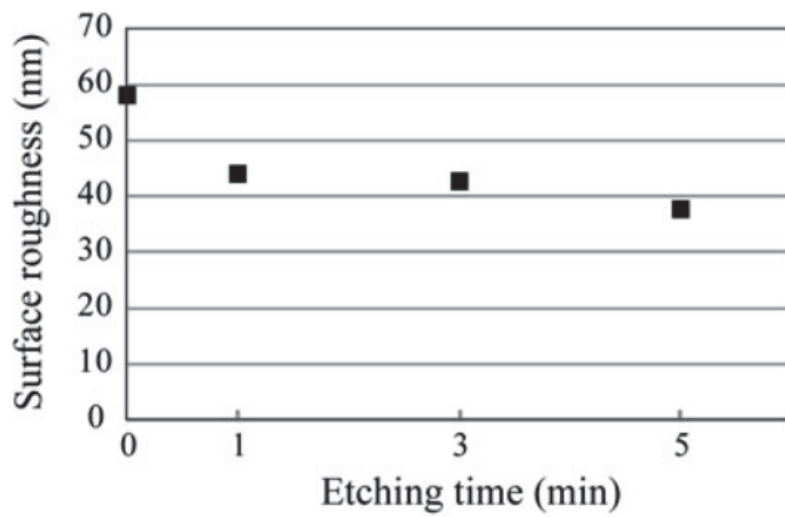
3.1 Wet etching

Wet etching is done by immersing the SCS microstructures in silicon etching solutions that would attack the peaks of the scallops on the sidewalls since they have high chemical reaction potential [51]. Wet etching using a 50% solution of KOH at 40°C was used to improve sidewall roughness developed on sidewalls of fabricated SCS microcantilevers [24]. Cantilevers were 10 µm wide, 37 µm thick and 500 µm long and were oriented along <110> and <100> direction. As shown in figure 3.1, sidewall surface roughness of <100> samples decreased from 49 nm to 12 nm while that of <110> decreased from 59 nm to 38 nm. These results were found to improve tensile strength as can be seen in figure 3.2. From these results, it can be noticed that the effect of KOH etching on improving sidewall roughness and strength was different between the crystal orientations. This could be related to anisotropic etching properties of KOH since it was reported that (100) surfaces have the least roughness among other orientations [24]. It was also noticed that differences in etch rates of KOH for different surface orientations exist with the (111) surface being as low as 5 nm/minute with 40% KOH solution etching at 70°C [52]. This method also requires that the whole chip or wafer carrying the structures to have their surface roughness improved be immersed in

KOH which might be detrimental to other components requiring high dimensional accuracy.



(a) Si{100} surfaces



(b) Si{110} surfaces

Fig 3.1: Effect of KOH wet etching time on sidewall roughness for different orientations of SCS microbeams [24]

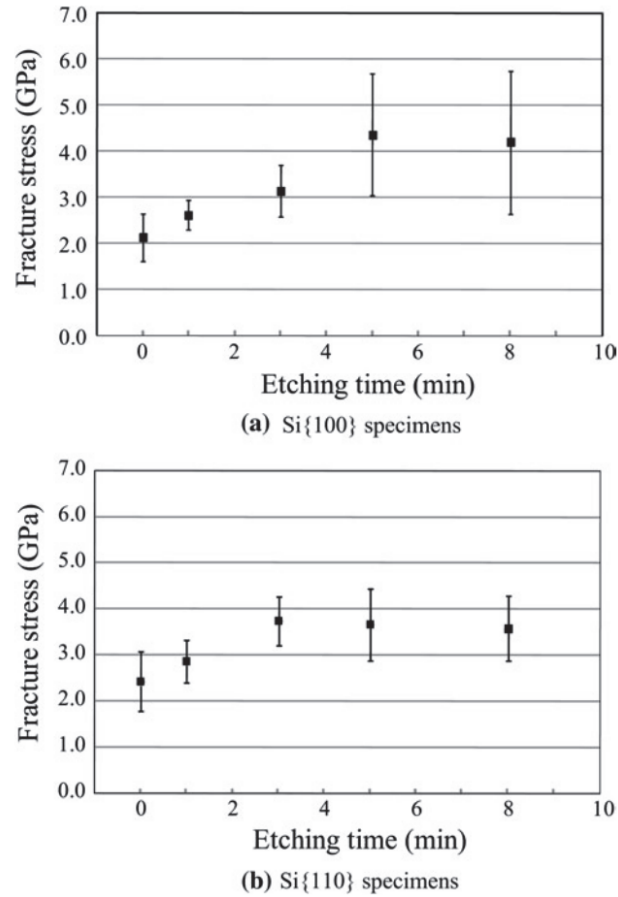


Fig 3.2: Effect of KOH wet etching time on fracture strength for different orientations of SCS microbeams [24]

3.2 Thermal Oxidation

Thermal oxidation techniques have shown to be effective in reducing sidewall roughness. The technique mainly depends on oxidizing the surface of the SCS microstructure with subsequent removal of the surface oxide leaving a smooth surface behind since scallops would be consumed in the reaction.

Wet thermal oxidation was used by Lee et al [25] to smooth waveguides oriented in the $\langle 110 \rangle$ direction on a (100) wafer. Wet oxidation was done for 43 minutes at 1000°C. Steps are shown in figure 3.3.

Sidewall roughness after oxidation smoothing was evaluated using AFM as shown in figure 3.4.

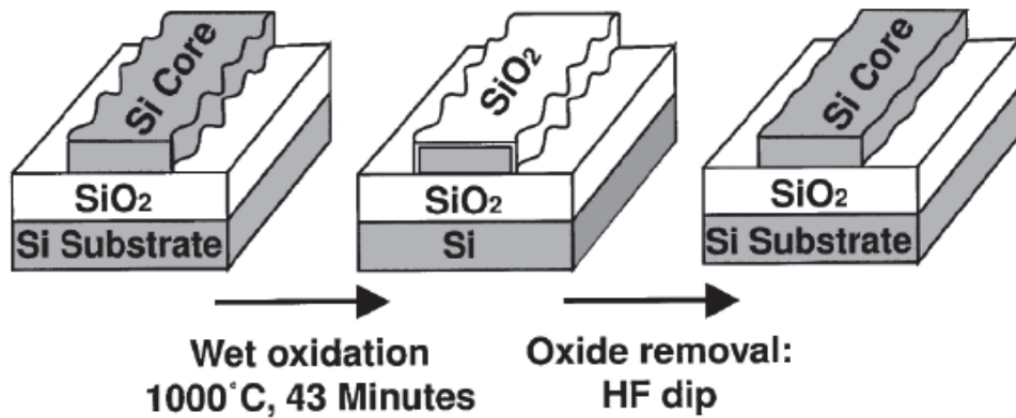


Fig 3.3: Surface smoothing by wet oxidation [25]

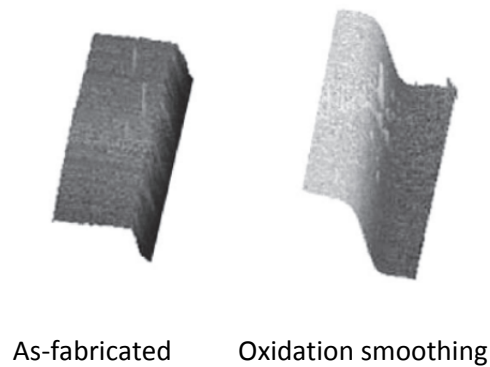


Fig 3.4: Surface profile before and after wet oxidation [25]

The resulting sidewall rms roughness was 10 nm for as-fabricated samples. With the oxidation smoothing step, the resulting rms roughness was 2 nm and the corners were rounded after oxidation smoothing.

Dry oxidation was used by Sparacin et al to improve waveguide performance [26]. Oxidation at 1050°C was performed for different periods of times and the sidewall roughness was measured using AFM as shown in figure 3.5. Buffered oxide etch (BOE) was used to remove the oxide layer before roughness measurements.

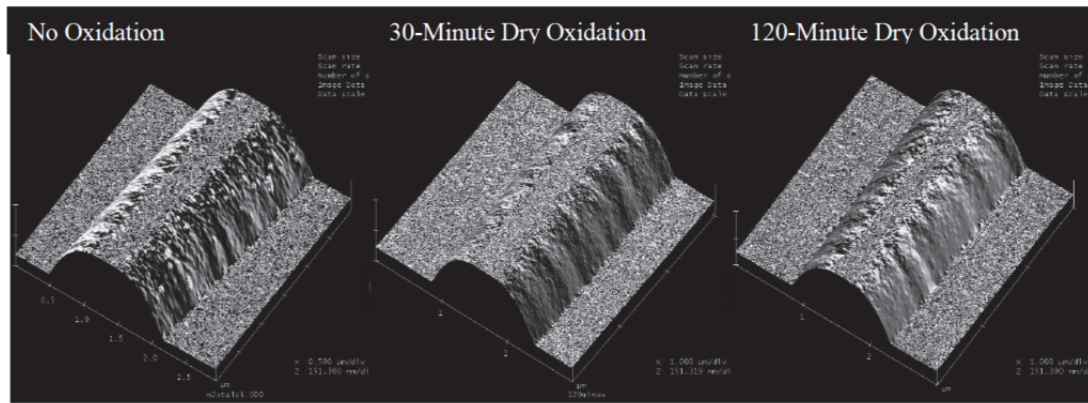


Fig 3.5: Surface profile before and after dry oxidation [26]

Roughness improved with oxidation time. Oxidation smoothing effect was discussed by attributing this phenomena to the Gibbs Thomson relation [51]:

$$\mu(k) = \mu(\infty) + \gamma\Omega k \quad 3.1$$

where $\mu(\kappa)$ is the chemical potential at a surface of curvature κ , $\mu(\infty)$ is the potential at a flat surface, γ is the surface energy, and Ω is the atomic volume. This relation means that peaks of sidewall roughness that have positive curvature have a positive potential for chemical reaction compared to grooves having negative curvature. Accordingly the peaks would be consumed in oxidation resulting in overall smoothness. One limitation of oxidation that is discussed by the same authors is that the oxidation rate decreases significantly with oxide layer thickness especially after a thickness of 20 nm as the oxide layer acts a barrier to further oxidation and smoothing. Oxidation in that case would need repeatable steps of oxide formation and removal.

Another problem to note is that the whole chip or wafer carrying the structures to have smoother surfaces need to be subjected to temperatures above 1000°C for thermal oxidation smoothing to take place. This high temperature could damage any metallic or polymeric components that may be present.

3.3 Hydrogen annealing

Hydrogen annealing is a process where silicon structures are heated up to a temperature of about 1000°C in a hydrogen atmosphere to promote a surface diffusion process whereby silicon atoms move to minimize the overall surface energy thereby smoothing the surface and rounding sharp corners as shown in figure 3.6 [28-31]

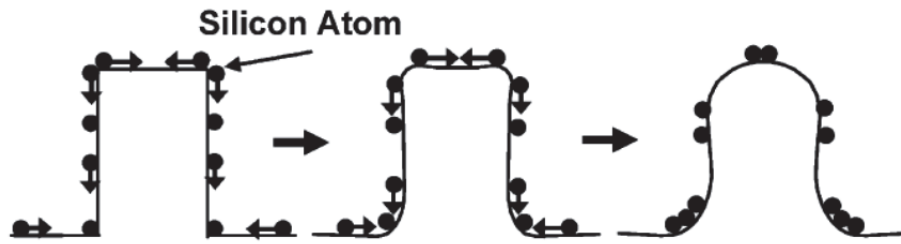


Fig 3.6: Mechanism of surface smoothing due to hydrogen annealing [28]

Lee et al [28] studied the effect of hydrogen annealing on various fabricated SCS microstructures by performing the annealing at 1100°C at 10 Torr for several minutes and observed the change in surface morphology after the treatment as well as measured resulting roughness on the sidewall of a 0.5 μm deep step by AFM. Examples of such structures are shown in figure 3.7 while AFM results are shown in figure 3.8.

AFM results showed a decrease in roughness from 20 nm for the sidewall of the as-fabricated step to 0.26 nm. Other studies also confirmed the reduction in surface roughness and rounding of corners [29,30].

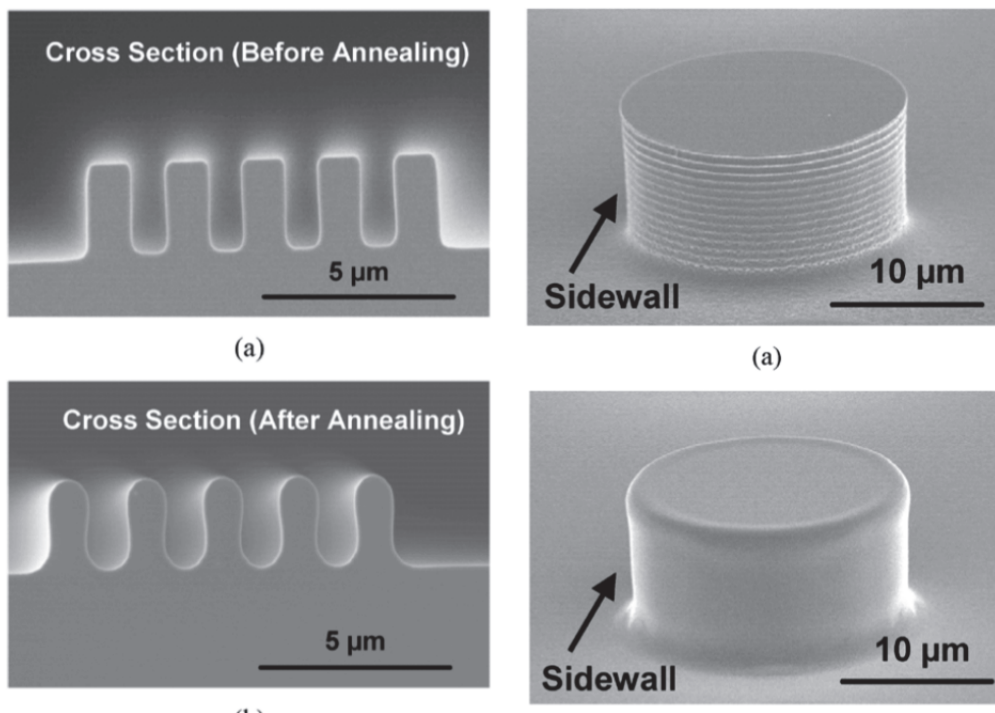


Fig 3.7: Trench and cylindrical patterns subjected to hydrogen annealing [28]

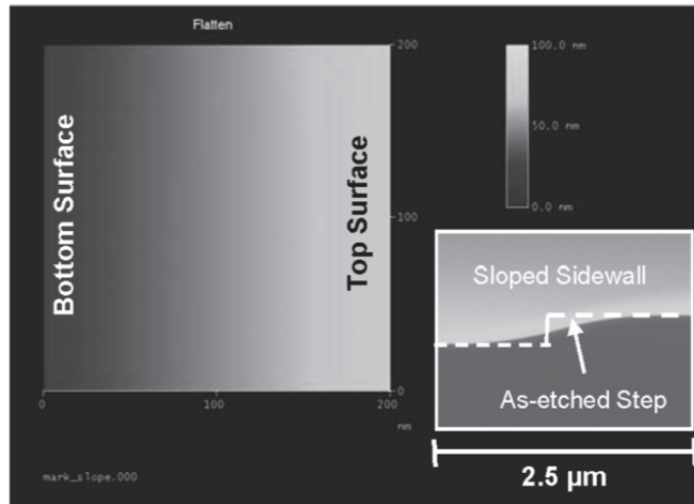


Fig 3.8: AFM profile image of a $0.5 \mu\text{m}$ fabricated step after hydrogen annealing [28]

Hydrogen smoothing has also been employed by Hajika et al[31] to study the effect on torsional strength of MEMS scanning mirrors. Hydrogen annealing was done at 1200°C for different annealing times. It was shown that the annealing time leads to better improvement in surface roughness as well as fracture strength as can be seen in figures 3.9 and 3.10.

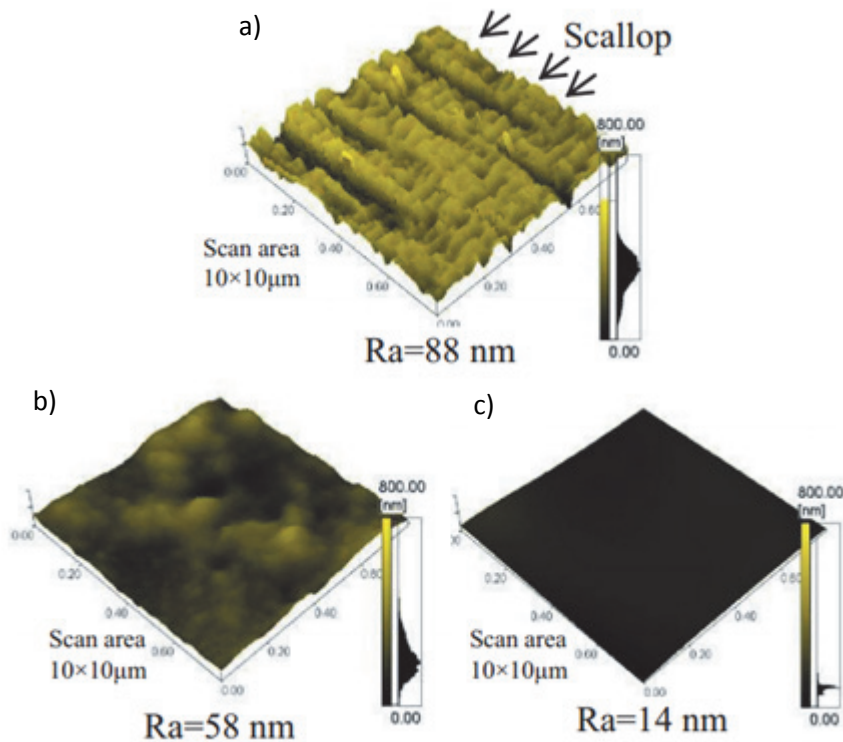


Fig 3.9: a) As-fabricated SCS sidewall surface, b) Hydrogen annealed surface for 30 minutes and c) Hydrogen annealed surface for 120 minutes [31]

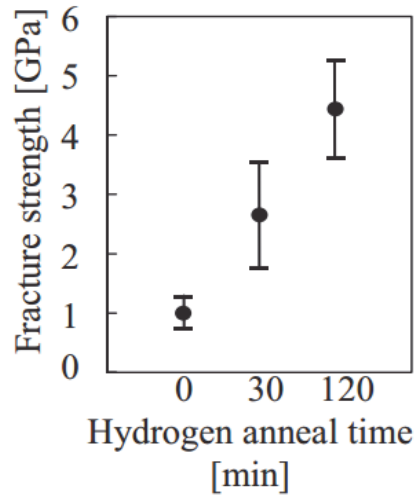


Fig 3.10: Fracture strength improvement due to hydrogen annealing at different hydrogen anneal times [31]

Hydrogen annealing is very promising for reducing surface roughness as has been observed however the high temperature needed ($>1000^{\circ}\text{C}$) would damage metallic or polymeric components on the chip

3.4 Laser annealing

Laser treatment for silicon wafers as well as other supported structures has been used for decades but has seldom been used for free-standing structures. Studies that investigated roughness improvement due to laser treatment focused on perpendicular irradiation of planar surfaces [33,34]. The smoothing mechanism of laser treated surfaces depends on surface tension driven flow of molten silicon [35].

Two studies have discussed laser treatment of sidewalls for the sake of roughness improvement for waveguide applications [35,36]. These two studies used a KrF excimer laser with a wavelength of 248 nm and a pulse duration of 25 ns. Samples were tilted in order to expose sidewalls for efficient laser treatment. Different laser energies, number of pulses as well as incidence angles were investigated and the roughness was measured using AFM on planar surfaces subjected to the same fabrication condition. Figure 3.11 shows the transformation of the ridge shape after laser treatment while figures 3.12 and 3.13 show the resulting roughness improvement as a function of tilt angles, number of shots and laser energies.

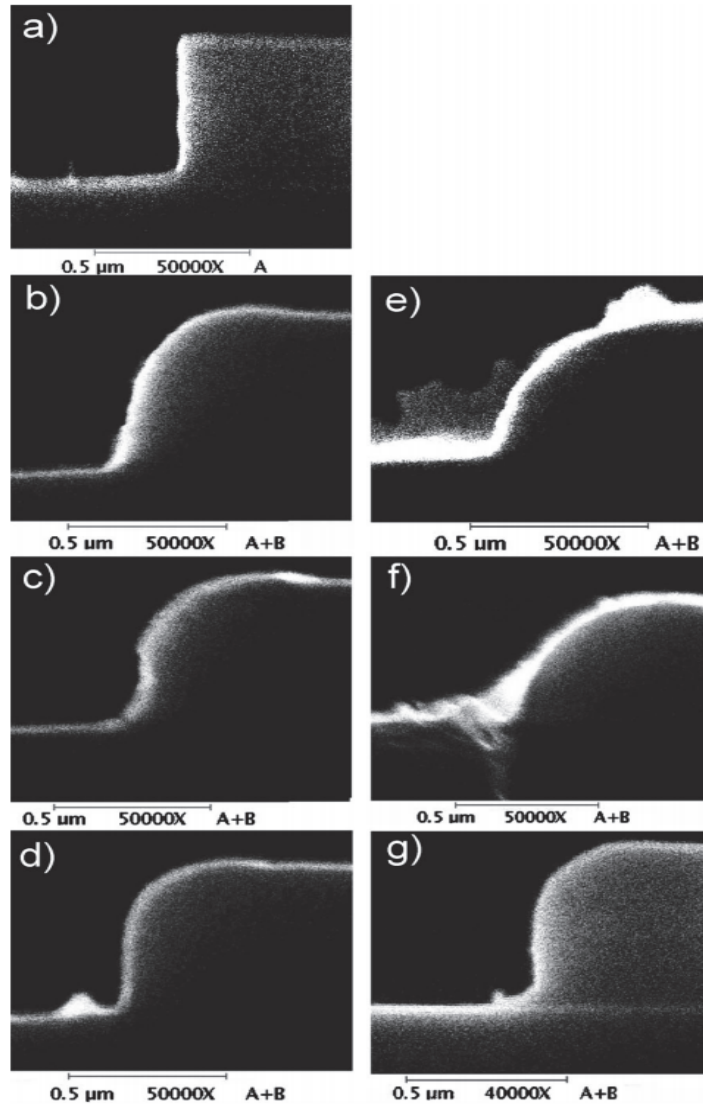


Fig 3.11: Cross sections of SCS waveguide. a) As-fabricated and laser treated at 1.4 J/cm^2 ,one shot at incident angles b) 45° , c) 60° d) 75° and 5 shots at the same energy at d) 45° , e) 60° and f) 75° [36]

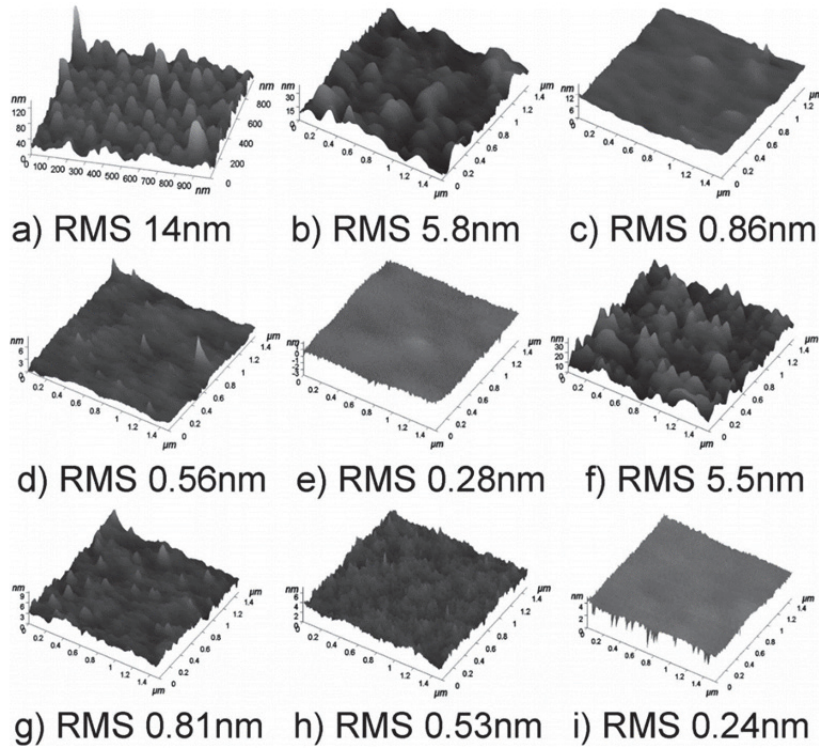


Fig 3.12: Surface roughness of flat SCS surfaces a) As-fabricated and laser treated surfaces subjected to 1 shot of laser at 1.4 J/cm^2 at the incident angles of b) 45° , c) 60° , d) 75° , e) 90° and 5 shots at the incident angle of f) 45° g) 60° , h) 75° and i) 90° [36]

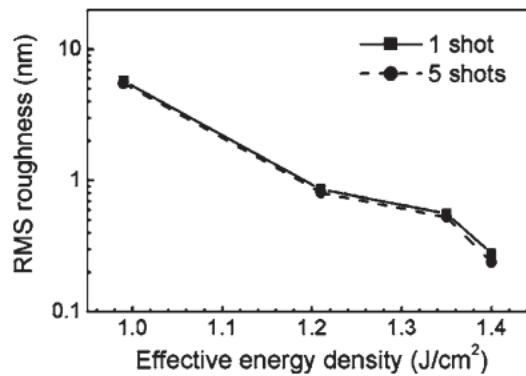


Fig 3.13: Effect of number of pulses at different laser energies on RMS roughness [36]

The rms roughness decreases significantly with the laser energy and with the incidence angle. The authors claim that the incidence angle determines the amount of absorbed laser energy by the irradiated surface. Higher laser energy that increases the temperature is also important since it can lower the viscosity of the melt and cause it to flow easily smoothing and reforming the irradiated surface. The major parameter that determines the roughness is the absorbed laser energy. Finally the authors claim that

there is an upper limit for laser energy that reduces the sidewall roughness but does not deform the shape of irradiated surfaces and a lower limit that can smoothen the irradiated sidewalls.

Concerning laser irradiation of free-standing structures, the treatment energies were kept below the melting threshold and was done mainly on top or bottom surfaces for solving stiction problems and curvature adjustment [53-56]. It was claimed that high energy laser treatment on free-standing microstructures would lead to thermal gradients across the thickness of samples. This is quite risky since high temperatures would mean high strains near the surface that can reach the material's yield strength.

For improving sidewalls roughness of any fabricated structures, high laser energies above melting threshold would be required. This presents a challenge in the case of free-standing structures. Another concern for laser treatment of sidewalls is efficient exposure to laser since neighboring structures could easily shadow sidewalls and prevent full exposure.

3.5 Choice of sidewall roughness improvement technique

The comparison between different methods to improve sidewall roughness is shown in table 3.1.

From table 3.1, laser treatment has an edge over other techniques in terms of localized treatment. Using a small laser spot size it is possible to improve sidewall roughness of target structures without damage to other structures on the chip or wafer since no global thermal treatment is required that could introduce damage to existing polymeric or metallic components. The processing time for laser treatment is also shorter compared to other methods since the pulse duration is within nanoseconds and the frequency can be controlled to minimize the time between pulses. The cost of laser treatment equipment and setup is however higher compared to other techniques. For the current study, laser treatment is employed as the method for improving sidewall roughness. The main challenge involved with laser treatment is to irradiate free-standing structures at high energies causing surface melting without fracture as well as efficient exposure of sidewalls. These challenges would be addressed by developing an appropriate experimental process and setup.

Table 3.1: Comparison between different sidewall roughness improvement techniques

Treatment technique	Minimum RMS roughness reported (nm)	Temperature	Localized treatment	Processing time	Cost ranking (1 corresponding to lowest cost)
Wet etching	0.7	<120°C	X	Minutes	1
Thermal oxidation	0.5	1100°C	X	Hours	2
Hydrogen annealing	0.11	1100°C	X	Minutes	3
Laser treatment	0.24	Room temperature	O	Seconds	4

4. Devices and experimental methods

4.1 Sample description and preparation

Two types of samples were fabricated on a (100) SOI wafer for tensile and fatigue testing. The test part of both types of samples were oriented along $\langle 110 \rangle$ and $\langle 100 \rangle$ directions. The samples are shown in figure 4.1

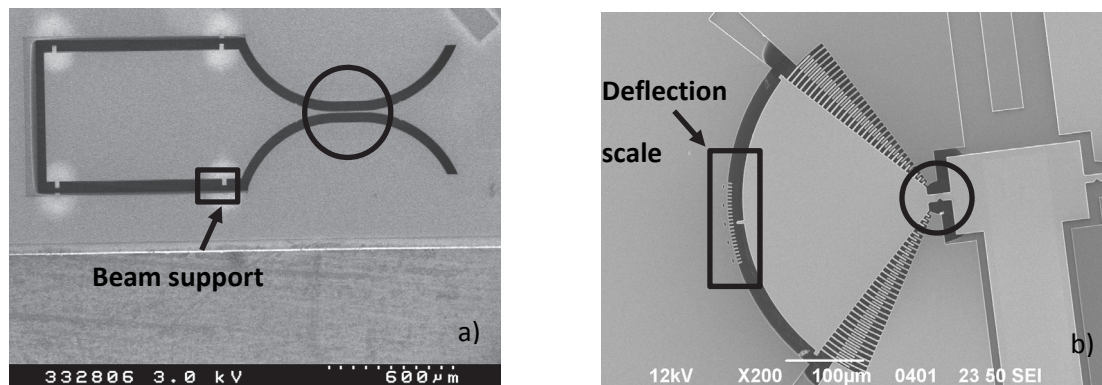


Fig 4.1: Test samples; a) tensile test sample and b) fatigue test sample

Figure 4.1a shows the sample used for tensile testing. The circled part is the test part having a gauge length of $120 \mu\text{m}$ and a cross section of $5 \times 5 \mu\text{m}$. The rectangular part with a bigger surface area is used for gripping during tensile testing. That part is supported using four beam supports on both sides that are cut using laser prior to tensile testing as shown in figure 4.1a. The sample shown in figure 4.1 b is the fatigue test sample with the test part encircled having a notch in the center of it. It has been used extensively for fatigue studies by Ikehara et al [10,12]. The test part has a length of $30 \mu\text{m}$, a width of $10 \mu\text{m}$ and a thickness of $5 \mu\text{m}$. The notch has a depth of $4 \mu\text{m}$ and an angle of 90° . The notch was designed to have a sharp corner at the tip but after fabrication a rounded notch tip is observed. The fatigue test structure has a bigger fan shaped mass with a radius of $250 \mu\text{m}$ having two sets of comb electrodes on both sides and a deflection scale. Electrodes are $2 \mu\text{m}$ wide and $1.5 \mu\text{m}$ in the gap. One set of comb electrodes is used for actuation while the other is used for sensing while the device is tested under cyclic in plane loading. The mass provides adequate vibration amplitude during resonance. The design resonance frequency value is 40 kHz . Differential sensing is used to detect the output by comparing the signal from the moving sensor comb to the identical reference comb as shown in figure 4.2. A deflection scale is used to measure the deflection angle during actuation.

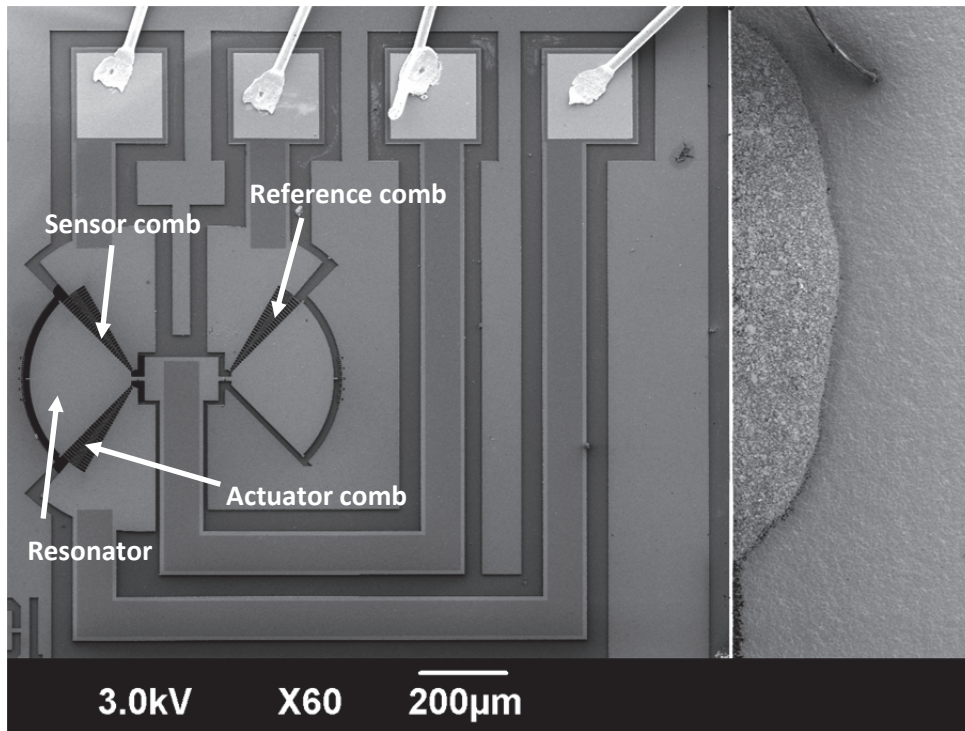


Fig 4.2: Layout of the fatigue test chip

Both types of samples were fabricated from SCS with boron concentration of 1×10^{17} / cm^3 using high resolution lithography of $0.6 \mu\text{m}$ using successive steps of deep reactive ion etching (DRIE). The substrate under the movable parts was removed by backside DRIE followed by wet etching of the buried oxide using HF. After fabrication, the wafers were diced into chips using laser dicing [14,16]. High magnification images were taken at the sidewall of both types of samples as shown in figure 4.3. From the figure 4.3 it seems that sidewalls from both samples exhibited significant scalloping due to the fabrication process. From field emission scanning electron microscope (FESEM) images scallops had a depth of about 46 nm and a pitch of 120 nm. High magnification images were also taken for both the top surface and bottom surface of samples as shown in figure 4.4. Top surfaces seemed to be slightly damaged may be due to ion bombardment during backside DRIE while bottom surfaces were smooth for most samples except that some samples had etch pits on the bottom surface probably from wet etching of the buried oxide layer. The chips were mounted on ceramic packages using silver paste and wire bonding.

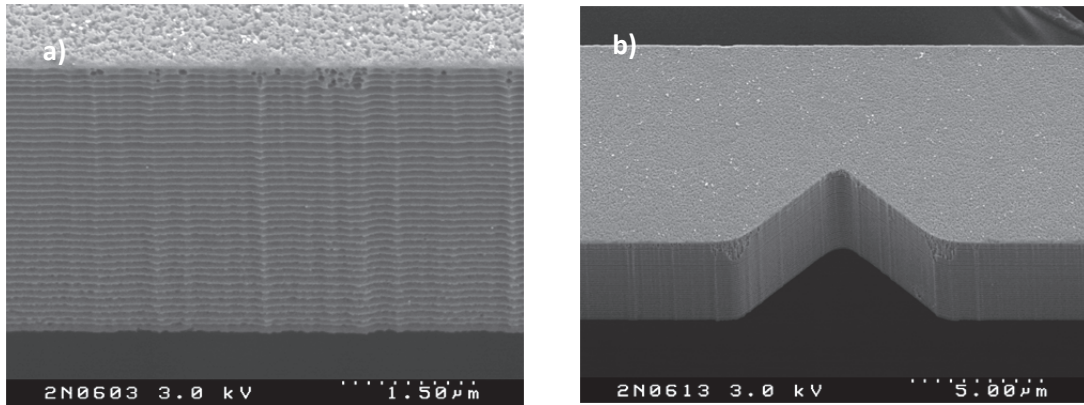


Fig 4.3: Sidewall view of the a) tensile and b) fatigue test samples

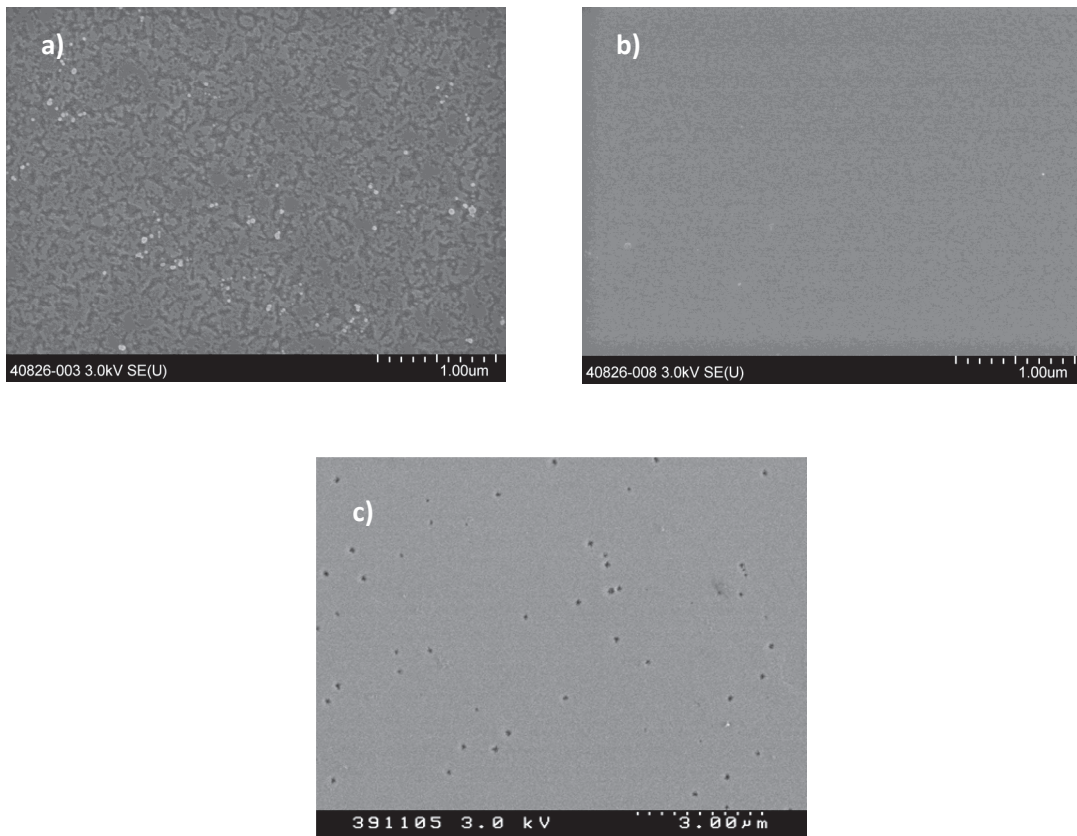


Fig 4.4: FESEM images of a) Top surfaces, b) bottom surfaces and c) Bottom surfaces with etch pits

4.2 Experimental procedure

The first stage of the experimental procedure was a conditioning stage to find a laser treatment condition that is expected to achieve an improvement in sidewall roughness and mechanical performance. Perpendicular laser treatment on planar surfaces was

performed but on top surfaces of tensile test samples to investigate basic effects of laser irradiation on free-standing structures surface morphology, roughness, crystallinity and residual stresses. For the fatigue test samples that have notches, the notch profile determines the stress concentration factor and the applied stress on the samples during testing. For that reason and since crack initiation is supposed to occur at the notch for fatigue test samples, sidewall morphology assessment was performed using irradiated notched sidewalls of fatigue samples. The final stage of the experimental procedure was the tensile and fatigue testing after choosing the optimum laser treatment conditions. During this stage as-fabricated and laser treated samples were tested and the mechanical properties were compared to evaluate the effect of laser treatment. In tensile testing, fracture strength was chosen for comparison and the fracture behavior was also studied by FESEM observation. In case of fatigue testing, the fatigue life of as-fabricated and laser treated samples subjected to the same loading condition was compared as well as fracture behavior.

4.3 Evaluation of irradiated samples

Quantitative analysis on the resulting surface roughness of planar surfaces was done using AFM (Nanowizard III) to evaluate laser treatment effect on surface roughness of the slightly damaged top surfaces shown in figure 4.4a. The change in surface average roughness for the top surfaces was examined for a scanned area of $1 \mu\text{m}^2$ near the center of the sample width. Evaluation of the effect of laser on sample crystallinity as well as residual stresses on the planar surfaces was conducted using laser Raman microspectroscopy (HORIBA Jobin Yvon, Labram HR-800) using Ar laser (488 nm) having a spot size of $1 \mu\text{m}$. Three locations along the top surface of the laser treated gauge length of tensile test samples were measured. Curve fitting and smoothing techniques were done for the Raman spectra. Evaluation of sidewall morphology of notched fatigue samples after laser treatment was done qualitatively using (FESEM) (Hitachi SU-8000 and S-4500) images since it was difficult to quantitatively measure sidewall roughness due to space limitation. The choice of laser treatment condition should take into consideration the improvement in surface roughness and preservation of the shape of notch shape.

4.4 Finite element analysis

The finite element analysis (FEA) was performed for the sidewall irradiation using ANSYS to evaluate the temperature distribution. A 3D model was constructed for the fatigue samples considering half of the test part starting at the notch tip. A 2D model was constructed for the tensile test samples for simplicity. The transmitted light intensity into silicon is governed by the Beer-Lambert equation [57]:

$$I(z, t) = (1 - R)I_o(t) \frac{e^{-z/\delta}}{\delta} \quad 4.1$$

where $I(z, t)$ is the laser intensity at a depth z from the surface and time t , R is the reflectivity, $I_o(t)$ is the laser intensity at the surface and δ is the penetration depth of KrF laser in silicon taken to be 6 nm[57]. The model considered melting of silicon by using parameters corresponding to solid and liquid silicon as shown in table 4.1. Latent heat of fusion was not considered during the analysis. The exact code used for modeling can be found in Appendix A.

Table 4.1: Material properties for solid and liquid silicon

Material Property	Solid Silicon	Liquid silicon
Thermal conductivity ($\text{W} \cdot \text{m}^{-1} \cdot \text{K}^{-1}$)	148	200
Density ($\text{kg} \cdot \text{m}^{-3}$)	2320	2500
Heat capacity ($\text{J} \cdot \text{kg}^{-1} \cdot \text{K}^{-1}$)	710	680

4.5 Laser annealing

Tensile and fatigue test samples were irradiated using a Coherent LAEX-1000 KrF (248 nm) excimer laser source with a pulse duration of 30 ns. As seen from figure 4.5, the laser system has telescopic lenses to adjust the beam short and long axis, homogenizer lenses to adjust the beam intensity, a field lens to collimate the light beams, a mask to control the spot size and a projection lens to focus the laser spot to the required size. Samples are attached to the sample holder, which is mounted on a two axis stage for the alignment.

The laser spot has a homogenous energy distribution over the spot size within 5%. The spot size at the mask is 20 mm square and the reduction ratio is 8 leading to a spot size

of about 2.5 mm square on the sample surface. For localized laser treatment a mask is used to reduce the spot size at the sample surface. The mask allows a nominal spot size of $250\ \mu\text{m} \times 100\ \mu\text{m}$ for tensile test samples to cover only the test part while for the fatigue samples it allows a nominal spot size of $100\ \mu\text{m}$ square to cover only the notch area.

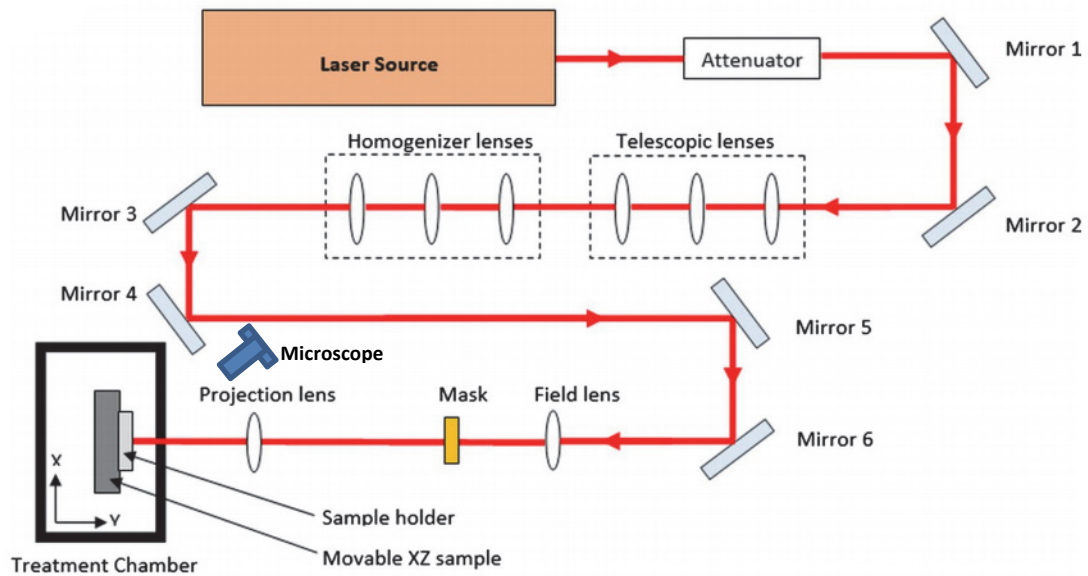


Fig 4.5: Laser system layout

During the conditioning stage the laser energy values was varied between $0.8\ \text{J}/\text{cm}^2$ and $4\ \text{J}/\text{cm}^2$ and the number of pulses between one and 1000 pulses. The pulse rate was kept constant at 1 Hz and the experiments were done in air at 1 atm and at room temperature. For efficient exposure of samples sidewalls, the chips carrying the samples to be irradiated were tilted according to the procedure suggested in section 3.4. A sample holder was designed for the purpose of tilting the samples. A schematic of the sample holder is shown in figure 4.6.

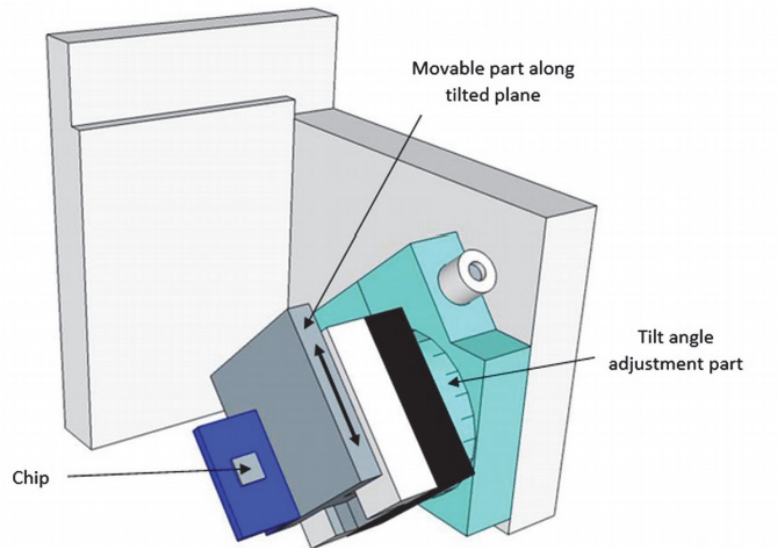


Fig 4.6: Sample holder

The tilt angles chosen for investigation were 45° and 65° . A tilt angle of 45° corresponds to both the top surface and sidewalls having the same laser treatment. A tilt angle of 65° on the other hand was the maximum possible tilt angle for exposing the sidewalls to the laser due to neighboring structures.

Tensile test samples were irradiated from both sides as shown in figure 4.7a while fatigue test samples were only irradiated from the side with notch only where the crack should initiate as shown in figure 4.7b.

For precise aiming at the test part for both types of samples an optical microscope was used to guide the laser.

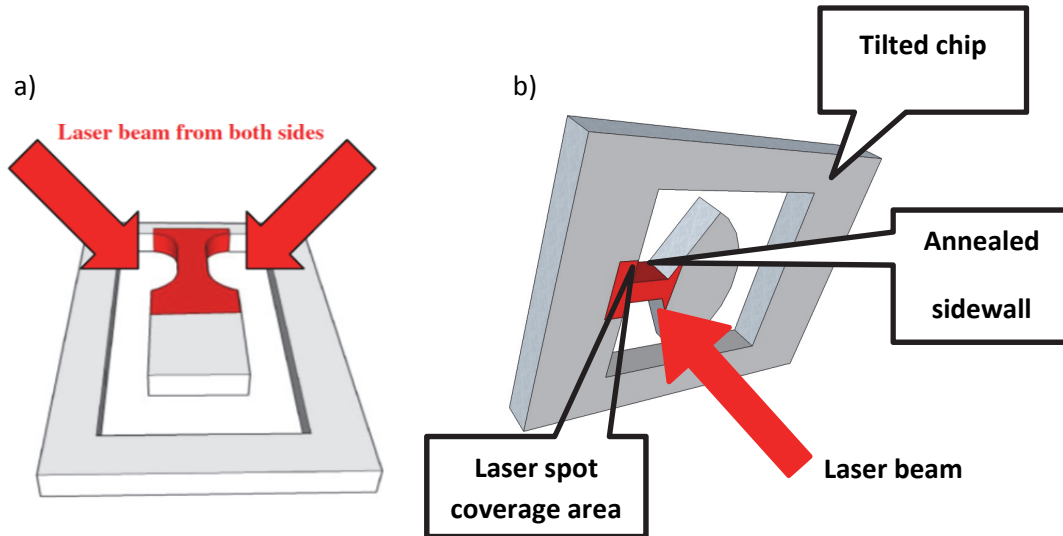


Fig 4.7: Schematic test setup for tilted irradiation of a) tensile and b) fatigue test samples

4.6 Tensile testing

As-fabricated samples as well as laser treated samples were tensile tested until fracture. The force at which the fracture occurs is divided over the cross sectional area ($25 \mu\text{m}^2$) to compute the strength. The test was done in air at 1 atm. The tensile test apparatus uses electrostatic force gripping of the bigger grip part attached to the test part as mentioned previously under section 4.1. A schematic of the test apparatus is shown in figure 4.8. Voltage is applied between the probe and the free-standing sample by locating the grip part under the probe using an optical microscope. Due to the opposite charge between the grip part and probe they are attached together by electrostatic force. The movable stage pulls the specimens to apply tensile force until fracture with the load cell monitoring the force applied during the test.

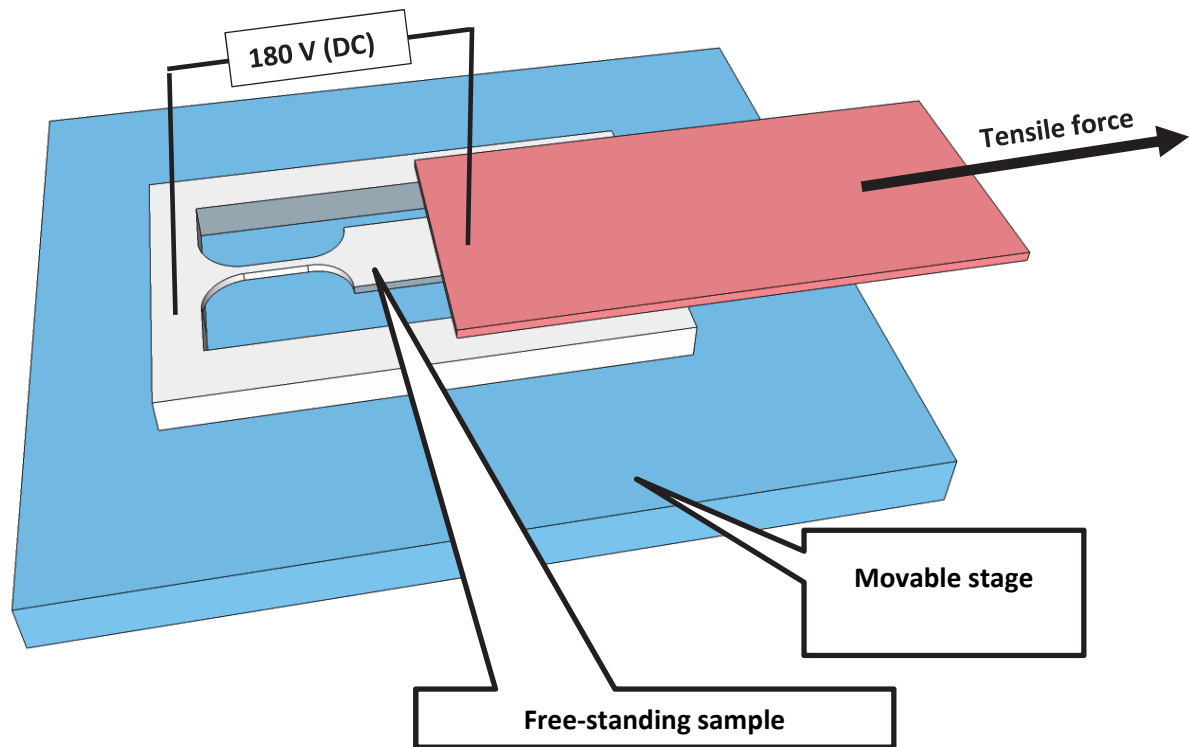


Fig 4.8: Schematic of tensile test setup (Not drawn to scale)

4.7 Fatigue testing

Due to the significant effect of environment on fatigue performance as discussed in section 2.2.1, fatigue testing of as-fabricated and laser treated samples was performed in a controlled environment oven at a temperature of 25°C and a relative humidity of 50%. First, a sweep test was done over a range of frequencies to determine the exact resonance frequency of the sample. The actuation voltage was then varied to calibrate the relationship between the deflection angle of the resonator and the applied voltage by monitoring the deflection scale on the mass under an optical microscope. The desired deflection amplitude was then used for both as-fabricated and laser treated samples by applying the fixed corresponding actuation voltage.

Open loop fatigue testing approach was adopted in which a voltage was applied at the resonance frequency of the sample and amplified via a high voltage amplifier for actuation with the output signal from the sensor and reference combs converted to voltage by the charge amplifier and then amplified with the differential amplifier to

detect motion of the resonator. Monitoring of the actuation signal and the output signal was done on an oscilloscope. The output signal amplitude as well as the resonance frequency of the test structure were also monitored and recorded over time on a computer via rms-dc converter and f-v converter, respectively. Fracture was indicated by a zero output signal. Fatigue life until fracture was calculated in the number of cycles by multiplying the resonance frequency and the time until fracture. Figure 4.9 is a schematic of the test setup. The sample board with its components was put in the controlled environment oven while the monitor board was kept outside.

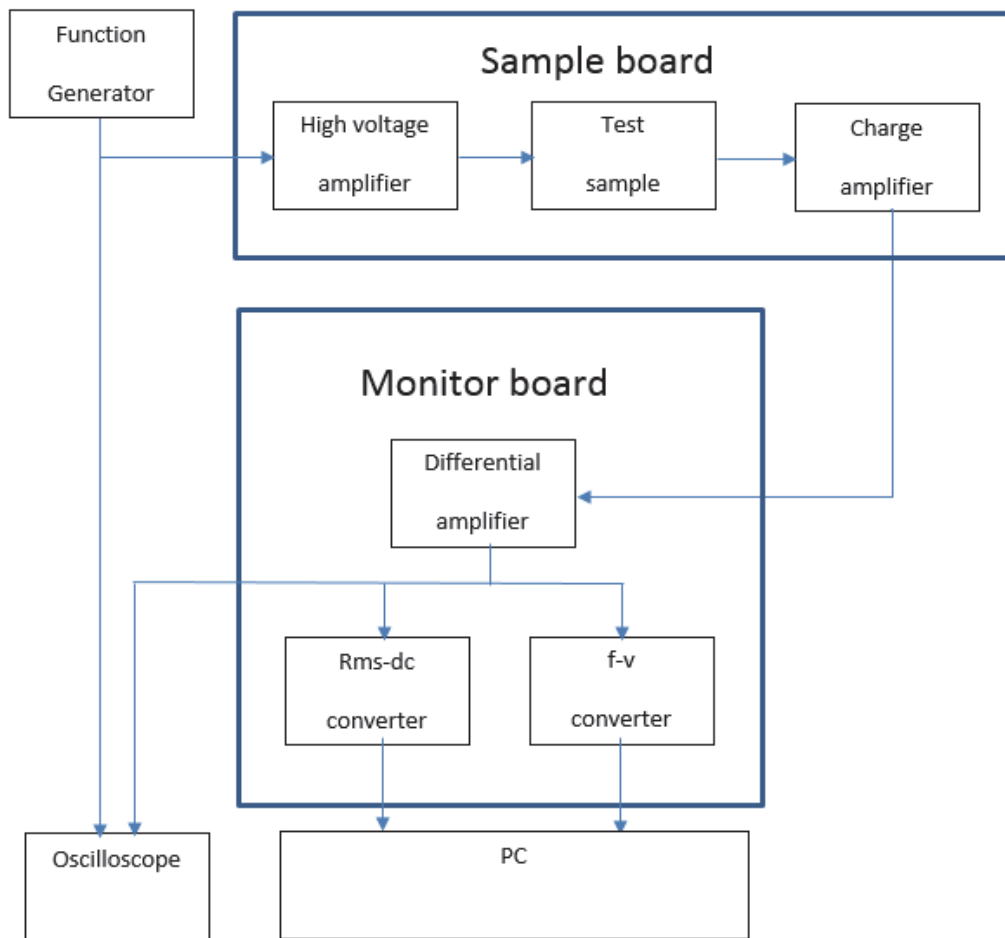


Fig 4.9: Layout of fatigue testing circuit

5. Localized laser treatment on free-standing SCS structures

This chapter discusses the conditioning stage where different laser treatment parameters (laser energy and number of pulses) are varied in order to study the effect on topology, morphology and crystallinity. From this stage, conclusions can be made regarding which conditions to be used for mechanical test structures.

5.1 Laser irradiation at high laser energies without sample fracture

Preliminary laser treatment experiments with no mask led to fracture of fatigue test samples at laser energies as low as 0.16 J/cm^2 . The laser spot covered the whole chip carrying the structures with fracture always occurred at the notch even at a single pulse. It is thought that fracture occurred due to out of plane bending by the mechanical shock caused by the energies absorbed on the fan shaped mass. Although the expected temperature rise along the top surface due to 0.16 J/cm^2 of laser energy is about 200 K, the sudden contraction and expansion can lead to vibrations. Although the calculated static deformation caused by the temperature rise is within nanometers, the expected acceleration of the top surface is within 10^6 - 10^7 m/s^2 due to the pulse duration being 30 ns [58-60]. Since the fatigue test structures can be modeled as a beam with the end mass, such acceleration of the mass would cause a significantly high force and accordingly a bending moment that could lead to failure at low energies.

By using localized irradiation the mass was kept at room temperature and only the silicon beam was irradiated leading to a successful treatment. No fracture occurred with energy values that go up to 4 J/cm^2 . For energies higher than 4 J/cm^2 , samples fractured even for single pulse treatments. We believe that localized laser treatment by controlling the spot size was responsible for the successful treatment of free-standing structure without fracture.

5.2 Temperature distribution

Fig. 5.1 shows the calculated temperature distribution for a single pulse of laser at 1.6 J/cm^2 at 65° tilt angle at the moment of maximum temperature for a fatigue test sample. Half of the test part is considered for modeling as shown in the inset. The temperature on sidewalls is higher than the melting temperature of silicon (1687 K) with the maximum being 1963 K near the top surface indicating that melting has

occurred on sidewalls. The temperature is highest near the top surface and decreases with thickness. The temperature at the notch tip is lower than the surrounding area and lower than the melting point of silicon with the temperature near the top surface being highest as was observed along sidewalls.

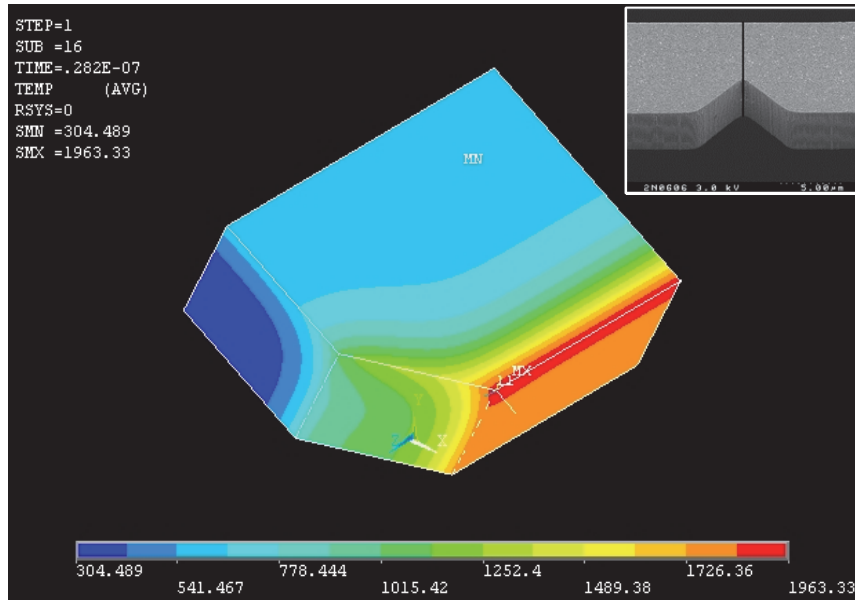


Fig 5.1: Temperature distribution due to a single laser pulse at 1.6 J/cm^2 at 65°

The FESEM image of a specimen annealed at the same condition in figure 5.2 shows that scallops disappear on sidewalls completely but traces of scallops can still be observed at the notch tip as we move downwards from the top surface. This confirms the trend observed from the FEA. The FESEM image however indicates that melting has occurred at the notch tip especially near the top surface while FEA results shows a lower temperature than the melting point at the notch tip. This might be due to a lower reflectivity value used in the model since it is based upon assuming polished surfaces which is not true for the silicon sidewalls that have considerable roughness due to the scallops present which might lead to more energy being absorbed than was calculated in the model.

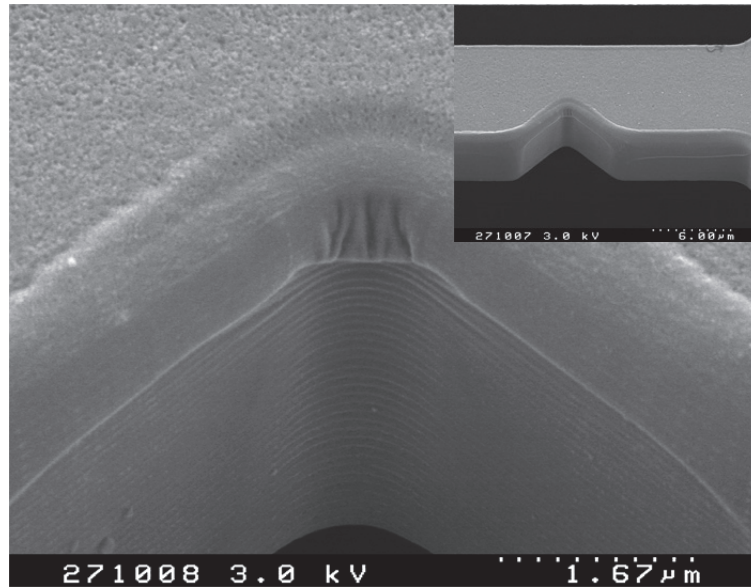


Fig 5.2: FESEM image of a fatigue test sample subjected to a single pulse at 1.6 J/cm^2 tilted at 65°

5.3 Effect of energy and number of pulses on sidewall morphology

Figure 5.3 shows the morphology of irradiated sidewalls of fatigue samples due to different combinations of laser energy and number of pulses. Up to 1.2 J/cm^2 sidewalls show improvement in roughness whereas the notch area did not improve as shown from figures 5.3 a,c and d. Sidewalls showed better roughness mainly at top edges while traces of scallops were still present at lower parts. This agrees well with the temperature trend observed in FEA where top edges have higher temperature than the rest of the sidewall. With 1000 pulses or more, columnar structures grew in a direction parallel to the laser beam. These structures might have occurred through ablation and deposition [61,62].

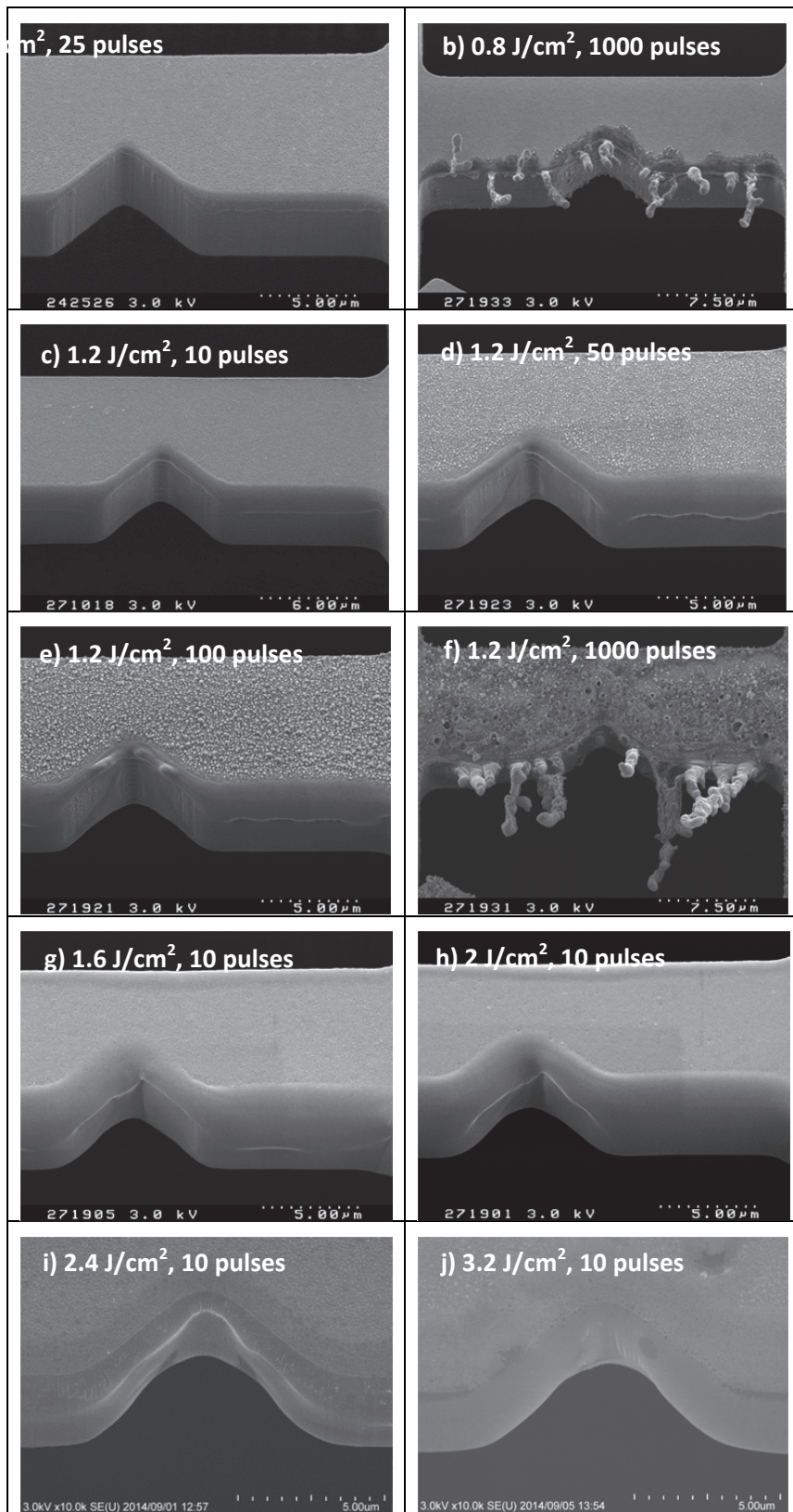


Fig 5.3: Sidewalls of fatigue test samples subjected to different laser treatment conditions

For energy values between 1.6 J/cm^2 and 2.4 J/cm^2 , the roughness of the notch area improved significantly without much distortion to the notch shape indicating melting

at the notch although traces of scallops can be seen at the notch tip especially at the lower energy values within that range. Sidewalls on the other hand show smooth surfaces with no traces of scallops. Vertical ridges were observed at the tip of the notch within that energy range. At higher energies and multiple pulses (3.2 J/cm^2 , 10 pulses), these ridges disappear as can be seen from figure 5.3j. A white line is also observed across the notch area and sidewalls of samples up to 2 J/cm^2 . The line however moves further downwards, fades away and completely disappears with higher laser energies and pulses. The tilting causes the development of a temperature gradient along the sidewalls having the highest temperature near the top surface as can be seen from figure 5.1. The white line appearing on sidewalls might be caused by Marangoni flow pushing molten silicon from the top to the bottom edge along the sidewalls as indicated by the white line moving downwards as the laser energy and number of pulses increase as seen from figure 5.3 [62-65]. From Figure 5.3c, 5.3d and 5.3e the white line moves downwards as the number of pulses increases from 10 to 50 but does not seem to move further as it increases to 100 at 1.2 J/cm^2 . As the laser energy increases, however, the line moves further downwards as can be seen from figure 5.3c, 5.3g and 5.3h with the white line totally disappearing at higher energies above 2.4 J/cm^2 as can be seen in figure 5.3j. At energies above 2.4 J/cm^2 however, significant increase in notch radius occurred. The significant increase in notch radius might be related to the shape of the notch having a wide angle that causes a large area to be subjected to laser and accordingly more molten silicon that moves.

5.4 Effect of energy and pulses on top surface morphology

A single pulse of 2 J/cm^2 sample was compared with a 10 pulses sample. Figure 5.4 shows the top surface morphology. The single pulse sample has a trench at the middle of the beam that disappears at 10 pulses. For higher energy values, no trenches were observed even for single pulses. This observation also suggests the occurrence of Marangoni flow on planar surfaces as was observed with sidewalls in the previous section and indicates the development of a temperature gradient on the surface whereby the center has a higher temperature than the edges. An explanation of this behavior has been proposed in literature that Marangoni flow pushes molten silicon outwards causing a depression at the center region and heightening the liquid at the periphery until the surface temperature gradient decreases. This molten silicon flows towards the edges having a higher surface tension. Marangoni flow was observed in

other studies for the case of Gaussian laser beams having a nonhomogeneous energy distributions over the laser spot unlike the current study where a homogenous energy spot is used [62-65]. It could be concluded that a temperature gradient is developed on the planar surfaces although a homogenous energy laser spot is supposed to cause a homogenous temperature distribution on the irradiated surfaces. The temperature gradient on planar surfaces could have been developed due to the temperature gradient developing along the sidewalls that would cause the molten liquid at the highest temperature near the top surface to move downwards along sidewalls. This would lead to a decrease in the temperature at the top edges and would cause a temperature gradient development on the top surface. Marangoni flow on the top surface seems to be only a transient effect since no trench is observed at higher energies or number of pulses corresponding to longer melt times. As the melt time increases, capillary forces will dominate due to surface deformation and will restore the shape of the surface pushing the liquid silicon back to the center until the trench congeals at sufficient melt time. Depending on the cooling rate, the shape of the solidified surface will be decided which will be that of the solidified melt [62-65].

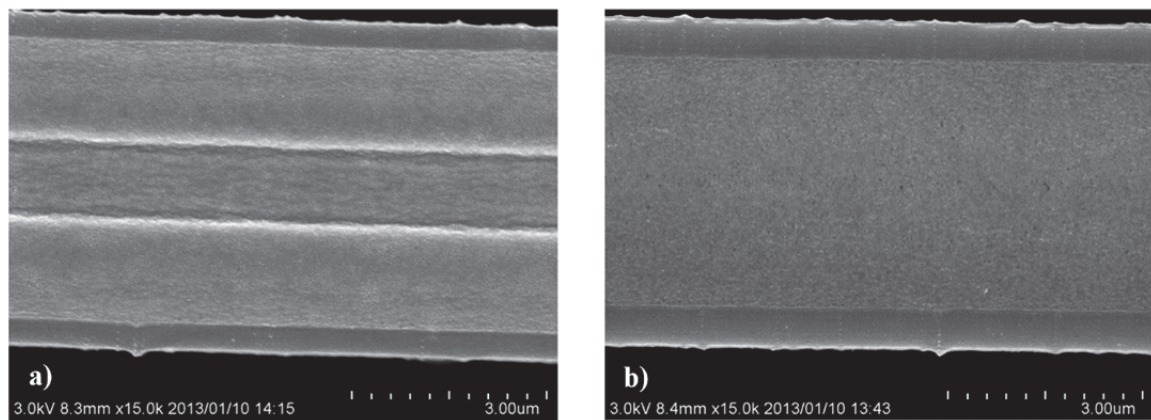


Fig 5.4: Top surface of tensile test sample subjected to 2 J/cm^2 of laser energy for a) one pulse and b) ten pulses

In order to investigate the effect of laser energy, different samples were treated at different laser energies with the number of pulses kept constant at 10. FESEM images for top surfaces are shown in figure 5.5. No change in morphology could be noticed up to 2.8 J/cm^2 (figure 5.5b) when particles start to form on the surface at the midsection. As the laser energy increases, these particles move further to the edges while the top surface roughness seems to improve in the central region as can be seen in figures 5.5c

and 5.5d. It was also noticed the center regions of the beam became darker than the edges. Such observations were also made by Nayak et al [66] who observed that Gaussian laser irradiated silicon has a central dark smooth region where the temperature is highest followed by particles on the rim and these particles were thought to be laser ablated particles depositing on the surface.

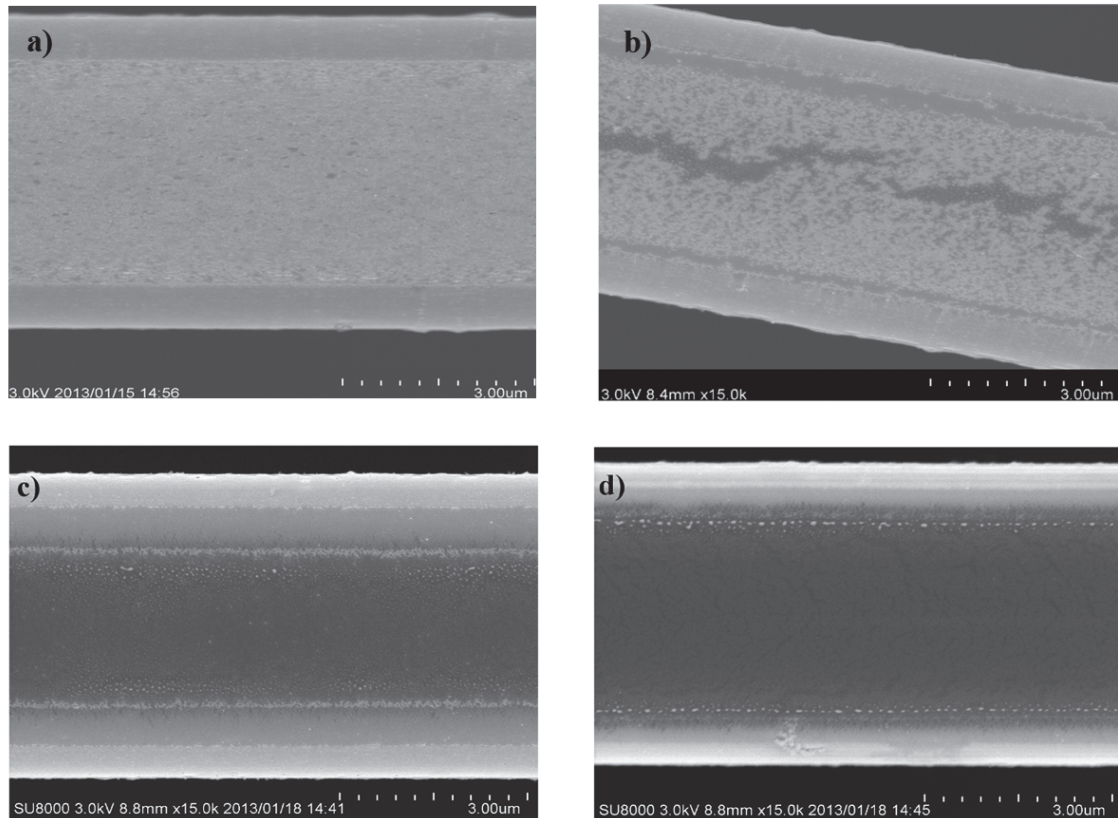


Fig 5.5: Laser treated top surfaces of tensile samples for 10 pulses at a) 2.4 J/cm^2 , b) 2.8 J/cm^2 , c) 3.2 J/cm^2 and d) 4 J/cm^2

5.5 Surface roughness of top surfaces

Figure 5.6 shows the surface morphology for top surfaces of as-fabricated and selected laser treated samples after leveling and curvature adjustment. All laser treated surfaces showed significant curvature compared to the as-fabricated surfaces and were planarized prior to roughness calculations. Figure 5.7 shows different values of average roughness corresponding to different laser energies. Roughness values showed a general decrease with laser energy with the sample irradiated at 3.2 J/cm^2 showing the minimum roughness (2.28 nm) which was an improvement over the as-fabricated sample roughness (2.86 nm). The only exception in roughness value was for the sample irradiated at 2.8 J/cm^2 which showed a significant increase in roughness (13.1

nm). This could be due to particle formation at the midsection as shown in figure 5.5b. The roughness of a particle free area for that value of laser energy is also shown in figure 5.7.

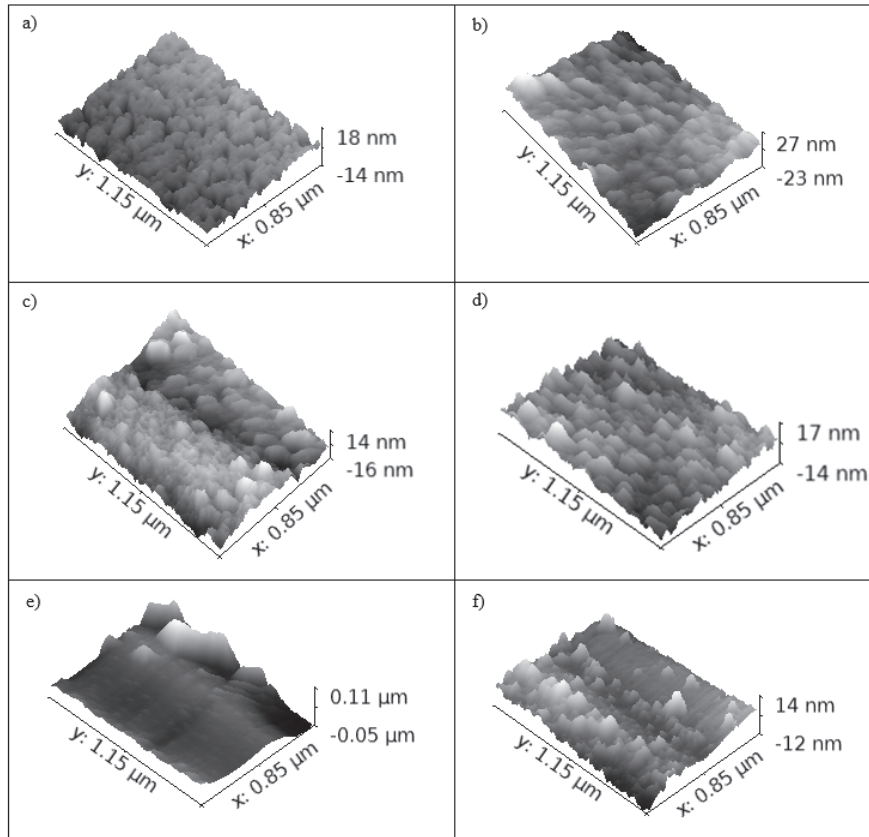


Fig 5.6 Surface profiles for a) as-fabricated and laser annealed samples at b) 1.2 J/cm^2 , c) 1.6 J/cm^2 , d) 2.4 J/cm^2 , and e) 2.8 J/cm^2 and f) 3.2 J/cm^2 with 10 pulses

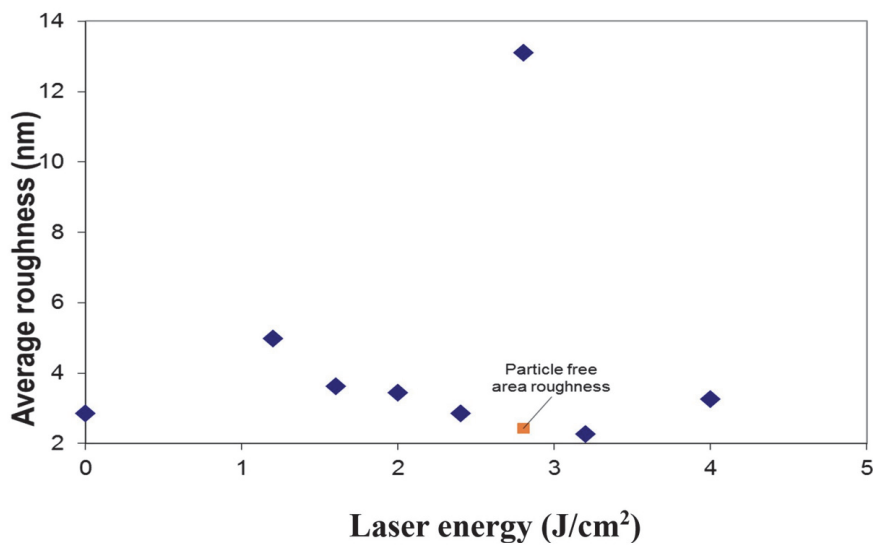


Fig 5.7: Average roughness values for different laser energies with a 10 pulse treatment

5.6 Crystallinity of top surfaces

Figure 5.8 shows the Raman spectra for single crystal silicon for as-fabricated and selected laser treated samples. The most dominant peak for crystalline silicon occurred at 520.7 cm^{-1} for as-fabricated samples. All laser treated samples showed that peak indicating the preservation of a crystalline structure.

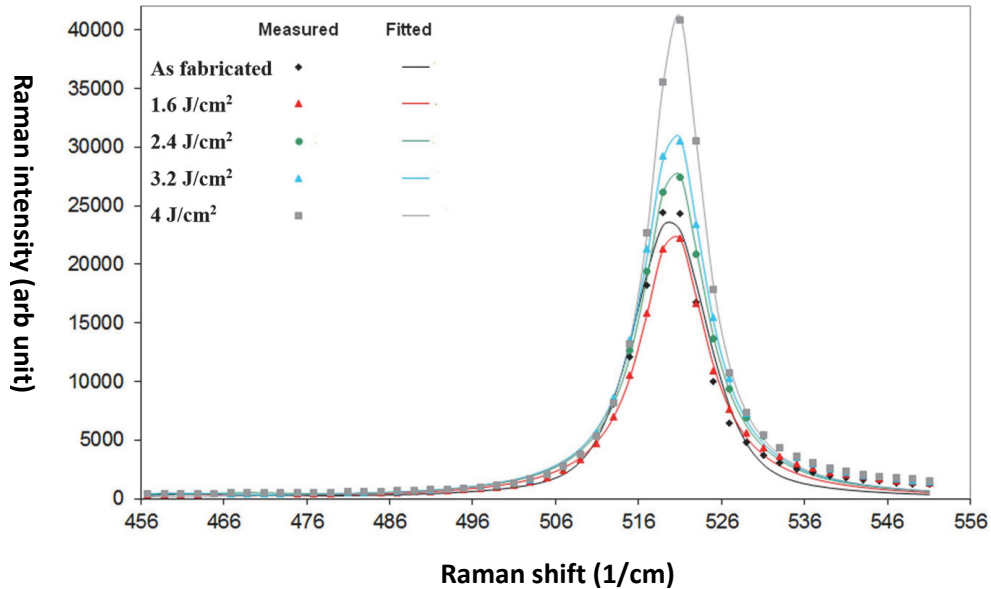


Fig 5.8: Raman spectra for as-fabricated and laser irradiated tensile samples at different laser energies at 10 pulses

It is expected that during the laser treatment of silicon, laser melts the upper top surface while the solid layer beneath acts as a seed layer for the growth of a single crystal [67]. Figure 5.9 shows the resulting data for peak shift and normalized change in peak width with respect to that of the crystal silicon peak of as-fabricated samples. The dominant peak has shifted to the left for all irradiated samples indicating tensile stress development on the surface. The shift showed a general trend of decrease with laser energy especially for energies above 1.2 J/cm^2 at which a maximum shift of 1.14 cm^{-1} was observed corresponding to tensile stresses of about 570 MPa [68]. FWHM remained fluctuating around an average of 0.2 cm^{-1} with a standard deviation of 0.05 cm^{-1} . During the heating cycle, the hot material is trying to expand but is being constrained by the surrounding cool region causing compressive stresses. On solidifying, silicon is trying to contract but is being pulled by the surrounding hot region resulting in tensile stresses as the end result [69].

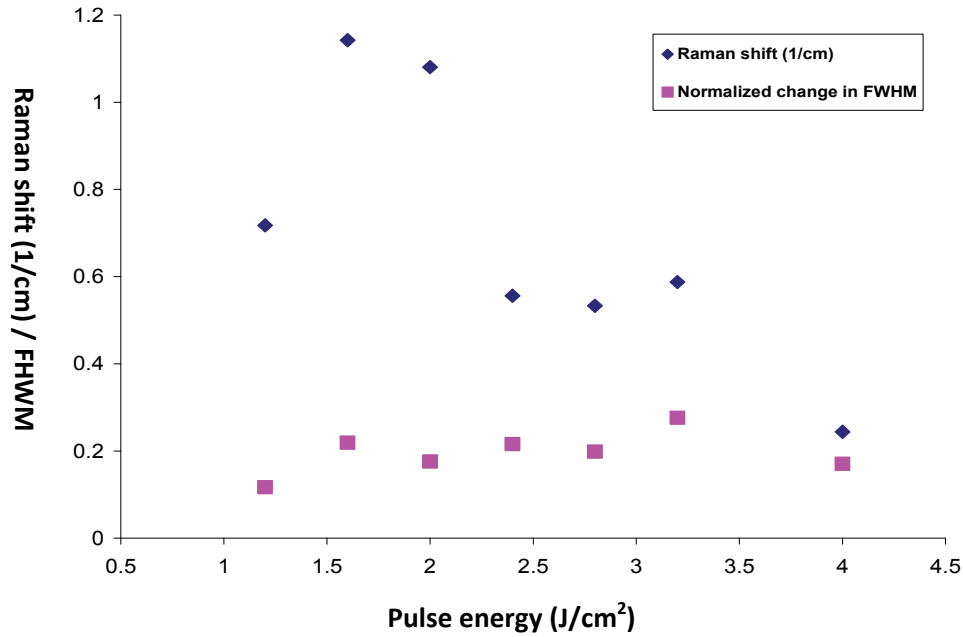


Fig 5.9: Change in normalized FWHM and Raman shift for different laser energies at 10 pulses

5.7 Effect of laser energy, number of pulses on melt flow

Since the melting time is supposed to be within the nanosecond regime and that the time interval between each pulse is 1 second, the effect of the number of pulses is an accumulation in melting time with no heat accumulation or change in the maximum temperature during each pulse. The laser energy on the other hand would be effective to increase the maximum temperature, the melting time, and depth, which decreases viscosity and enhances the flow of the molten silicon. This explains why the laser energy is more significant in liquid flow than the number of pulses as was indicated by the flow of liquid front indicated by the white line on sidewalls as seen in Figure 5.3. This could also explain the more significant change in notch profile of fatigue test samples with laser energy.

Laser energy enhances the flow more significantly than the number of pulses because of the higher maximum temperature, which causes a decrease in viscosity and increase in molten region, but the main contribution of the number of pulses would be to increase the total melting time. So for surfaces that need no precise control on dimensions or profiles, an irradiation with higher laser energy could be efficient for

improving surface roughness but for surfaces requiring preservation of their original shape, multiple shots at lower laser energies might be a better approach.

5.8 Summary of laser treatment conditioning

Trends observed in surface morphologies as functions of the energies and number of pulses are summarized in figure 5.10. From laser irradiation of both fatigue and tensile test samples, common observations can be made regarding ranges of laser energies and associated features together with residual stresses and surface roughness:

- Less than 1.6 J/cm^2 , no improvement in surface roughness is observed. At a high number of pulses (>100), columnar structures develop. Since the ablation threshold is around 1.3 J/cm^2 , such structures are thought to occur due to evaporation and deposition and they increase in length as the number of pulses increases. An increase in residual surface stresses is also observed.
- From 1.6 J/cm^2 to 2.4 J/cm^2 , a good compromise between notch distortion and sidewall roughness was achieved for fatigue test samples. Surface roughness and residual stresses also improve.
- From 2.4 J/cm^2 to 3.2 J/cm^2 , further improvement in surface roughness is observed indicated by scallops disappearing totally from sidewalls and AFM measurements of surface roughness of planar surfaces. The notch radius however increases significantly with laser energy in that range.
- From 3.2 J/cm^2 to 4 J/cm^2 , an improvement in surface roughness compared to as-fabricated samples was achieved. Further improvement in residual surface stresses was also noticed.
- Samples subjected to more than 4 J/cm^2 fractured even for single pulses.

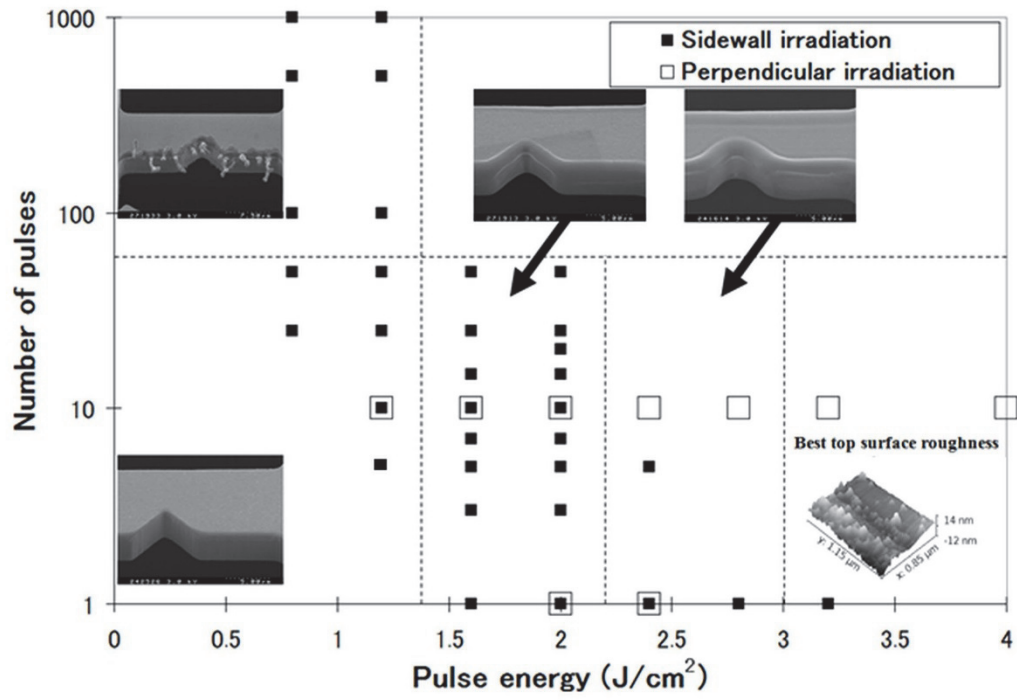


Fig 5.10: Summary of laser treatment results

6. Tensile strength and fracture behavior of laser treated SCS

This chapter focuses on tensile test results of as-fabricated and laser treated samples oriented along $\langle 110 \rangle$ and $\langle 100 \rangle$ directions. Two laser treatment conditions were studied for the $\langle 110 \rangle$ samples and one of them was chosen for both $\langle 110 \rangle$ and $\langle 100 \rangle$ to study the effect of crystal orientation based on the conditioning stage. Fracture strength as well as fracture behavior were investigated for different orientations and laser treatment conditions used in the study.

6.1 Choice of laser treatment condition for tensile test samples

From chapter 5 it was observed that high energies above 2.4 J/cm^2 and until 4 J/cm^2 (fracture energy) could be used for sidewall irradiation of tensile test samples since scallops totally disappear in that range. This range of energy however showed a significant change in notch profile for notched samples subjected to irradiation as shown in figure 5.3 I and j. The high energies could cause a significant change in cross section shape of tensile test samples. We decided to investigate two conditions for laser irradiation. The first condition aims at sidewall roughness improvement only using a 65° tilt angle at a low energy (1.2 J/cm^2) for 5 pulses to preserve cross section shape. The second condition on the other hand was at high energy (4 J/cm^2) aiming at total removal of scallops from sidewalls as well as improving surface roughness of top surface by using a tilt angle of 45° and 10 pulses. Both conditions were investigated on $\langle 110 \rangle$ samples and tensile strength results as well as fracture behavior were compared. Finally, $\langle 100 \rangle$ samples were irradiated using the laser treatment condition that achieved the highest improvement in fracture strength results. Five to eight samples were investigated for each condition.

6.2: Temperature distribution analysis

Figure 6.1 shows a 2D FEM temperature distribution analysis by a single pulse treatment of laser at 4 J/cm^2 tilted by 45° and at 1.2 J/cm^2 tilted by 65° .

The temperature gradient existed for both cases where the maximum temperature occurred at the top corner and decreased along both sidewalls and top surface. The temperature distribution on the sidewall for the 65° tilting was more uniform than that for the 45° tilting where a large temperature difference existed along sidewalls

between top corner and bottom corner. It is also observed that the temperature reached on sidewalls is higher than the temperature reached on the top surface for the 65° tilt angle case. This means that such an angle causes the laser treatment to occur mainly at sidewalls rather than the top surface.

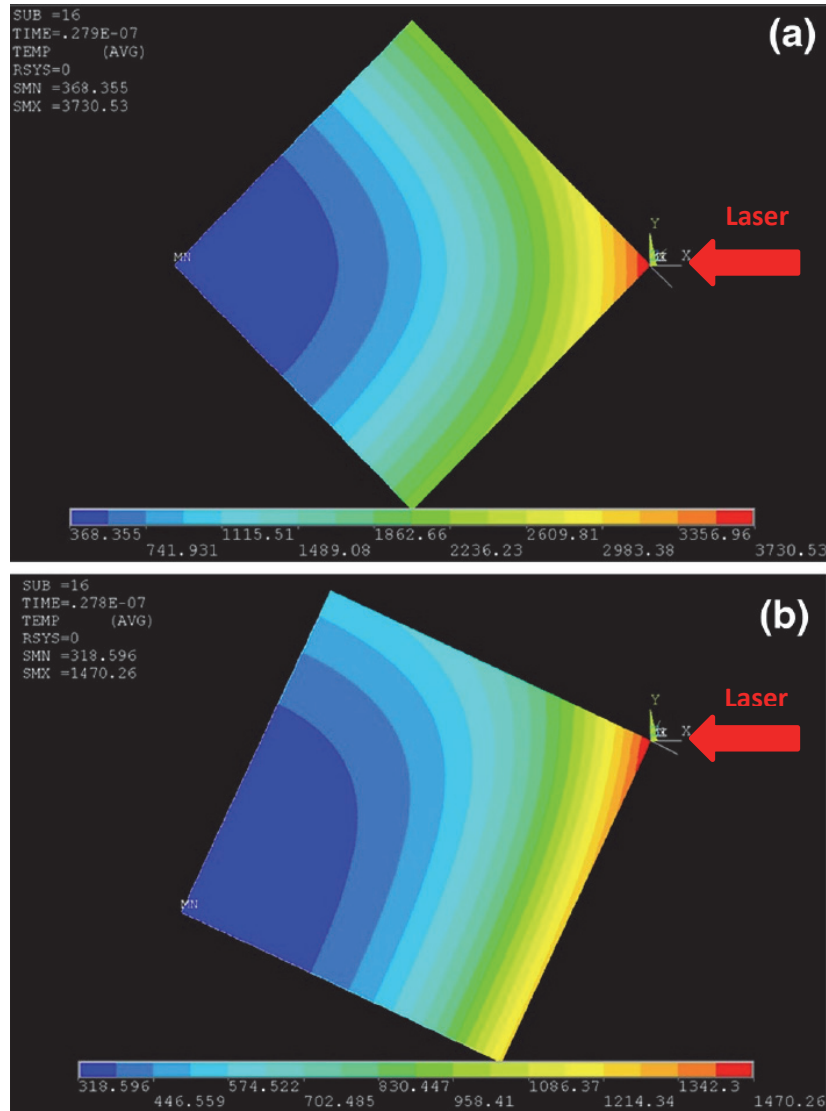


Fig 6.1: Temperature distribution for laser treated samples at a) 4 J/cm² tilted by 45° and b) 1.2 J/cm² tilted by 65°

6.3 Tensile strength of as-fabricated and laser treated samples

Figure 6.2 shows the tensile strength with indicating the fracture location for as-fabricated and laser treated <110> samples with two different laser treatment conditions. The as-fabricated samples had the average tensile strength of 3.20 GPa with the standard deviation of 0.28 GPa. Samples irradiated at 45° showed the average strength of 3.84 GPa with the standard deviation of 0.58 GPa. Samples that were

irradiated at 65° showed the average strength of 3.16 GPa with the standard deviation of 0.40 GPa. Figure 6.3 shows the fracture surfaces and corresponding side views of as-fabricated as well as laser irradiated samples at different conditions with the fracture origins encircled. The as-fabricated samples had scallops on the sidewalls with a slightly etched top surface and accordingly seven out of eight samples fractured at the sidewalls near the top. Such behavior could be due to the upper section of the sidewall being subjected to more etch cycles causing degradation and accumulation of roughness [49, 70].

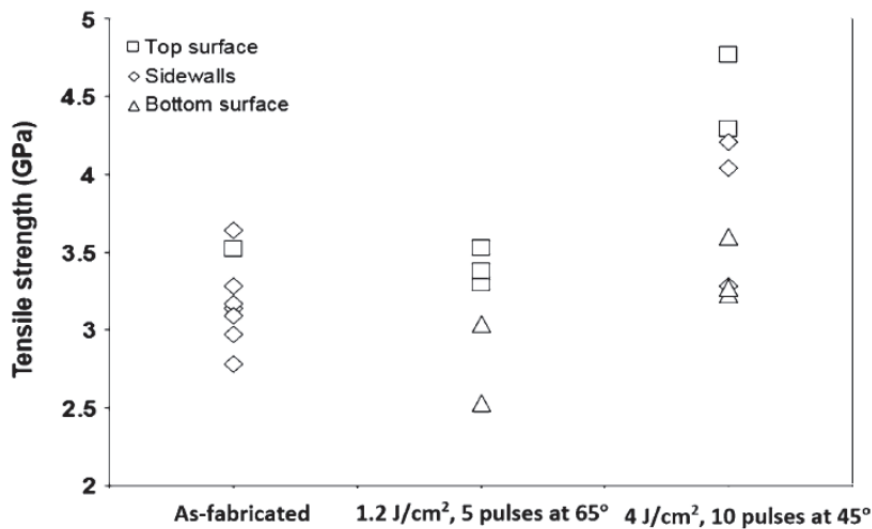


Fig 6.2: Fracture strength and location for as-fabricated and laser treated $\langle 110 \rangle$ samples

The cross section of the laser treated samples at 65° shows a nearly square shape with the distortion occurring mainly at the top corners being subjected to the highest temperature as seen from figure 6.3. Sidewalls also show the removal of scallops indicating the occurrence of melting. The simulation result however shows that the maximum temperature (1470 K) is lower than the melting point (1689 K) as can be seen from figure 6.1. This might be related to the simulation assumption of smooth sidewalls as mentioned previously in section 5.2. None of the samples fractured at sidewalls; two samples fractured at the bottom surface while three fractured at the top surface. The samples that fractured at the top surface after laser treatment at 65° showed the highest strength and had the fracture starting at the midsection as seen in figure 6.3. Such behavior can be related to temperature distribution results where fracture starts at the location experiencing the lowest temperature as can be seen from the simulation results in figure 6.1.

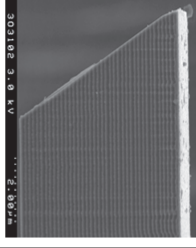
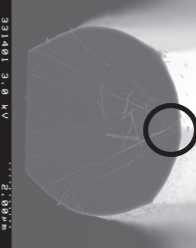
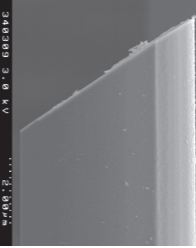
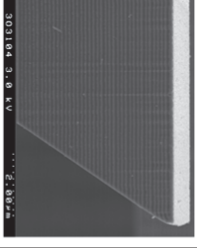
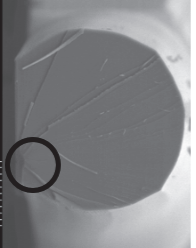
	As fabricated	1.2 J/cm ² , 5 pulses @65°	4 J/cm ² , 10 pulses @45°
Top surface	 	 	 
Sidewall	 		 
Bottom surface		 	 

Fig 6.3: Fracture surfaces and sidewalls for as-fabricated and laser treated $\langle 110 \rangle$ samples. Fracture origin location is encircled

The samples fractured at the bottom surface showed the lowest strength. With FESEM observation these samples had the etch pits on the bottom surfaces as can be seen in 6.4. The etch pits become locations of stress concentration that cause such a lower strength. They could be a result of wet etching of the oxide layer while releasing the test structures.

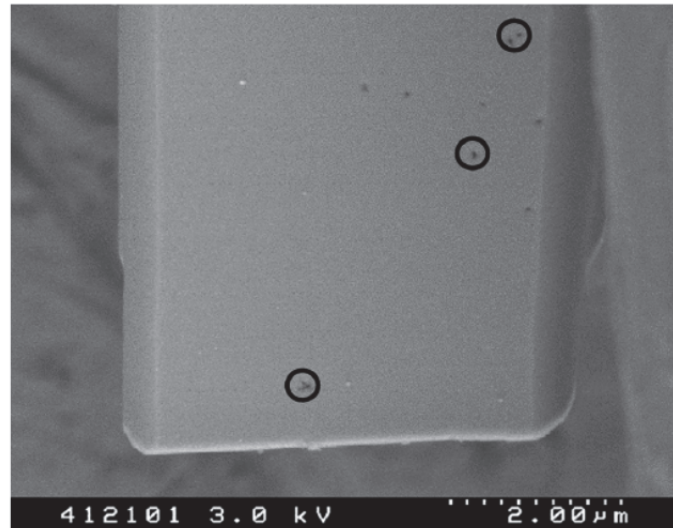


Fig 6.4: Bottom surfaces of laser treated $\langle 110 \rangle$ samples at 1.2 J/cm^2 , 5 pulses tilted at 65° with several etch pits encircled

For laser treated samples at 45° , a significant change in cross section due to laser irradiation was observed as can be seen in figure 6.3. Sidewalls as well as top surfaces exhibit significant curvature change while bottom surfaces remains flat since it was not subjected to laser irradiation. Side views of samples show that scallops have almost disappeared. Fracture origin location after irradiation is more evenly distributed among all surfaces unlike samples irradiated at 65° . Three samples fractured at sidewalls, three at bottom surfaces and two at top surfaces. There also seems to be a trend between fracture origin location and strength. Samples that fractured at top surface showed the highest strength followed by samples that had sidewall fracture origins and finally samples that fractured at bottom surfaces. An investigation was made to explain the relation between fracture origin location and tensile strength. Samples that fractured at bottom surfaces showed that they had etch pits prior to tensile testing as can be seen in figure 6.5 and showed the lowest strength as was observed with samples irradiated at 65° . Samples that fractured at sidewalls had intermediate strength values. Bottom surfaces were free of any etch pits. These samples had fracture origins on the

lower parts of sidewalls as shown in figure 6.3. Figure 6.6 shows a bottom view of that sample in figure 6.3 and it can be observed that the lower parts have higher roughness than the rest of the sidewall. This could also be attributed to these parts being subjected to the lowest temperatures compared to the rest of the neighboring areas of the sidewalls as can be seen in figure 6.1.

Samples that fractured at top surfaces had the highest strength. Fracture started at the midsection of the top surface as can be seen in 6.3. Figure 6.7 shows a top surface view for that sample in figure 6.3 and it can be observed that the midsection has higher roughness than the neighboring area also being subjected to a lower temperature than the rest of the top surface. Particles can also be observed depositing in the midsection which might be a result of ablation and deposition.

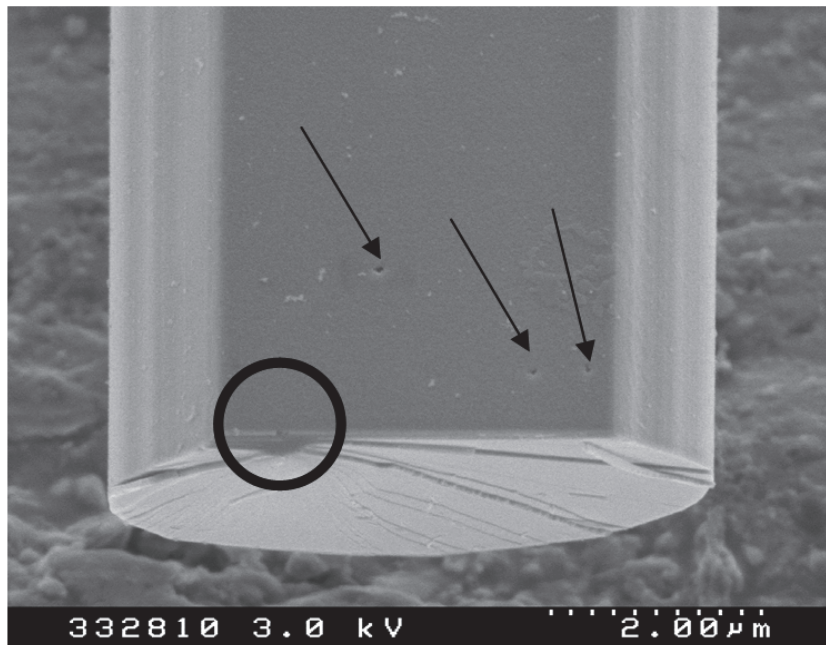


Fig. 6.5: Bottom surface of a laser treated samples at 4 J/cm^2 that fractured at the bottom surface. A circle indicates the fracture origin and arrows indicate etch pits.

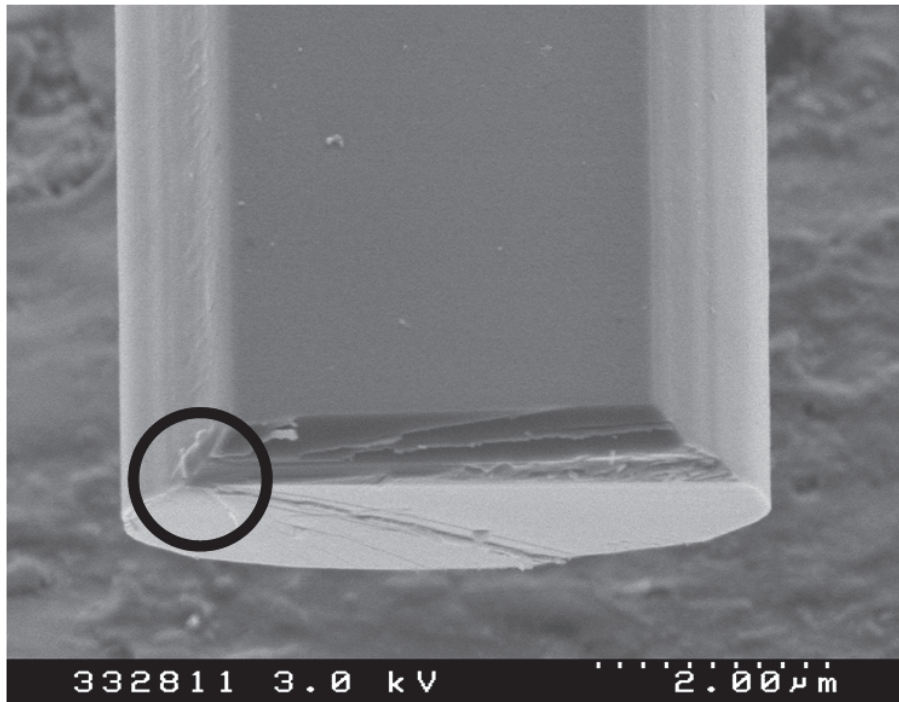


Fig. 6.6: Bottom view of a laser treated sample at 4 J/cm^2 that fractured at sidewalls. A circle indicates the fracture origin.

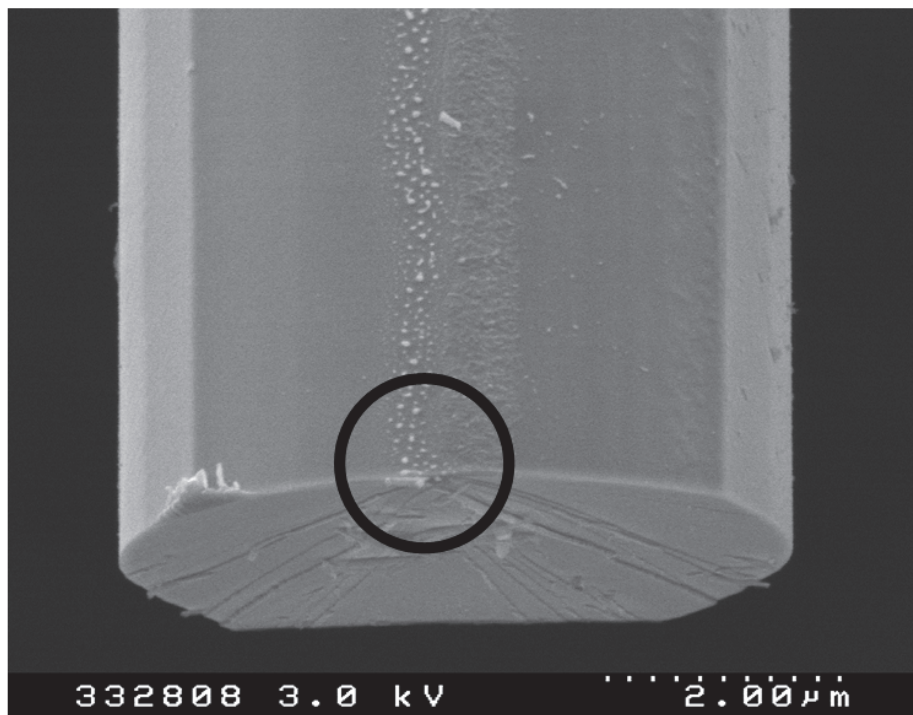


Fig 6.7: Top surface view of a laser treated sample that fractured at top surface. A circle indicates the fracture origin.

Samples fractured on the top surface had higher average strength compared to samples fractured at sidewalls. This means that those samples had smoother sidewalls compared to the rest of the laser treated samples. This might be related to the initial surface roughness of these samples.

For a fair comparison of fracture strength results for both laser treatment conditions, results of samples that have etch pits on the bottom surfaces will not be taken into account since etch pits are generated randomly and may hinder the effect of treatment. All results of the samples which had the fracture origins at the bottom surfaces are not considered leading to an average tensile strength of 3.40 GPa (6% improvement) for samples irradiated at 65° and an average strength of 4.12 GPa (30% improvement) for samples irradiated at 45°. The slight improvement for the samples irradiated at 65° could be caused by the top surface roughness since the treatment resulted in mainly roughness improvement of sidewalls only. Samples irradiated at 45° had both top surface and sidewalls irradiated using a higher energy and much higher strength was achieved. Both conditions however proved the effectiveness of laser treatment as a method for improving tensile strength by improving surface roughness of sidewalls as well as top surfaces.

6.4 Effect of crystallographic orientation

Samples oriented along the <100> direction were irradiated at 45° with ten laser pulses at 4 J/cm² and compared with <110> samples irradiated with the same irradiation condition which showed the highest improvement in strength. We did not observe any difference in the surface roughness and cross-sectional shape of these two directions samples after the irradiation. For a comparison of the effect of laser irradiation on the strength, the result of one as-fabricated <100> sample (2.4 GPa) fractured from the bottom surface was not included. Figure 6.8 shows the tensile strengths of as-fabricated and laser treated <100> samples with the location of fracture origin indicated. Both the samples oriented along the <110> and <100> directions showed nearly the same improvement in tensile strength (30%). The as-fabricated <100> samples had the average strength of 3.00 GPa with the standard deviation of 0.30 GPa and that of the irradiated samples is 3.90 GPa with the standard deviation of 0.66 GPa.

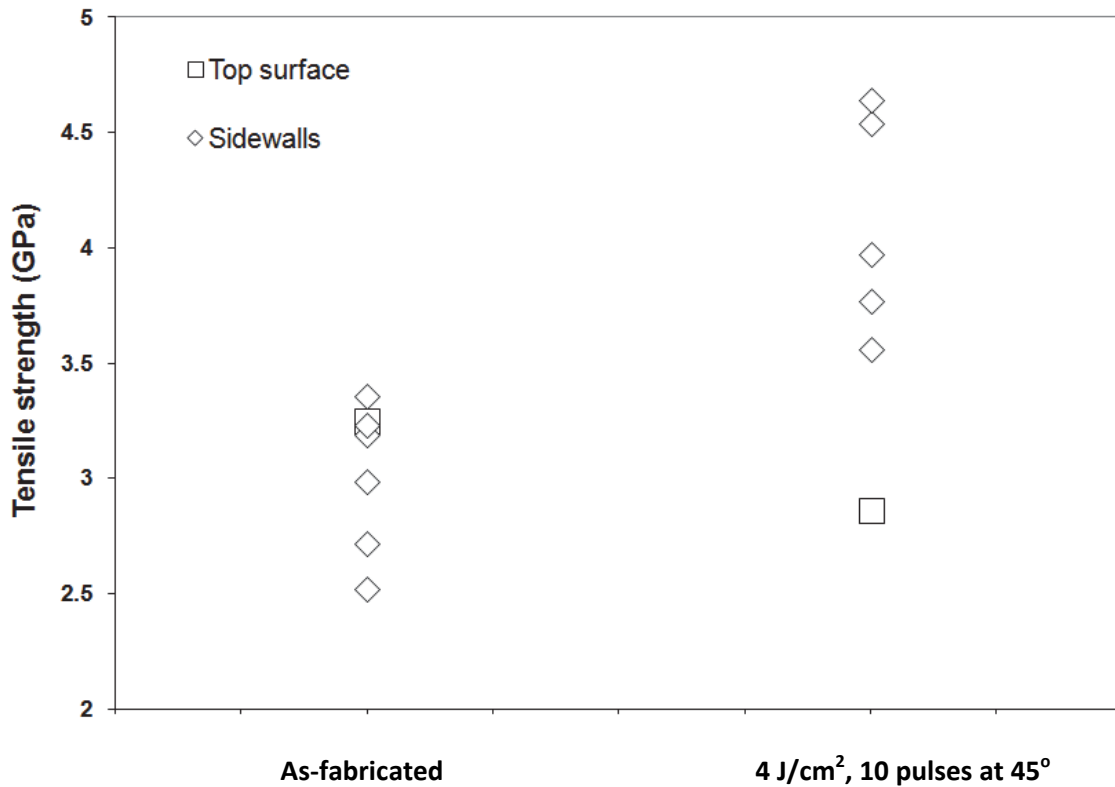


Fig 6.8: Fracture strength and location for as-fabricated and laser treated $\langle 100 \rangle$ samples

Figure 6.9 shows the fracture surfaces and side views of $\langle 100 \rangle$ oriented samples with the fracture origins encircled. Almost all of the as-fabricated $\langle 100 \rangle$ samples fractured near the top corner of the sidewalls, while the sidewall fracture origin shifted towards the bottom after laser irradiation as was observed with the $\langle 110 \rangle$ samples due to the bottom corners exhibiting the lowest temperature during laser treatment. The $\langle 110 \rangle$ samples also showed the average fracture strain, calculated using the theoretical Young's modulus, that is about 20% lower than the $\langle 100 \rangle$ samples. Such behaviour has been reported earlier by Ando et al. [46] who observed that fracture strains of samples tested either in bending or uniaxial tensile tests showed a lower strain for $\langle 110 \rangle$ samples than for $\langle 100 \rangle$ samples.

Both $\langle 110 \rangle$ and $\langle 100 \rangle$ oriented samples showed 30% improvement in the tensile strength at the same treatment condition through improvement of the roughness of the surface where fracture occurred which indicates that the crystal orientation does not affect the increase in the tensile strength due to surface roughness improvement. The strength values achieved in the current study are comparable to those from the work done by Shikida et al. [24] who have achieved a maximum strength value of 4.2 GPa through roughness improvement using KOH wet etching with the scallops totally removed.

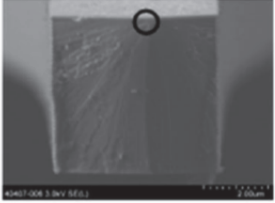
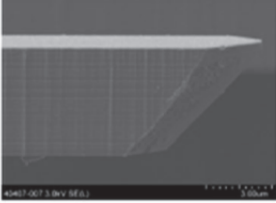
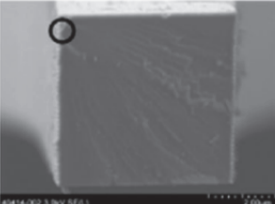
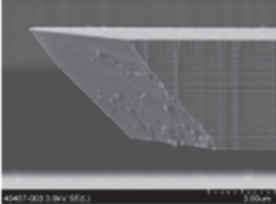
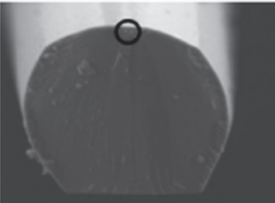
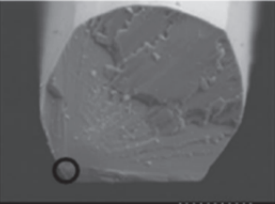
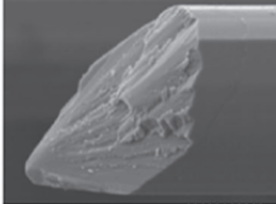
Fracture Origin		Fracture surface	Sidewall
As-fabricated	Top surface		
	Sidewall		
Laser-treated	Top surface		
	Sidewall		

Fig 6.9: Fracture surfaces and sidewalls for as-fabricated and laser treated <100> samples with fracture locations encircled

6.5 Fracture behavior of as-fabricated and laser treated samples

As-fabricated as well as laser treated samples for both $\langle 110 \rangle$ and $\langle 100 \rangle$ samples had (111) cleavage planes. It is the plane having the lowest surface energy [48]. Fracture behavior for $\langle 110 \rangle$ and $\langle 100 \rangle$ samples however was different. The samples oriented along $\langle 110 \rangle$ direction showed smooth surfaces and fractured on the (111) plane. Most of the samples oriented along the $\langle 100 \rangle$ direction showed rough fracture surfaces and clear cleavage steps especially after laser treatment as can be seen from figures 6.9 and 6.10. Figure 6.11 shows 3D schematics of as-fabricated and laser treated $\langle 100 \rangle$ fracture surfaces for the top and sidewall origins colored in red and fracture origins encircled. The rough features for $\langle 100 \rangle$ fracture surfaces and cleavage steps are a sign of directional instability and are usually associated with mixed fracture modes where shear loading is substantial [71]. Substantial shear loading might be due to the larger angle (54.7°) between the (100) loading plane and the (111) cleavage plane as opposed to a small angle between the (110) loading plane and the (111) cleavage plane (35°). Since the rough features were more significant after laser treatment, this might be related to the fracture strength that has increased by 30% after laser treatment.



Fig 6.10: Top view of a laser treated $\langle 100 \rangle$ sample after fracture showing cleavage steps

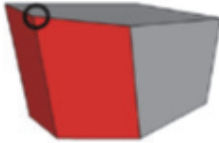
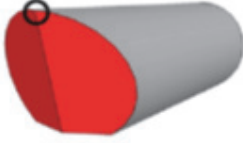
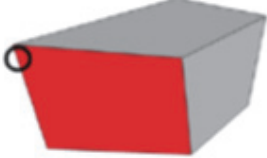
Fracture origin	As-fabricated	Laser-treated
Top surface		
Sidewall		

Fig 6.11: 3D schematic of as-fabricated and laser treated $\langle 100 \rangle$ samples after fracture with fracture location encircled

6.6 Concluding remarks

Laser treatment results in a significant improvement in fracture strength regardless of samples orientation. A high energy (4 J/m^2) low tilt angle (45°) laser treatment condition showed a 30% improvement in fracture strength for both $\langle 110 \rangle$ and $\langle 100 \rangle$ specimens due to roughness improvement of both top surfaces and sidewalls. A significant change in cross section was observed. The cross section of laser treated samples was preserved using the low energy (1.2 J/cm^2) high tilt angle (65°) treatment condition however a slight improvement in tensile strength was achieved. Both as-fabricated and laser treated $\langle 110 \rangle$ and $\langle 100 \rangle$ orientations had cleavage to occur on the (111) plane with the $\langle 100 \rangle$ samples showing rough surfaces and cleavage steps especially after laser treatment. This can be related to the angle of the (100) loading plane with respect to the (111) fracture plane.

7. Fatigue properties of laser treated SCS

This chapter focuses on test results of as-fabricated and laser treated fatigue samples. It starts first by studying a laser treatment condition based on the conditioning stage performed on the fatigue sample with the wide notch type. Fatigue experiments on the wide notch samples influenced our strategy to change the type of notch to narrow notch, condition for laser treatment and fatigue testing conditions. Fatigue life as well as fracture behavior for as-fabricated and laser treated samples have been investigated.

7.1 Laser treatment of wide notch samples

From the experiments performed during the conditioning stage on the wide notch samples, energies in the range of 1.6 J/cm^2 and 2.4 J/cm^2 would be most suitable for fatigue testing since there is a compromise between improvement in sidewall roughness and preservation the notch profile. Notch profile preservation is important since it determines the level of stress concentration and makes the comparison between as-fabricated and laser treated samples valid. The condition of a single pulse at 1.6 J/cm^2 at an angle of 65° was used. Samples were oriented along the $\langle 100 \rangle$ direction. The lowest energy in the energy range was chosen to minimize the change in notch profile while allowing for an improvement in sidewall roughness. Figure 7.1 shows the surface morphology for a typical sample after laser treatment. There are ridges at the notch tip near the top surface, which was also observed in figure 5.3.

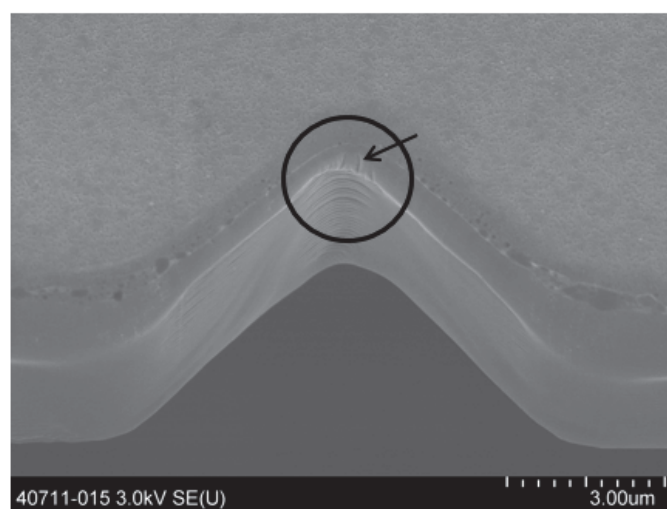


Fig 7.1: Notch part of fatigue sample after laser treatment at 1.6 J/cm^2 for 1 pulse at 65° , ridges are encircled

7.2: Fatigue testing of wide notch samples

Six as-fabricated samples were tested with a constant deflection amplitude of 2.25° . The fatigue life is shown in table 7.1. Fatigue life ranged from 7.0×10^8 to 6.3×10^9 cycles with the average of 2.4×10^9 . FESEM images of the fracture surfaces of selected samples are shown in figure 7.2.

Table 7.1: Fatigue life of as-fabricated wide notch samples

Sample ID	Fatigue life ($\times 10^9$)
1	6.3
2	3.3
3	1.9
4	1.1
5	1.1
6	0.7

Fracture of the laser treated samples occurred while the load was being increased prior to reaching the constant amplitude (2.25°). The sample shown in figure 7.1 fractured at the amplitude of 1.6° with the fracture surface shown in figure 7.3. The ridges at the notch tip would be the source of stress concentration that leads to premature failure of the laser treated structures.

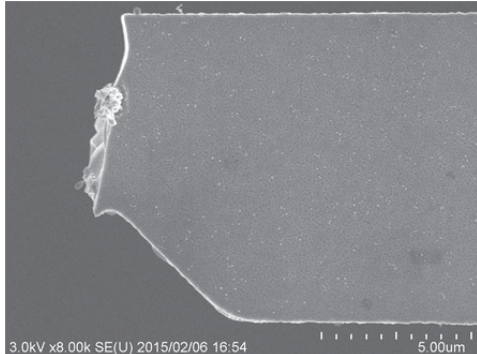
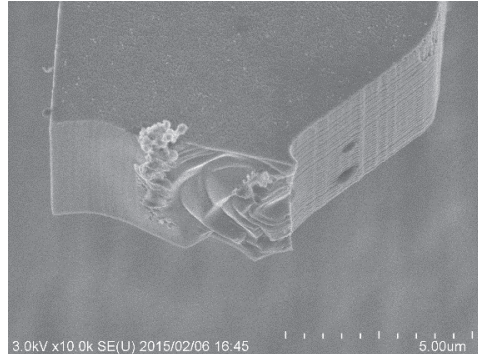
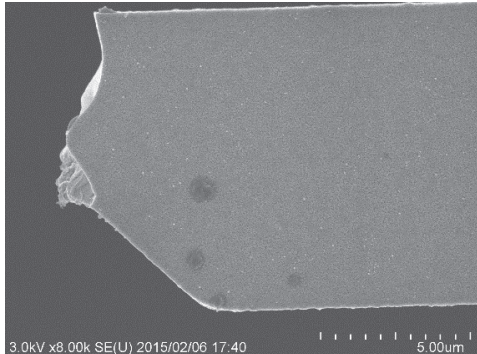
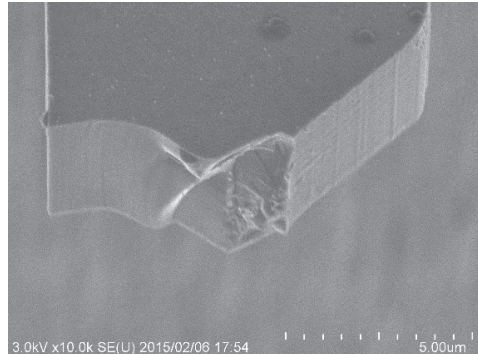
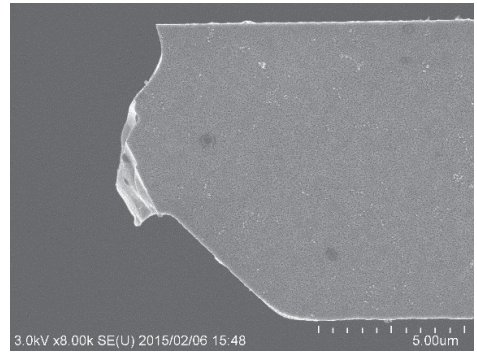
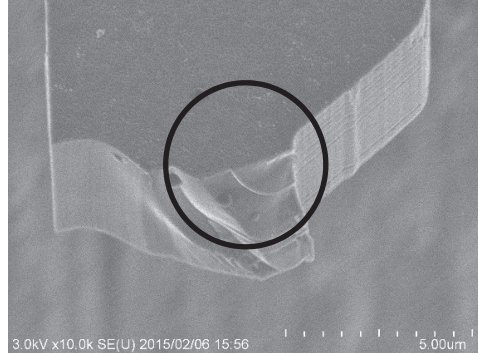
Sample ID	Top view	Fracture surface
1		
2		
4		

Fig 7.2: Fracture surfaces for selected fatigue samples

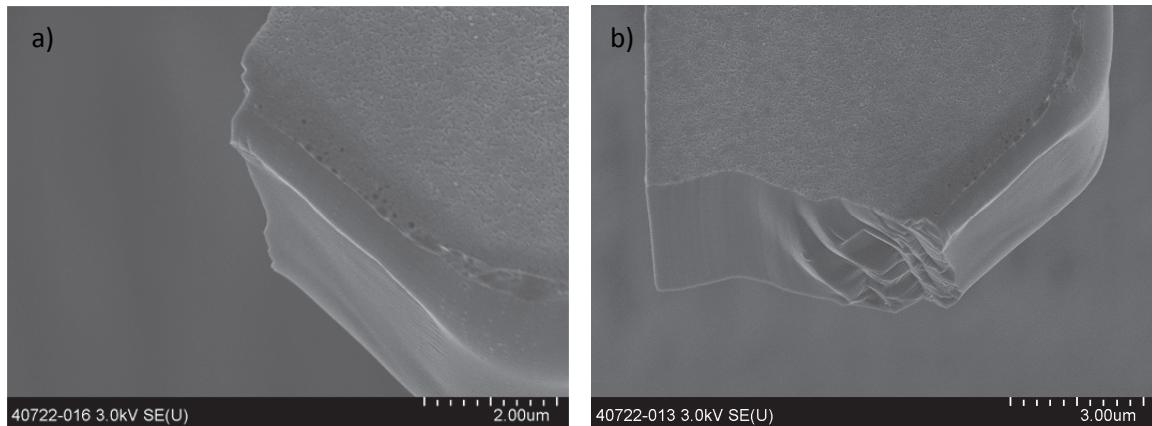


Fig 7.3: Sample in figure 7.1 after fracture at 1.6° a) Notch surface and b) fracture surface

7.3 Fracture behavior of wide notch samples

For as-fabricated samples in figure 7.2, looking at the fracture surface of sample 4 it seems that the crack initiated near the top corner as can be seen from the concentric lines that are encircled in the figure. This agrees well with results from as-fabricated tensile test samples where fracture also initiated near the top corner and can be attributed to the surface roughness as was explained in section 6.2. Other features observed on most fracture surfaces include steps that are observed in the vicinity of the notch area followed by a smooth region. No clear major cleavage plane was observed from top view images as the crack seems to have a zigzag shape across the sample width. Similar crack path was observed by Ikehara [12] for samples of same size and orientation but having a different notch type. Another feature to note is that cracks did not initiate at the notch tip as can be seen from top view images of samples 1 and 2. For most samples, cracks seemed to initiate at locations that are slightly displaced from the notch tip. This could be attributed to stress distribution since the first principal stress was found not to occur at the notch tip but is displaced by an angle of about 30° based on stress analysis done by Ikehara [12].

As for laser treated samples, from figure 7.1 the ridges would be the source of stress concentration and premature failure. These ridges only disappear at energies higher than 2.4 J/cm^2 as can be seen from figure 5.3. High energy leads to a significant change in notch profile and alters the stress level at the notch, which makes the comparison against as-fabricated samples invalid.

7.4 Choice of laser treatment condition for narrow notch samples

We decided to test narrow notch type samples, shown in figure 7.4, since a narrower notch would lead to a more localized irradiation and less distortion in the notch profile will result. A low laser energy condition to insure preserving the notch profile was used.

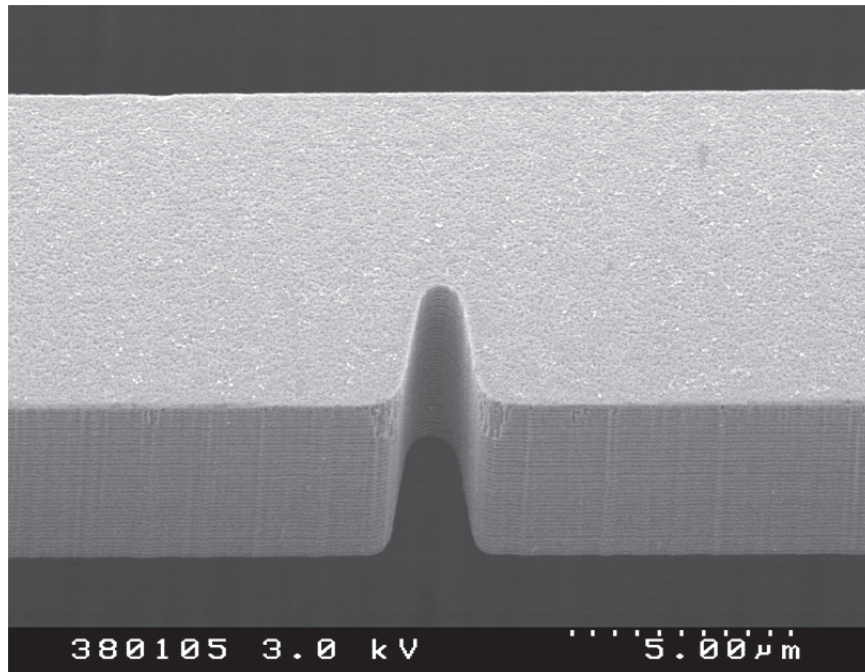


Fig 7.4: Narrow notch test structure.

The optimized laser treatment condition was 1 J/cm^2 , 5 pulses at 45° . This condition was chosen based on a conditioning stage for narrow notch sample and it was found to achieve a good compromise between roughness improvement and notch profile preservation. Higher energies lead to protrusions acting as locations of stress concentration at the notch tip as shown in figure 7.5 for a sample irradiated at 1.4 J/cm^2 , 2 pulses. Lower energies showed no significant improvement in roughness. This also agrees with results from the conditioning stage of wide notch samples where stress concentration features at the notch tip start to occur at energies higher than 1.2 J/cm^2 . Samples oriented along the $\langle 110 \rangle$ direction were considered for fatigue testing instead of $\langle 100 \rangle$ samples, because of the stress analysis by Ikehara et al [12] who showed that the highest stress is at the notch tip for $\langle 110 \rangle$ samples. The stress in $\langle 100 \rangle$ samples is more distributed over the notch tip area. The localised notch tip laser

treatment would be more effective in the case of $\langle 110 \rangle$ oriented samples. The notch radius as can be seen from figure 7.6 was preserved.

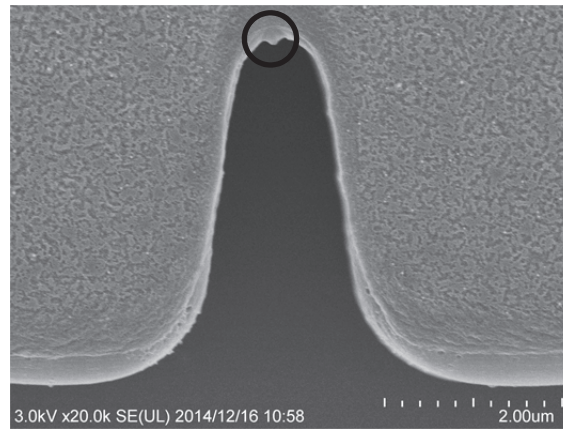


Fig 7.5: Top view at notch area of a sample irradiated at 1.4 J/cm^2 , 2 pulses tilted at 65° with the protrusion encircled

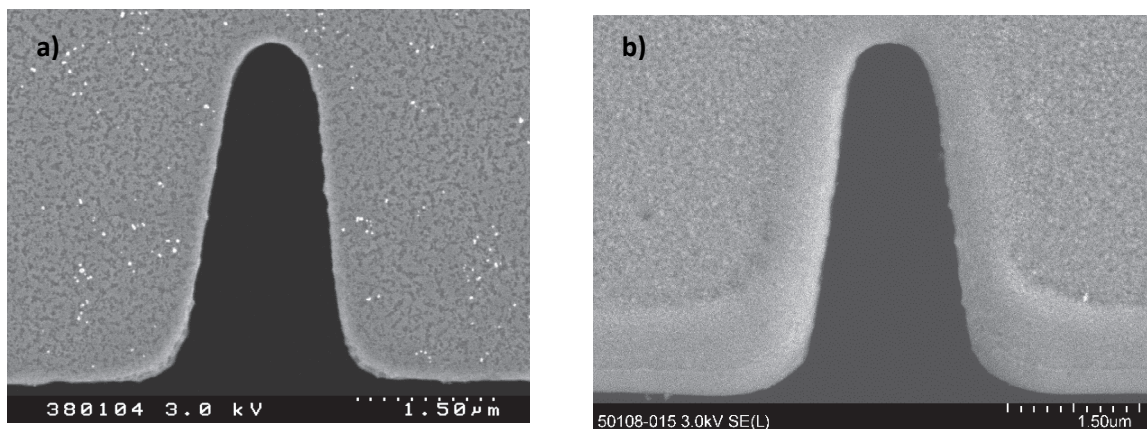


Fig 7.6: Narrow notch top view of a) as-fabricated sample and b) laser treated samples

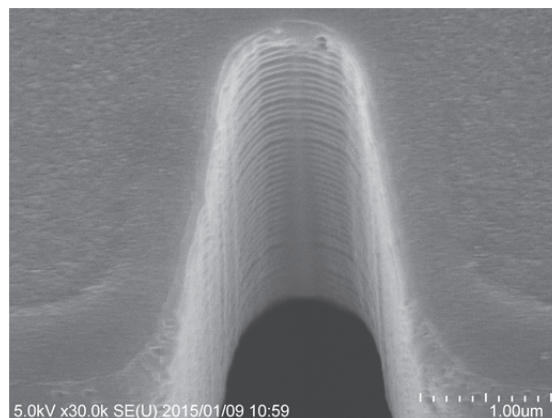


Fig 7.7: Notch area after laser treatment

As can be seen from figure 7.7 slight improvement in surface roughness near the notch tip was achieved where scallops disappear.

7.5: Fatigue testing of narrow notch samples

As-fabricated samples were tested first. The deflection amplitude was kept constant at 1.7° which is lower than the amplitude used for the wide notch fatigue samples since $\langle 110 \rangle$ samples are known to fracture at a lower amplitude than $\langle 100 \rangle$ samples [10,12]. This deflection amplitude corresponds to the same nominal stress value caused by a deflection of 2.25° of $\langle 100 \rangle$ samples. The fatigue life of as-fabricated $\langle 110 \rangle$ narrow notch samples are shown in table 7.2 while FESEM images for selected fractured samples are shown in figure 7.8. The number of cycles until fracture of seven as-fabricated samples ranged from 8.3×10^7 to 1.3×10^9 cycles with an average of 5.6×10^8 .

Table 7.2: Fatigue life of as-fabricated narrow notch samples

Sample ID	Fatigue life ($\times 10^9$)
1	1.3
2	1.1
3	0.71
4	0.45
5	0.19
6	0.13
7	0.083

The fatigue life of laser treated sample are shown in table 7.3 with the corresponding FESEM images of selected fractured samples shown in figure 7.9. Laser treated samples showed a wide variation in Fatigue life. Two samples fractured instantaneously, one sample showed a fatigue life of 1.1×10^7 cycles and two samples showed an improvement (1.8×10^9 cycles).

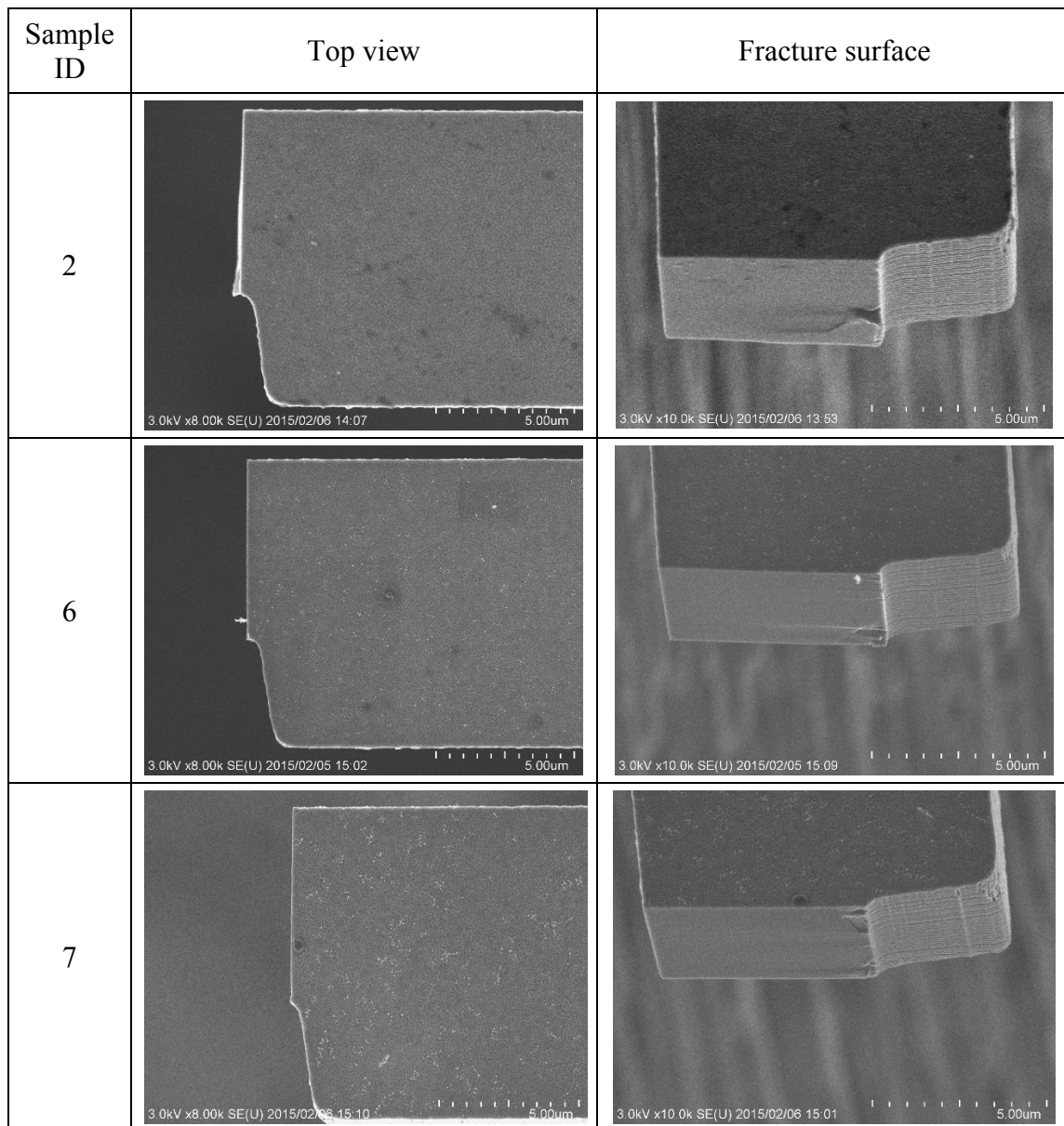


Fig 7.8: Fracture surfaces for as-fabricated narrow notch $\langle 110 \rangle$ samples

Table 7.3: Fatigue life of laser treated samples with a narrow notch

Sample ID	Fatigue life ($\times 10^9$)
1	1.8
2	1.8
3	0.011
4	Instant fracture
5	Instant fracture

7.6 Fracture behavior of narrow notch samples

The fracture behaviour of as-fabricated and laser treated samples showed the main cleavage plane being the (110) plane leaving smooth fracture surfaces as can be seen from figures 7.8 and 7.9.

For as-fabricated samples, results agree well with studies previously conducted by Ikehara et al [12] about fracture behaviour of similar samples. From top views in figure 7.8, most samples had the cracks to initiate almost at the notch tip. This is attributed to the maximum first principle stress at the notch tip. Sample 7 of the shortest fatigue life fractured at an offset position from the notch tip and we think that a stress concentration feature at that location might have led to a shorter fatigue life.

As for laser treated samples, looking at the top view images in figure 7.9, the relation between fracture origin and fatigue life was opposite to as-fabricated samples. In the laser treated samples, the two samples that showed an improvement in fatigue life had the fracture origin at an offset position from the notch tip. The three samples that showed shorter fatigue life or instant fracture had the crack fracture origin at the notch tip.

For the two samples with improved fatigue life, the laser treatment was successful in improving surface roughness at the notch center and the crack initiation location shifted from the notch tip to an offset position. This proves the effectiveness of even low energy localized laser treatment in improving fatigue performance of SCS silicon structures.

From the close up image of sample 3 in figure 7.10 we see no effect of laser treatment in improving scallops at the notch area. We conclude that the sample was in an “as-fabricated” condition in terms of roughness at notch area and showed a fatigue life that was comparable to as-fabricated samples.

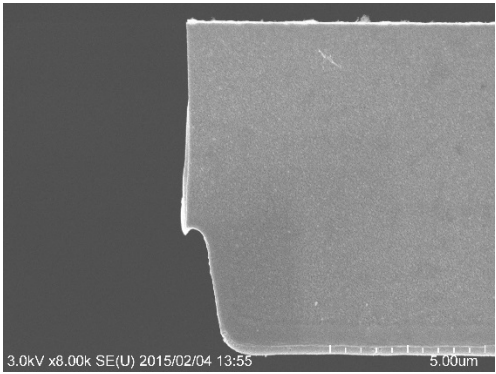
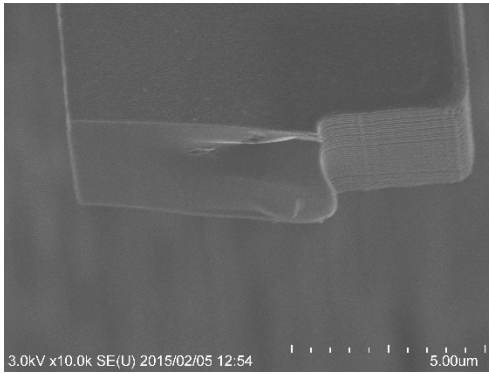
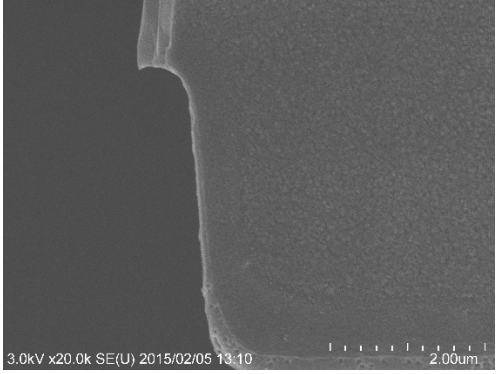
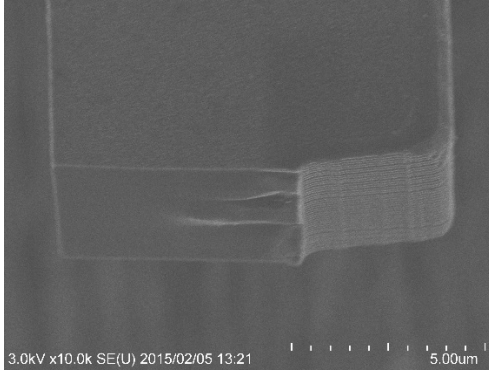
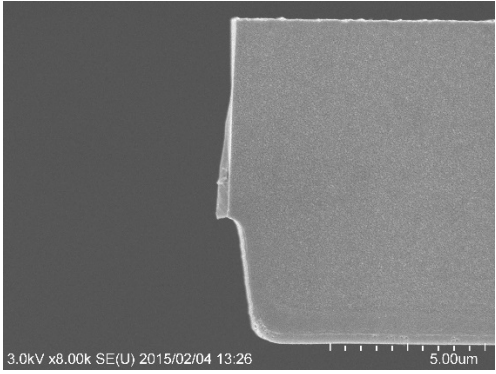
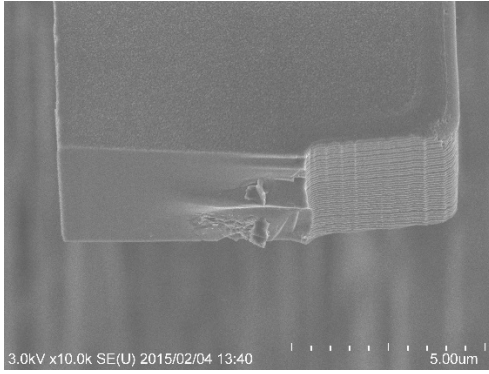
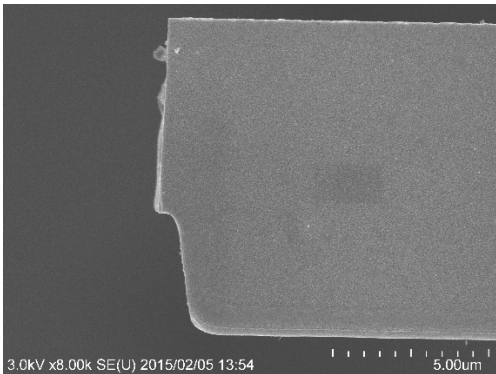
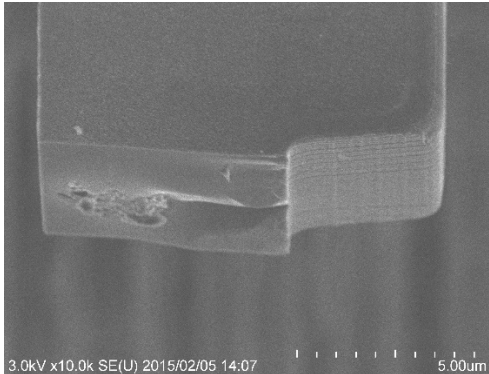
Sample ID	Top view	Fracture surface
1	 <p>3.0kV x8.00k SE(U) 2015/02/04 13:55 5.00um</p>	 <p>3.0kV x10.0k SE(U) 2015/02/05 12:54 5.00um</p>
2	 <p>3.0kV x20.0k SE(U) 2015/02/05 13:10 2.00um</p>	 <p>3.0kV x10.0k SE(U) 2015/02/05 13:21 5.00um</p>
3	 <p>3.0kV x8.00k SE(U) 2015/02/04 13:26 5.00um</p>	 <p>3.0kV x10.0k SE(U) 2015/02/04 13:40 5.00um</p>
5	 <p>3.0kV x8.00k SE(U) 2015/02/05 13:54 5.00um</p>	 <p>3.0kV x10.0k SE(U) 2015/02/05 14:07 5.00um</p>

Fig 7.9: Fracture surfaces for laser treated narrow notch $\langle 110 \rangle$ samples

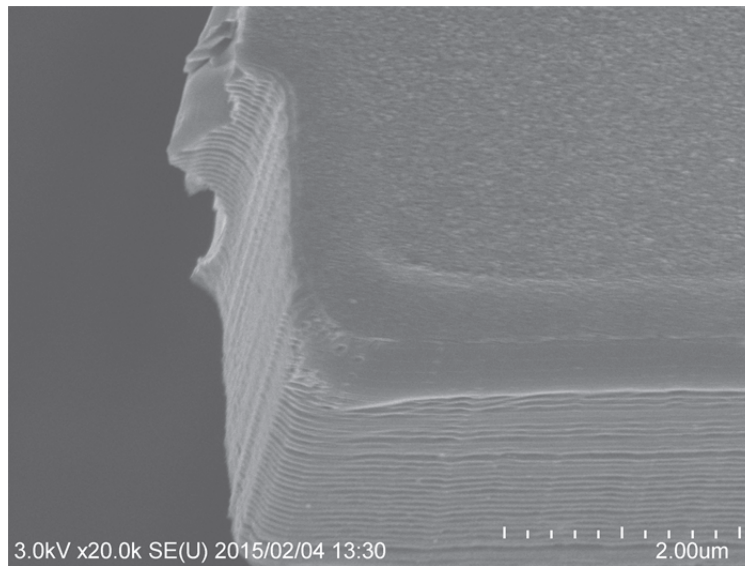


Fig 7.10: Notch area of laser treated sample 3

Samples 4 and 5 exhibited instantaneous fracture. The laser treatment of these samples however was successful in improving roughness at the notch tip as can be seen from figure 7.11. We suspect that the degraded fatigue life can be due to stress concentration features developing at the notch tip. Protrusions were observed at the notch tip of samples irradiated at slightly higher energies and higher angle (65°) such as the sample in figure 7.5 irradiated at 1.4 J/cm^2 , two pulses while tilted at 65° . Looking at figure 7.12 showing the top view of sample 5, a small change (protrusion) in notch profile at the notch center can be observed that is encircled. We suspect that this could be the reason of degraded fatigue life.

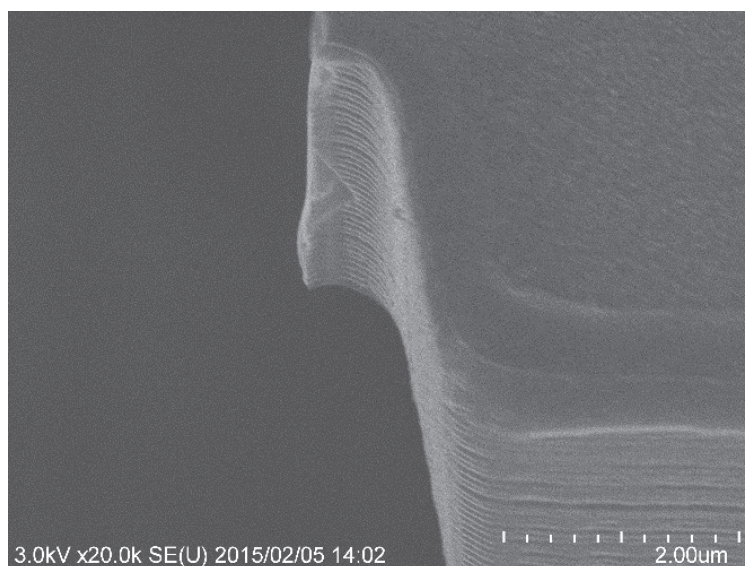


Fig 7.11: Notch area of laser treated sample 5

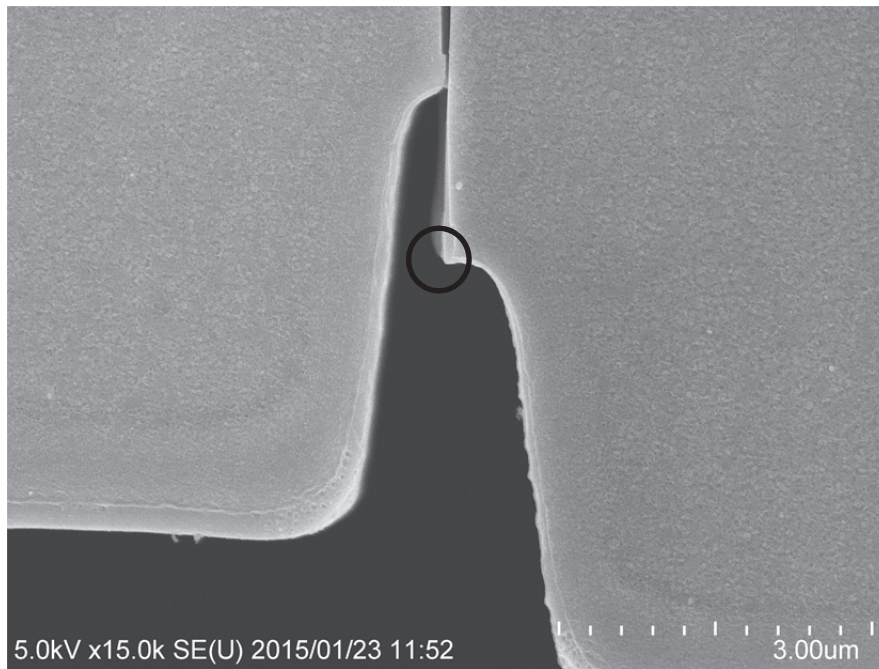


Fig 7.12: Top view at notch area of laser treated sample 5

7.7 Concluding remarks

Fatigue testing of as-fabricated and laser treated fatigue samples having different notch types was conducted. Laser treated samples having a wide notch showed instant fracture before reaching the test deflection amplitude. This is related to the ridges that existed at the notch near the top surface and acted as stress concentration locations. Laser treated narrow notch samples showed an improvement in fatigue life in two tested samples but there was a large variation in fatigue life of the five tested samples. Two laser treated samples fractured instantly which might be due to stress concentration features developing at the notch tip.

8. Conclusions and future work

This study contributes to the field of mechanical properties of SCS microstructures focusing on laser treatment as the means mechanical performance improvement through sidewall roughness modification. This is the first attempt to explore laser treatment of free-standing MEMS structures and demonstrate mechanical performance improvements. Localized irradiation was crucial in improving mechanical performance as it allowed the use of high laser energy on free-standing structures without fracture. Laser treatment parameters such as laser energy, number of pulses and tilt angle were optimized to achieve the roughness reduction without influencing the original shape affecting the performance of micro-mechanical structures.

8.1 Thesis contributions

This study provides insights on the details of laser treatment of SCS microstructures. Several aspects of laser treatment of SCS test structures were explored to get a better understanding on how to achieve the best mechanical performance of structures.

- 1) Localized laser treatment is a key in the success of laser treatment of free-standing structures. Laser treatment with energies up to 4 J/cm^2 was successfully employed without fracture through focusing the laser spot on locations of interest.
- 2) Laser energy among the treatment parameters dominates the resulting surface morphology and roughness. From the conditioning stage, it was found that laser energies between 1.6 J/cm^2 and 2.4 J/cm^2 improved the surface roughness while preserving the notch profile. Higher values of energies between 2.4 J/cm^2 and 4 J/cm^2 led to scallops totally disappearing but caused a significant change in notch radius. The energy value should be optimized for each type of sample according to the function of the sample to be treated for improving mechanical performance.
- 3) Improvement of tensile strength of laser treated SCS structures oriented along both $\langle 110 \rangle$ and $\langle 100 \rangle$ was achieved. The samples showed the improvement of 30% at higher energy irradiation (4 J/cm^2) while the cross section of the samples changed significantly. A low energy condition (1.2 J/cm^2) that

preserved the cross section and focused mainly on sidewalls yielded 6% improvement in strength.

- 4) Laser treatment was successful in improving fatigue life of narrow notch samples. Two samples showed an improvement in fatigue life (1.8×10^9) that was one order of magnitude higher than the average of as-fabricated samples (5.6×10^8). Results showed a variation in fatigue life with another two laser treated samples showing lower fatigue life than as-fabricated samples. This could be attributed to stress concentration features developing at the notch tip.

8.2 Future work

The following aspects could be explored for further optimization of mechanical performance.

- 1) Perpendicular irradiation of top and bottom surfaces of tensile test samples can be considered for further improvement of fracture strength. Perpendicular irradiation of top surfaces would mean that the whole surface would be subjected to high values of energy that could eliminate a region at the middle of the test structure subjected to low energy and acting as a higher roughness location compared to the surrounding regions. Perpendicular irradiation of bottom surfaces would also improve the roughness of lower regions along sidewalls where fracture was noticed to start after laser treatment
- 2) The irradiation environment of laser treatment can be explored. Current experiments on laser treatment took place in air. Irradiation environment might affect the oxygen content of the treated surface as well as surface morphology.

Bibliography

- [1] Hsu, Tai-Ran. *MEMS & microsystems: design, manufacture, and nanoscale engineering*. John Wiley & Sons, 2008.
- [2] David F. Guillou, IC Mechanics, Inc “Packaging MEMS: New Manufacturing Methodology Substantially Reduces Smart MEMS Costs”. *Sensorsmag*, Dec. 2003 web. 2nd March, 2015.
- [3] Alper, Said Emre, and Tayfun Akin. "A single-crystal silicon symmetrical and decoupled MEMS gyroscope on an insulating substrate." *Microelectromechanical Systems, Journal of* 14.4 (2005): 707-717.
- [4] Maillefer, Didier, et al. "A high-performance silicon micropump for disposable drug delivery systems." *Micro Electro Mechanical Systems, 2001. MEMS 2001. The 14th IEEE International Conference on*. IEEE, 2001.
- [5] Vandelli, Nelsimar, et al. "Development of a MEMS microvalve array for fluid flow control." *Microelectromechanical Systems, Journal of* 7.4 (1998): 395-403.
- [6] Gad-el-Hak, Mohamed, ed. *The MEMS handbook*. CRC press, 2010.
- [7] Kang, Wonmo, and M. Taher A. Saif. "In Situ Study of Size and Temperature Dependent Brittle-to-Ductile Transition in Single Crystal Silicon." *Advanced Functional Materials* 23.6 (2013): 713-719.
- [8] Kamiya, S., et al. "Cross comparison of fatigue lifetime testing on silicon thin film specimens." *Micro Electro Mechanical Systems (MEMS), 2011 IEEE 24th International Conference on*. IEEE, 2011.
- [9] Alsem, Daan Hein, et al. "Mechanisms for Fatigue of Micron-Scale Silicon Structural Films." *Advanced Engineering Materials* 9.1-2 (2007): 15-30.
- [10] Ikehara, T., and T. Tsuchiya. "Measurement of anisotropic fatigue life in micrometre-scale single-crystal silicon specimens." *Micro & Nano Letters, IET* 5.1 (2010): 49-52.
- [11] Pierron, Olivier N., and Christopher L. Muhlstein. "The critical role of environment in fatigue damage accumulation in deep-reactive ion-etched single-crystal silicon structural films." *Microelectromechanical Systems, Journal of* 15.1 (2006): 111-119.
- [12] Ikehara, T., and T. Tsuchiya. "Crystal orientation dependence of fatigue characteristics in single crystal silicon measured using a rotating micro resonator." *Micro Electro Mechanical Systems, 2008. MEMS 2008. IEEE 21st International Conference on*. IEEE, 2008.

- [13] Kahn, H., R. Ballarini, and A. H. Heuer. "Dynamic fatigue of silicon." *Current Opinion in Solid State and Materials Science* 8.1 (2004): 71-76.
- [14] Ikehara, Tsuyoshi, and Toshiyuki Tsuchiya. "High-cycle fatigue of micromachined single crystal silicon measured using a parallel fatigue test system." *IEICE Electronics Express* 4.9 (2007): 288-293.
- [16] Ikehara, Tsuyoshi, and Toshiyuki Tsuchiya. "High-cycle fatigue of micromachined single-crystal silicon measured using high-resolution patterned specimens." *Journal of micromechanics and microengineering* 18.7 (2008): 075004.
- [17] Muhlstein, Christopher L., Stuart B. Brown, and Robert O. Ritchie. "High-cycle fatigue of single-crystal silicon thin films." *Microelectromechanical Systems, Journal of* 10.4 (2001): 593-600.
- [18] Ikehara, Tsuyoshi, and Toshiyuki Tsuchiya. "Low-cycle to ultrahigh-cycle fatigue lifetime measurement of single-crystal-silicon specimens using a microresonator test device." *Microelectromechanical Systems, Journal of* 21.4 (2012): 830-839.
- [19] Theillet, P-O., and O. N. Pierron. "Fatigue rates of monocrystalline silicon thin films in harsh environments: Influence of stress amplitude, relative humidity, and temperature." *Applied Physics Letters* 94.18 (2009): 181915.
- [20] Pierron, Olivier N., and Christopher L. Muhlstein. "The critical role of environment in fatigue damage accumulation in deep-reactive ion-etched single-crystal silicon structural films." *Microelectromechanical Systems, Journal of* 15.1 (2006): 111-119.
- [21] Kamiya, S., et al. "Finite fatigue lifetime of silicon under inert environment." *Micro Electro Mechanical Systems (MEMS), 2011 IEEE 24th International Conference on. IEEE, 2011.*
- [22] Ando, Taeko, Mitsuhiro Shikida, and Kazuo Sato. "Tensile-mode fatigue testing of silicon films as structural materials for MEMS." *Sensors and Actuators A: Physical* 93.1 (2001): 70-75.
- [23] Shikida, Mitsuhiro, et al. "Mechanical strengthening of Si cantilevers by chemical wet etching." *Microsystem technologies* 19.4 (2013): 547-553.
- [24] Shikida, Mitsuhiro, et al. "Mechanical strengthening of Si cantilever by chemical KOH etching and its surface analysis by TEM and AFM." *Microsystem Technologies* (2014): 1-8.
- [25] Lee, Kevin K., et al. "Fabrication of ultralow-loss Si/SiO₂ waveguides by roughness reduction." *Optics letters* 26.23 (2001): 1888-1890.

- [26] Sparacin, Daniel K., Kazumi Wada, and Lionel C. Kimerling. "Oxidation kinetics of waveguide roughness minimization in silicon microphotonics." *Integrated Photonics Research*. Optical Society of America, 2003.
- [27] Takahashi, Jun-ichi, et al. "Oxidation-induced improvement in the sidewall morphology and cross-sectional profile of silicon wire waveguides." *Journal of Vacuum Science & Technology B: Microelectronics and Nanometer Structures* 22.5 (2004): 2522-2525.
- [28] Lee, Ming-Chang M., and Ming C. Wu. "Thermal annealing in hydrogen for 3-D profile transformation on silicon-on-insulator and sidewall roughness reduction." *Microelectromechanical Systems, Journal of* 15.2 (2006): 338-343.
- [29] Kim, Sang-Gi, et al. "Behavior of trench surface by H₂ annealing for reliable trench gate oxide." *Journal of crystal growth* 255.1 (2003): 123-129.
- [30] Kuribayashi, Hitoshi, et al. "Investigation of shape transformation of silicon trenches during hydrogen annealing." *Japanese journal of applied physics* 43.4A (2004): L468.
- [31] Hajika, R., et al. "Mechanical strengthening of silicon torsion bar of MEMS scanning mirror by hydrogen anneal." *Micro Electro Mechanical Systems (MEMS), 2013 IEEE 26th International Conference on*. IEEE, 2013.
- [32] Sato, Nobuhiko, and Takao Yonehara. "Hydrogen annealed silicon-on-insulator." *Applied physics letters* 65.15 (1994): 1924-1926.
- [33] Bosseboeuf, A., J. Boulmer, and D. Débarre. "Planarization of rough silicon surfaces by laser annealing." *Applied surface science* 109 (1997): 473-476.
- [34] Sedky, Sherif, Roger T. Howe, and Tsu-Jae King. "Pulsed-laser annealing, a low-thermal-budget technique for eliminating stress gradient in poly-SiGe MEMS structures." *Microelectromechanical Systems, Journal of* 13.4 (2004): 669-675.
- [35] Hung, Shih-Che, Eih-Zhe Liang, and Ching-Fuh Lin. "Silicon waveguide sidewall smoothing by KrF excimer laser reformation." *Journal of Lightwave Technology* 27.7 (2009): 887-892.
- [36] Liang, Eih-Zhe, et al. "Effective energy densities in KrF excimer laser reformation as a sidewall smoothing technique." *Journal of Vacuum Science & Technology B* 26.1 (2008): 110-116.
- [37] Brede, M. "The brittle-to-ductile transition in silicon." *Acta metallurgica et materialia* 41.1 (1993): 211-228.
- [38] Namazu, Takahiro, Yoshitada Isono, and Takeshi Tanaka. "Plastic deformation of nanometric single crystal silicon wire in AFM bending test at intermediate temperatures." *Microelectromechanical Systems, Journal of* 11.2 (2002): 125-135.

- [40] Nakao, Shigeki, et al. "Effect of temperature on fracture toughness in a single-crystal-silicon film and transition in its fracture mode." *Journal of Micromechanics and Microengineering* 18.1 (2008): 015026.
- [41] Nakao, Shigeki, et al. "Mechanical properties of a micron-sized SCS film in a high-temperature environment." *Journal of Micromechanics and Microengineering* 16.4 (2006): 715.
- [42] Namazu, Takahiro, Yoshitada Isono, and Takeshi Tanaka. "Evaluation of size effect on mechanical properties of single crystal silicon by nanoscale bending test using AFM." *Microelectromechanical Systems, Journal of* 9.4 (2000): 450-459.
- [43] Uesugi, Akio., et al. "Effect of crystal orientations on tensile strength of (100) and (110) single crystal silicon" *Mechanical engineering congress, Japan*, 2013.
- [44] Li, Xueping, et al. "Anisotropy in fracture of single crystal silicon film characterized under uniaxial tensile condition." *Sensors and Actuators A: Physical* 117.1 (2005): 143-150.
- [45] Ando, Taeko, et al. "Effect of crystal orientation on fracture strength and fracture toughness of single crystal silicon." *Micro Electro Mechanical Systems, 2004. 17th IEEE International Conference on. (MEMS)*. IEEE, 2004.
- [46] Ando, Taeko, et al. "Orientation-dependent fracture strain in single-crystal silicon beams under uniaxial tensile conditions." *Micromechatronics and Human Science, 1997. Proceedings of the 1997 International Symposium on*. IEEE, 1997.
- [47] Sato, Kazuo, et al. "Tensile testing of silicon film having different crystallographic orientations carried out on a silicon chip." *Sensors and Actuators A: Physical* 70.1 (1998): 148-152.
- [48] Lindroos, Veikko, et al., eds. *Handbook of silicon based MEMS materials and technologies*. Elsevier, 2009.
- [49] Uesugi, A., et al. "Effect of surface morphology and crystal orientations on fracture strength of thin film (110) single crystal silicon." *Solid-State Sensors, Actuators and Microsystems (TRANSDUCERS & EUROSENSORS XXVII), 2013 Transducers & Eurosensors XXVII: The 17th International Conference on*. IEEE, 2013.
- [50] Ikehara, Tsuyoshi, and Toshiyuki Tsuchiya. "Effect of etching surface roughness on the fatigue characteristics of single-crystal silicon" *IEEJ Transaction on sensors and micromachines* 134.2 (2013): 32-37.
- [51] Sparacin, Daniel K., Steven J. Spector, and Lionel C. Kimerling. "Silicon waveguide sidewall smoothing by wet chemical oxidation." *Journal of lightwave technology* 23.8 (2005): 2455.

- [52] Shikida, Mitsuhiro, et al. "Differences in anisotropic etching properties of KOH and TMAH solutions." *Sensors and Actuators A: Physical* 80.2 (2000): 179-188.
- [53] Rogers, James W., and Leslie M. Phinney. "Temperature response of silicon MEMS cantilevers during and after Nd: YAG laser irradiation." *Numerical Heat Transfer, Part A: Applications* 45.8 (2004): 737-750.
- [54] Rogers, James W., and Leslie M. Phinney. "Process yields for laser repair of aged, stiction-failed, MEMS devices." *Microelectromechanical Systems, Journal of* 10.2 (2001): 280-285.
- [55] Zhang, X. Richard, and Xianfan Xu. "Laser bending for high-precision curvature adjustment of microcantilevers." *Applied Physics Letters* 86.2 (2005): 021114.
- [56] Dirscherl, Manfred, Gerd Esser, and Michael Schmidt. "Ultrashort pulse laser bending." *Journal of Laser Micro/Nanoengineering* 1.1 (2006): 54-60.
- [57] Darif, Mohamed, Nadjib Semmar, and France Orléans Cedex. "Numerical Simulation of Si Nanosecond Laser Annealing by COMSOL Multiphysics." *Proceedings of the COMSOL Conference 2008 Hannover*. 2008.
- [58] Kudryashov, Sergey I., and Susan D. Allen. "Photoacoustic study of KrF laser heating of Si: Implications for laser particle removal." *Journal of applied physics* 92.10 (2002): 5627-5631.
- [59] Tam, Andrew C., et al. "Laser-cleaning techniques for removal of surface particulates." *Journal of Applied Physics* 71.7 (1992): 3515-3523.
- [60] Park, Hee K., et al. "A practical excimer laser-based cleaning tool for removal of surface contaminants." *Components, Packaging, and Manufacturing Technology, Part A, IEEE Transactions on* 17.4 (1994): 631-643.
- [61] Pedraza, A. J., J. D. Fowlkes, and D. H. Lowndes. "Silicon microcolumn arrays grown by nanosecond pulsed-excimer laser irradiation." *Applied Physics Letters* 74.16 (1999): 2322-2324.
- [62] Sanchez, F., et al. "Whiskerlike structure growth on silicon exposed to ArF excimer laser irradiation." *Applied physics letters* 69.5 (1996): 620-622.
- [63] Anthony, T. R., and H. E. Cline. "Surface rippling induced by surface-tension gradients during laser surface melting and alloying." *Journal of Applied Physics* 48.9 (1977): 3888-3894.
- [64] Amutha, Gomathinayagam, et al. "Investigations on Nano-and Pico-Second Laser Based Annealing Combined Texturing of Amorphous Silicon Thin Films for Photovoltaic Applications." *Journal of Solid Mechanics and Materials Engineering* 7.2 (2013): 206-216.

- [65] Palani, I. A., et al. "Investigation on laser-annealing and subsequent laser-nanotexturing of amorphous silicon (a-Si) films for photovoltaic application." *JLMN-Journal of Laser Micro/Nanoengineering* 5.2 (2010): 150-155.
- [66] Nayak, Barada K., et al. "Self-organized 2D periodic arrays of nanostructures in silicon by nanosecond laser irradiation." *Applied optics* 50.16 (2011): 2349-2355.
- [67] Yan, Ji Wang, Tooru Asami, and Tsunemoto Kuriyagawa. "Complete Recovery of Subsurface Structures of Machining-Damaged Single Crystalline Silicon by Nd: YAG Laser Irradiation." *Key Engineering Materials* 389 (2009): 469-474.
- [68] De Wolf, Ingrid. "Micro-Raman spectroscopy to study local mechanical stress in silicon integrated circuits." *Semiconductor Science and Technology* 11.2 (1996): 139.
- [69] Steen, William, Kenneth G. Watkins, and Jyotirmoy Mazumder. *Laser material processing*. Springer Science & Business Media, 2010.
- [70] Lee, C. H., K. Jiang, and G. J. Davies. "Sidewall roughness characterization and comparison between silicon and SU-8 microcomponents." *Materials characterization* 58.7 (2007): 603-609.
- [71] Lawn, Brian R. *Fracture of brittle solids*. Cambridge university press, 1993.

Appendix A

The code for FEA simulation to determine temperature distribution due to a single pulse laser irradiation at 1.6 J/cm^2 for fatigue test samples while tilted by 65°

/title,3d Laser problem

/PREP7

ANTYPE,TRANS

!Type of analysis

ET,1,SOLID70

!Type of element

MPTEMP,1,298,400,600,900,1200,1689

!Material properties

MPTEMP,7,1709,2000,2500,3000,10000,15000

MPDATA,KXX,1,1,148,148,148,148,148,148

MPDATA,KXX,1,7,200,200,200,200,200,200

MPDATA,DENS,1,1,2320,2320,2320,2320,2320,2320

MPDATA,DENS,1,7,2500,2500,2500,2500,2500,2500

MPDATA,C,1,1,710,710,710,710,710,710

MPDATA,C,1,7,680,680,680,680,680,680

CLOCAL,11,0,0,0,-4E-6,-25,0,0,,

w=10e-6

!Solid model construction

ww=-w/0.906307787

K,3,0,0,-9E-6

!Defining keypoints

K,4,0,-5e-6,-9E-6

K,1,-W,-5e-6,-9E-6

K,2,-W,0,-9E-6

K,5,0,0,0

K,6,0,-5E-6,0

K,11,-W,0,0

K,50,-W,-5E-6,0

k,8,-0.021445069e-6,-5e-6,-9E-6

k,16,-0.021445069e-6,-5e-6,0

K,22,-W,-0.01E-6,0

K,24,-W,-0.01E-6,-9E-6

K,25,-W,0,4E-6

K,26,-4E-6,0,4E-6

K,27,-4E-6,-5E-6,4E-6

K,28,-W,-5E-6,4E-6
K,29,-W,-0.01E-6,4E-6
K,30,-4.021445069E-6,-5E-6,4E-6
K,31,-4.021445069E-6,-0.01E-6,4E-6
k,9,-0.021445069e-6,-0.01E-6,-9E-6
k,15,-0.021445069e-6,-0.01E-6,0
K,17,-W,-0.4663076582*w,-9E-6
K,18,-W,-0.4663076582*w,0
K,19,-W,-0.4663076582*(w-4e-6),4E-6

CSYS,0

A,2,24,22,11

! Defining areas and volumes

A,3,5,15,9

A,2,11,5,3

A,24,22,15,9

A,2,24,9,3

A,11,22,15,5

VA,1,2,3,4,5,6

A,4,6,16,8

A,3,9,8,4

A,5,15,16,6

A,3,5,6,4

A,9,15,16,8

VA,2,7,8,9,10,11

A,24,22,18,17

A,9,15,18,17

A,24,17,9

A,22,18,15

VA,4,12,13,14,15

A,17,1,8,9

A,18,50,16,15

A,1,50,16,8

A,17,18,50,1

VA,13,11,16,17,18,19

A,25,29,31,26

A,11,25,26,5
A,22,29,31,15
A,11,25,29,22
A,5,26,31,15
VA,6,20,21,22,23,24
A,6,27,30,16
A,26,31,30,27
A,5,26,27,6
A,15,31,30,16
VA,24,9,25,26,27,28
A,29,19,31
A,22,29,19,18
A,15,31,19,18
VA,15,22,29,30,31
A,19,28,30,31
A,50,28,30,16
A,18,19,28,50
VA,17,31,28,32,33,34
MSHAPE,3D
LESIZE,8,,4
LESIZE,5,50E-9
LESIZE,19,,50
LESIZE,11,,200
LESIZE,36,,114
LESIZE,25,,50,0.1
LESIZE,23,,25
lesize,28,,5
LESIZE,27,,25,0.25
VMESH,1
VMESH,2
VSWEEP,3
vsweep,4
Vmesh,5
VMESH,6

!Mesh attributes

!Defining element sizes on lines

!Volume meshing

```

V sweep,7
v sweep,8
/ solu
NSEL,S,LOC,Y,0,10E-6          ! Applying loads on selected
nodes
NSEL,R,LOC,Z,-4E-6,-13E-6
BF,ALL,HGEN,%LASERUP%      !Applying volume heat generated load due to laser
ALLSEL,ALL
VSEL,S,,,5,7,2
ESLV,S,ALL
NSLE,S,ALL
BF,ALL,HGEN,%LASERUP%      !Applying volume heat generated load due to laser
ALLSEL,ALL
VSEL,S,,,6,8,2
ESLV,S,ALL
NSLE,S,ALL
BF,ALL,HGEN,%LASERZ%      !Applying volume heat generated load due to laser
ALLSEL,ALL
NSEL,S,LOC,Y,-10E-6,0
NSEL,R,LOC,Z,-4E-6,-13E-6
BF,ALL,HGEN,%LASERDO%      !Applying volume heat generated load due to laser
ALLSEL,ALL
SFA,12,,CONV,10,298          !Applying surface convection boundary conditions
SFA,12,,RAD,0.37,298        !Applying surface radiation boundary conditions
SFA,30,,CONV,10,298          !Applying surface convection boundary conditions
SFA,30,,RAD,0.37,298        !Applying surface radiation boundary conditions
SFA,19,,CONV,10,298          !Applying surface convection boundary conditions
SFA,19,,RAD,0.37,298        !Applying surface radiation boundary conditions
SFA,34,,CONV,10,298          !Applying surface convection boundary conditions
SFA,34,,RAD,0.37,298        !Applying surface radiation boundary conditions
SFA,1,,CONV,10,298          !Applying surface convection boundary conditions
SFA,1,,RAD,0.37,298        !Applying surface radiation boundary conditions
SFA,23,,CONV,10,298          !Applying surface convection boundary conditions
SFA,23,,RAD,0.37,298        !Applying surface radiation boundary conditions

```

SFA,18,,CONV,10,298	!Applying surface convection boundary conditions
SFA,18,,RAD,0.37,298	!Applying surface radiation boundary conditions
SFA,33,,CONV,10,298	!Applying surface convection boundary conditions
SFA,33,,RAD,0.37,298	!Applying surface radiation boundary conditions
SFA,7,,CONV,10,298	!Applying surface convection boundary conditions
SFA,7,,RAD,0.37,298	!Applying surface radiation boundary conditions
SFA,25,,CONV,10,298	!Applying surface convection boundary conditions
SFA,25,,RAD,0.37,298	!Applying surface radiation boundary conditions
SFA,10,,CONV,10,298	!Applying surface convection boundary conditions
SFA,10,,RAD,0.37,298	!Applying surface radiation boundary conditions
SFA,27,,CONV,10,298	!Applying surface convection boundary conditions
SFA,27,,RAD,0.37,298	!Applying surface radiation boundary conditions
SFA,3,,CONV,10,298	!Applying surface convection boundary conditions
SFA,3,,RAD,0.37,298	!Applying surface radiation boundary conditions
SFA,21,,CONV,10,298	!Applying surface convection boundary conditions
SFA,21,,RAD,0.37,298	!Applying surface radiation boundary conditions
Allsel,all	
TRNOPT,FULL	
OUTRES,ALL,ALL	
TUNIF,298	! Initial temperature
AUTOTS,ON	
DELTIM,1E-9,0.1e-10,2e-9	
TIME,60e-9	! Final time
SOLVE	! Solving the model

List of publications

Journal papers

- 1) Mitwally, Mohamed E., et al. "Improvement of tensile strength of freestanding single crystal silicon microstructures using localized harsh laser treatment." *Japanese Journal of Applied Physics* 53.6S (2014): 06JM03.
- 2) Mitwally, Mohamed Elwi, et al. "Surface Roughness Modification of Free Standing Single Crystal Silicon Microstructures Using KrF Excimer Laser Treatment for Mechanical Performance Improvement." *Journal of Surface Engineered Materials and Advanced Technology* 5.01 (2015): 28.
- 3) Mitwally, M. Elwi, et al. "Effect of localized KrF excimer laser treatment on fracture behaviors of freestanding <110> and <100> single crystal silicon beams." *Microsystem Technologies* (2015): 1-8.

International conferences

- 1) Mitwally, Mohamed E., et al. "KrF excimer laser reformation for sidewall smoothing of free-standing single crystal silicon beams". *Proceedings of the international workshop on Micro-/Nano engineering, Kyoto, Japan.* (2011)
- 2) Mitwally, Mohamed E., et al. "Improvement of tensile strength of freestanding single crystal silicon microstructures using localized harsh laser treatment." *Proceedings of the 26th International Microprocesses and Nanotechnology Conference (MNC 2013), Sapporo, Japan.* (2013)